Volume 42
DOE/DP40200-124

LLE Review

Quarterly Report

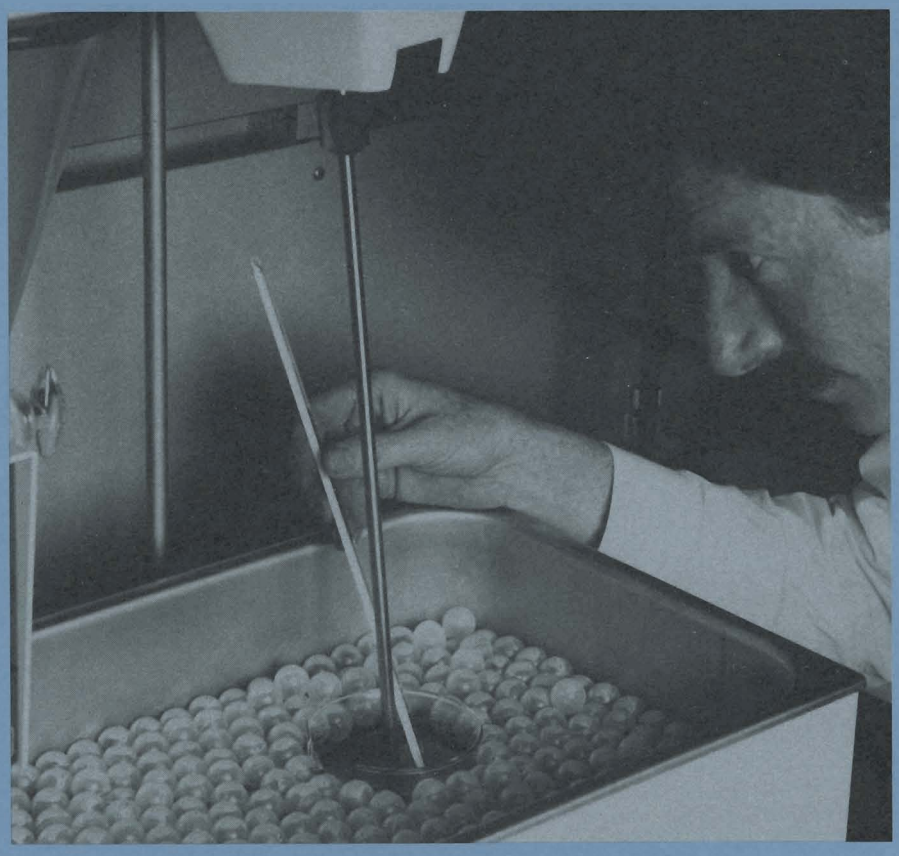

January–March 1990

Laboratory for Laser Energetics
College of Engineering and Applied Science
University of Rochester
250 East River Road
Rochester, New York 14623-1299

Volume 42
DOE/DP40200-124

LLE Review

Quarterly Report

Editor: D. K. Bradley
(716) 275-5769

January–March 1990

Laboratory for Laser Energetics
College of Engineering and Applied Science
University of Rochester
250 East River Road
Rochester, New York 14623-1299

IN BRIEF

This volume of the LLE Review, covering the period January–March 1990, contains a study of electron heat transport using two-dimensional Fokker-Planck simulations and an article describing how plastic microshells are being manufactured at LLE for future implosion studies. The advanced technology section reports on an experiment that has measured exponential gain in a number of x-ray lasing transitions and discusses the continuing development of a two-dimensional high-speed electro-optic probing system. Finally, the activities of the National Laser Users Facility and the GDL and OMEGA laser facilities are summarized.

The highlights of this issue are

- The validity of fluid models of electron transport has been investigated in the context of laser fusion. Comparisons with numerical solutions of the electron Fokker-Planck equation confirm the existence of flux inhibition for $(Z + 1)^{1/2} \lambda_t > 0.005\ l$, where λ_t is the scattering mean free path of a thermal electron and l is the appropriate temperature scale length. When compared with fluid predictions, two-dimensional Fokker-Planck simulations of heat transport under nonuniform laser illumination show reduced smoothing in the corona and enhanced smoothing at the ablation surface.

- Large numbers of polystyrene microshells have been produced using the microencapsulation technique. The resultant shells have very uniform wall thickness, a smooth surface finish, and few, if any, vacuoles embedded in the wall. In an adaptation of the process, the number of shells lost due to cracking has been significantly reduced by using osmotic action to remove water from the interior of the shells.

- X-ray laser experiments on the single-beam GDL laser have demonstrated gain in several elements using slab targets. Collisionally pumped Ne-like Ge was observed to lase on five $3s$–$3p$ transitions in the range 196 Å–287 Å. Other experiments showed lasing on the $3d$–$5f$ and $3d$–$4f$ transitions in Li-like Al (105 Å and 154 Å). This scheme was extended to produce gain in Ti at 47 Å. Additionally, a new lasing transition has been demonstrated in the Ti targets at a wavelength of 326.5 Å. It is speculated that this is a $3s$–$3p$ transition in Ne-like Ti and may be pumped by mechanisms other than collisions.

- A two-dimensional time-resolved electro-optic probe has been developed and used to measure surface-field collapse in a number of photoconductive switches with 200-ps time resolution and 3-μm spatial resolution. The switching speed and generation of field enhancements in a GaAs bulk switch were found to be dependent on the illumination configuration and the applied field. Switching efficiency was found to decrease with increasing field.

CONTENTS

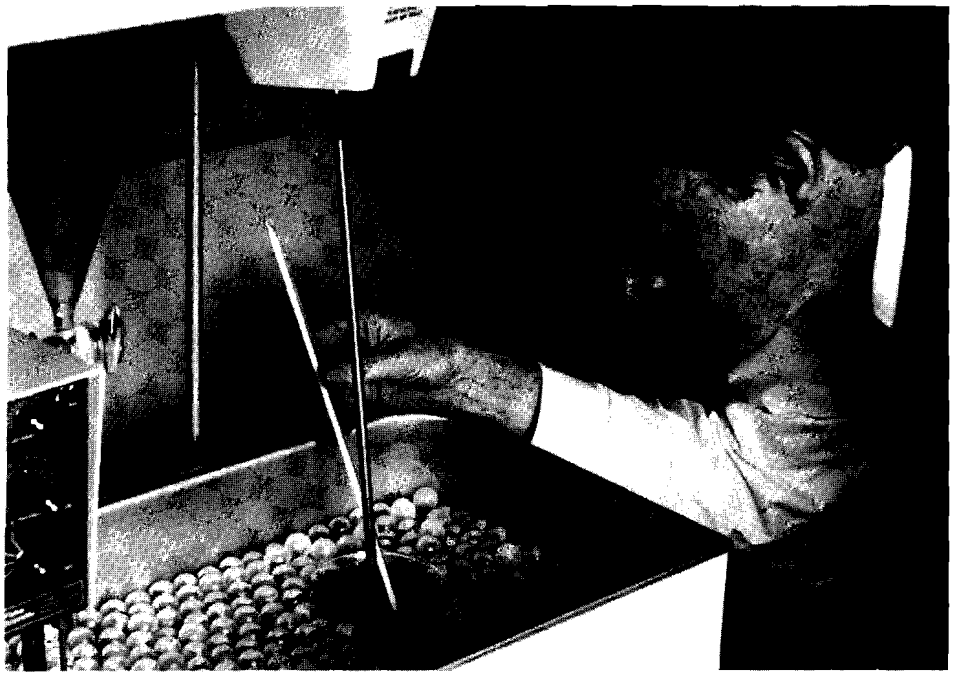

Stephen Noyes, Senior Technical Associate, is shown monitoring solution temperature during production of polystyrene shells made by the microencapsulation process. Highly uniform polymer shells necessary for high-density implosions are produced by this method.

Section 1
PROGRESS IN LASER FUSION

1.A Electron Kinetics in Laser-Driven Inertial Confinement Fusion

One important requirement for the modeling of the dynamics of laser-driven inertial confinement fusion (ICF) is a proper understanding of electron transport.[1] Electron transport from the critical surface, where most of the laser energy is absorbed, to the cold overdense plasma gives rise to the ablatively driven implosion necessary for fusion. The presence of lateral transport is responsible for smoothing out short-scale thermal modulations that may arise as a result of nonuniform laser illumination, thereby reducing the "seed" for instabilities that are detrimental to efficient target compression.

All processes associated with thermal electron transport are normally studied by solving the fluid equations using classical heat conduction $q_c = -\kappa_c \nabla T$, where κ_c is the thermal conductivity (also known as the Spitzer-Härm conductivity),[2] and T is the temperature in energy units. However, typical laser plasmas involve high temperatures and short scale lengths, where the mean free path of a heat-carrying electron (which has an energy of about $7T$) may be comparable to $l = T/|\nabla T|$.[3] Under such conditions the electron transport becomes nonlocal, i.e., cannot be adequately described in terms of a local ∇T, and fluid theory breaks down. The need for a kinetic treatment of the electrons has thus resulted in many transport studies based on numerical solutions of the Fokker-Planck (FP) equation.[4–6] Figure 42.1 schematically shows the consequences of highly nonlocal transport in a laser-produced plasma.

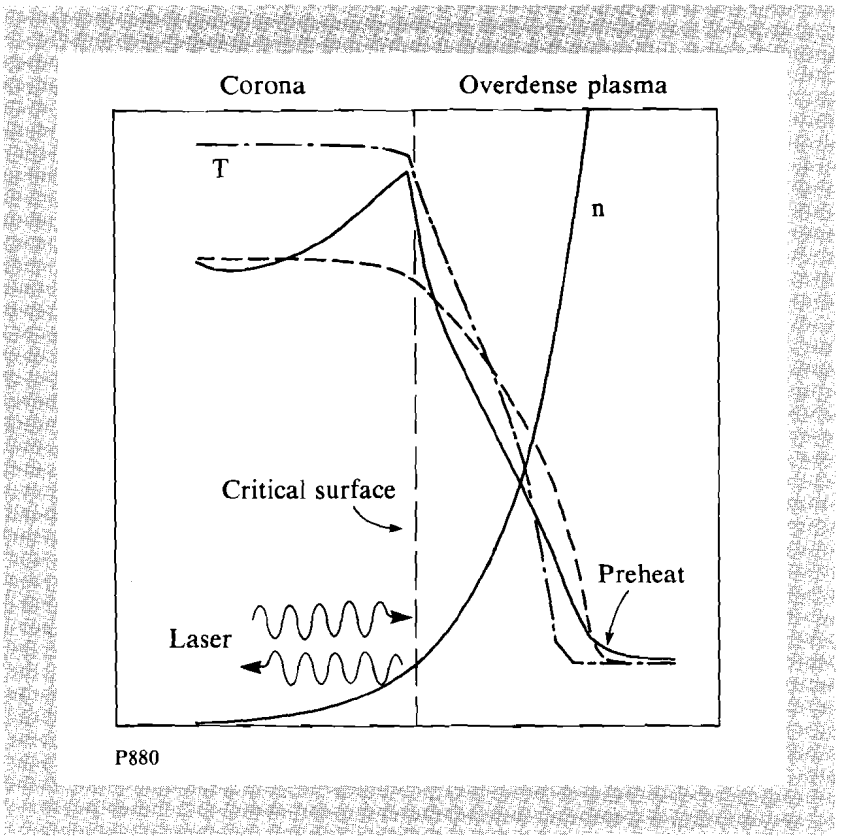

Fig. 42.1
Schematic of density (n) and temperature (T) profiles in a laser-produced plasma where kinetic effects are assumed dominant. Solid curves refer to FP heat flow, dashed curves to classical heat flow, and dash-dotted curves to flux-limited heat flow. For simplicity, n is assumed invariant.

A characteristic feature of nonlocal transport is the ability of coronal electrons to deposit their energy ahead of the main heat front, thereby causing undesirable preheating of the fuel. Also, if electron thermalization is not sufficiently strong to maintain a Maxwellian distribution, the hot corona becomes partially depleted of heat-carrying electrons. This has the effect of reducing their phase-space density gradient, which in turn reduces their diffusive flow, thereby lowering the effective heat flow. This phenomenon, known as flux inhibition, is commonly identified with a flux-limiting parameter f, which when multiplied by the "free-streaming" heat flux

$$q_f = nmv_t^3 (\text{where } v_t = \sqrt{T/m})$$

provides an upper bound to q_c.[7] The resultant heat front is correspondingly modified as shown qualitatively in Fig. 42.1. Another manifestation of the departure from classical heat flow arises in multidimensional transport where $\boldsymbol{q}$ is not necessarily parallel to $-\nabla T$.[5,6]

These issues and others associated with nonlocal transport in ICF are addressed in this article. Our main approach is based on comparisons between fluid and FP results. For a review of experimental investigations of heat transport we refer to an article by Delettrez (1986).[8] Other physical processes that may also affect the heat flow, such as magnetic field generation, ion-acoustic instability, and strong inverse-bremsstrahlung heating, are

reviewed by Kruer (1988).[9] In the following sections we first present a brief derivation of the classical heat-flow formula, identify several reasons for its breakdown, and discuss the physical motivation behind the flux limiter. We then provide a more detailed analysis of nonlocal transport by solving the FP equation. In particular we demonstrate a case where the simple flux limiter fails. This is followed by a section devoted to simulations more closely applicable to ICF conditions. We close by discussing the results and what further investigations are needed on the subject of nonlocal transport.

All of the transport simulations presented in this article are obtained using the 2-D FP code SPARK.[5,6] The code is Eulerian (in Cartesian or cylindrical geometries) and is coupled to a fluid-ion package. Magnetic field effects are not presently included.

Classical Heat Flow and the Flux Limiter

We start with the electron FP equation for a fully ionized plasma, where ions are assumed to be cold and at rest and magnetic-field effects are neglected:

$$\frac{\partial}{\partial t} f + \boldsymbol{v} \cdot \nabla f - \frac{e}{m} \boldsymbol{E} \cdot \nabla_v f = C. \tag{1}$$

The electron distribution function at a spatial point $\boldsymbol{r}$, velocity $\boldsymbol{v}$, and time t is given by $f(\boldsymbol{r},\boldsymbol{v},t)$, e is the electron charge, m is the electron mass, $\boldsymbol{E}$ is the electric field, and C is the FP collision operator. The properties and form of the latter are described in detail elsewhere.[10]

The basis for calculating the heat flow from Eq. (1) assumes that the plasma is close to thermodynamic equilibrium, so that we may expand f as[10]

$$f = f_0 + \boldsymbol{v} \cdot \boldsymbol{f}_1 / v, \tag{2}$$

where $f_0(\boldsymbol{r},v,t)$ is the isotropic part, taken to be a Maxwellian, and $\boldsymbol{f}_1$ is the anisotropic part describing the transport. Substituting Eq. (2) into Eq. (1) and dropping the time derivative we obtain

$$\boldsymbol{f}_1 = -\lambda(v)\left(\nabla f_0 - \frac{e\boldsymbol{E}}{mv}\frac{\partial}{\partial v} f_0\right), \tag{3}$$

where $\lambda(v) = v^4/[n(Z+1)\,4\pi(e^2/m)^2 \ln\Lambda]$ is the velocity-dependent scattering mean free path. In deriving Eq. (3) we have neglected electron-electron momentum exchange, an assumption that is strictly valid only for high-Z plasmas. However, for the purpose of comparing classical with nonlocal transport, this assumption is relatively unimportant.[4]

By invoking quasi-neutrality and therefore zero current [i.e., $j = -(4\pi/3)\int dv v^3 f_1 = 0$] we obtain

$$eE/m = -v_t^2(5\nabla T/2T + \nabla n/n)$$

and

$$f_1 = \lambda_t\left(\frac{v}{v_t}\right)^4\left[\frac{1}{2}\left(\frac{v}{v_t}\right)^2 - 4\right]\frac{\nabla T}{T}f_0, \tag{4}$$

where $\lambda_t = \lambda(v_t)$. We now calculate the heat flow using the definition

$$q = (2\pi/3)\int dv v^4 f_1$$

and obtain $q_c = -\kappa_c \nabla T$, where $\kappa_c = \gamma n v_t \lambda_t$, and $\gamma = 64(2/\pi)^{1/2}$. A more detailed calculation of transport coefficients for arbitrary Z and magnetic fields is given by Epperlein and Haines (1986).[11]

The first problem with the present calculation for q is the fact that the perturbation analysis breaks down, i.e., $|f_1/f_0| \gg 1$, for large v, thus giving rise to a negative distribution function. This unphysical behavior is most likely to occur for small values of $l\,(=T/|\nabla T|)$, as seen from Eq. (4). More precisely, since the main contribution to the heat-flow integral comes from $v \sim v^* = 3.7\,v_t$, the validity criterion becomes $\lambda_t < 0.002\,l$, by requiring that $|f_1/f_0| < 1$ at v^*.[3,4,12] However, as will be demonstrated in the next section, a more accurate criterion should also involve the electron-electron energy-loss mean free path.

Another limitation of the classical heat-flow formulation comes from the prediction of infinite energy flux as $l \to 0$. On physical grounds we might expect the energy flow to be limited to some fraction f of $q_f = nmv_t^3$, the "free-streaming limit." We may, therefore, arbitrarily define an effective heat flow as either $q = \min(q_c, fq_f)$, or $q = q_c/(1 + q_c/fq_f)$,[7] based on the "sharp cutoff" or "harmonic mean" method, respectively. Both methods yield similar results, though the harmonic mean, adopted in this study, gives a stronger reduction for a given value of f. Currently acceptable values for f range from about 0.03 to 0.2 (larger values essentially give $q = q_c$).[8] *A priori*, based on the simple arguments presented above, there is no simple way to predict a unique value of f. Also, because of its local character, one cannot expect the flux limiter to be applicable in situations where nonlocal transport effects are dominant. In particular, it fails to account for the possibility of preheat.

Although the flux limiter is a very useful tool in many situations, one must exercise caution when using it. As will be demonstrated in the following sections there are certain cases for which it is totally inadequate.

Heat Flow in a Homogeneous Plasma

To more accurately investigate nonlocal transport the FP equation must be solved numerically. Our starting assumption is once again the expansion defined by Eq. (2), which is sufficient for demonstrating the major features of nonlocal transport and is probably adequate for most transport problems relevant to ICF.[4] The contributions from other terms in the expansion become necessary when one is interested in nearly collisionless phenomena and electromagnetic instabilities.[13]

We do not assume a Maxwellian form for f_o, unlike in the previous section, but rather solve for it using the equation

$$\frac{\partial f_o}{\partial t} + \frac{v}{3}\nabla \cdot \boldsymbol{f}_1 = \frac{1}{v^2}\frac{\partial}{\partial v}\left[\frac{v^2}{3}\boldsymbol{a}\cdot\boldsymbol{f}_1 + Y\left(C_o f_o + D_o \frac{\partial}{\partial v} f_o\right) + \frac{YnZ}{6v} v_o^2 \frac{\partial}{\partial v} f_o\right], \tag{5}$$

where $\boldsymbol{a} = |e|\boldsymbol{E}/m$, $Y = 4\pi(e^2/m)^2 \ln\Lambda$, and $C_o(f_o)$ and $D_o(f_o)$ are integral operators, as defined by Shkarofsky *et al.*[10] The last term in the equation is the inverse-bremsstrahlung operator, with v_o being the electron quiver velocity in the laser field.[14] Equations (3) and (5), coupled with the quasi-neutrality condition and a few modifications to account for ion motion, are solved in the 2-D code SPARK, the details of which are described in Refs. 5 and 6.

As a first illustration of kinetic transport consider a homogeneous plasma of temperature T_o, where we apply a perturbation of the form $\delta T(t)e^{ikx}$, such that $\delta T \ll T_o$. Using the energy-conservation equation $(3/2)n\partial_t T + \nabla \cdot \boldsymbol{q} = 0$, it is easily shown that $\delta T_c(t) = \delta T_c(t=0)e^{-t\alpha}$, where $\alpha = 2k^2\kappa_c/3n$ is the classical decay rate. By numerically calculating the temperature decay using SPARK, and defining $\alpha_{FP} = 2k^2\kappa_{FP}/3n$, it is then possible to obtain κ_{FP}/κ_c. This gives us a measure of departure from classical transport. By varying k we obtain different values of κ_{FP}/κ_c, which are then plotted in Fig. 42.2 as a function of $(k\lambda_d)^{-1}$, where $\lambda_d = (\lambda_e\lambda_t)^{1/2} = (Z+1)^{1/2}\lambda_t$ is an effective delocalization length (or stopping length), and $\lambda_e = T^2/4\pi ne^4 \ln\Lambda$ is the energy-loss mean free path.[15] The origin of λ_d may be traced back to Eqs. (3) and (5) by estimating

$$v^{-2}\partial(YC_o f_o)/\partial v \sim (v_t/\lambda_e) f_o$$

as the electron-electron energy-loss term, and comparing it to the spatial diffusion term $v\nabla \cdot \boldsymbol{f}_1 \sim v_t\lambda_t\nabla^2 f_o \sim v_t\lambda_t f_o/\lambda_d^2$, assuming $v = v_t$. In effect, λ_d provides a better measure of delocalization than λ_t alone (with some appropriate weighting to account for the higher-velocity heat-carrying electrons), since it also depends on the strength of the electron-electron energy loss.

In Fig. 42.2 we observe a departure from classical heat flow, in the form of flux inhibition, for scale lengths $k^{-1} < 200\,\lambda_d$. Such an effect, which has been predicted by Bell in the context of ion waves,[16] clearly demonstrates a situation where nonlocal electron transport is present and yet $q_c \ll fq_f$, i.e., the heat flow is unsaturated. In fact, since the heat flow is arbitrarily small, there is no unique value of f that will give $q_{FP} = q_c$. The explanation for the flux inhibition comes from the fact that, for $l \ll 200\,\lambda_d$, the heat-carrying electrons are able to diffuse across many wavelengths, thereby reducing their density gradient in phase space. Since the modulation e^{ikx} refers to the thermal electrons (with energies ~ T), and the electron thermalization to higher energies ($E^* \sim 7T$) is not instantaneous, the effective heat flux is reduced, as shown schematically in Fig. 42.3.

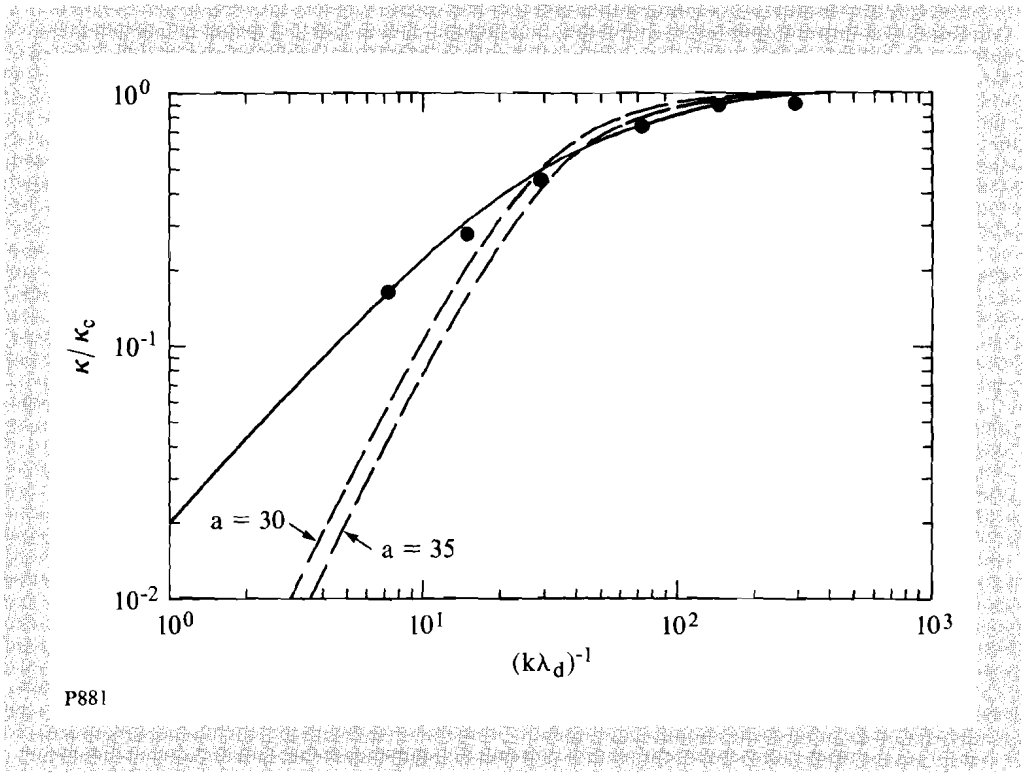

Fig. 42.2
Plot of κ_{FP}/κ_c (solid curve) and κ_d/κ_c (dashed curves) as functions of $(k\lambda_d)^{-1}$. Data points are obtained from a 2-D FP simulation.

At this point it is interesting to investigate the properties of so-called delocalization models of heat flux, designed to bridge the gap between fluid and kinetic theories. The simplest one, first proposed by Luciani *et al.*,[15] is given by

$$q_d(x) = \int_{-\infty}^{\infty} dx' \frac{q_c(x')}{2\lambda_0(x')} \exp\left[-|x - x'|/\lambda_0(x')\right]$$

for a homogeneous plasma. Here, $\lambda_0 = a\lambda_d$ and a is a free parameter. By Fourier analyzing the above equation it is straightforward to show that

$$q_d / q_c = \kappa_d / \kappa_c = (1 + a^2 k^2 \lambda_d^2)^{-1}$$

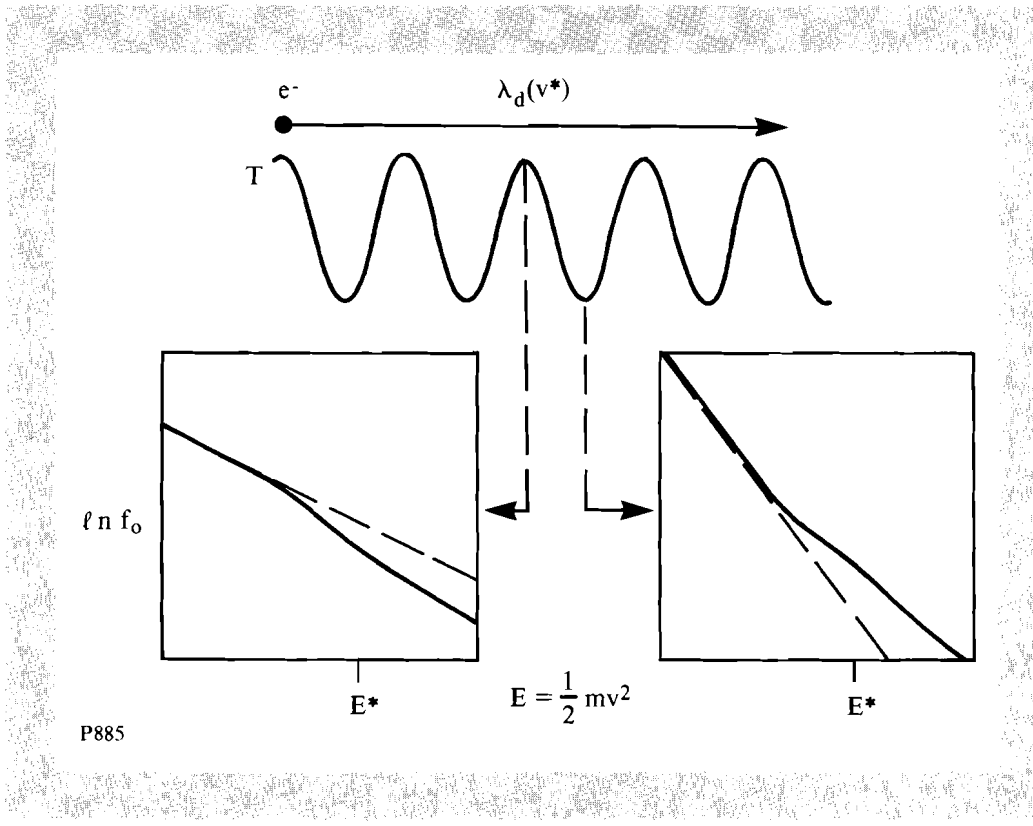

Fig. 42.3
Qualitative description of nonlocal transport. In the distribution plots, solid curves are based on a kinetic calculation, whereas dashed curves are obtained assuming a Maxwellian distribution at the local temperature.

so that at first sight it appears to have the desired property that κ_d/κ_c decreases for large $k\lambda_d$. However, plotting this function in Fig. 42.2 using $a = 30$–35 (which covers the range of values quoted in the literature)[15] gives poor agreement with the FP data. The main reason is that for large $k\lambda_d$, $\kappa_{FP}/\kappa_c \sim (k\lambda_d)^{-1}$, whereas $\kappa_d/\kappa_c \sim (k\lambda_d)^{-2}$. Such a discrepancy may explain the somewhat limited success enjoyed by delocalization models in ICF-related transport simulations.[8,17]

Heat Flow in a Laser-Heated Plasma

Here we review the results of 2-D transport simulations that illustrate some of the subtleties associated with nonlocal transport. We investigate the thermal response of a CH target that has been subjected to nonuniform laser irradiation. It is particularly important to predict the level of thermal smoothing at the beginning of the laser pulse since the effectiveness of the implosion may depend on it.

As it is not yet feasible to run a full 2-D laser-ablative implosion using SPARK we restrict ourselves to the early-time response by keeping the ions stationary. The background density profile, shown in Fig. 42.4, is obtained using the 1-D fluid code *LILAC*.[18] The conditions correspond to that of a

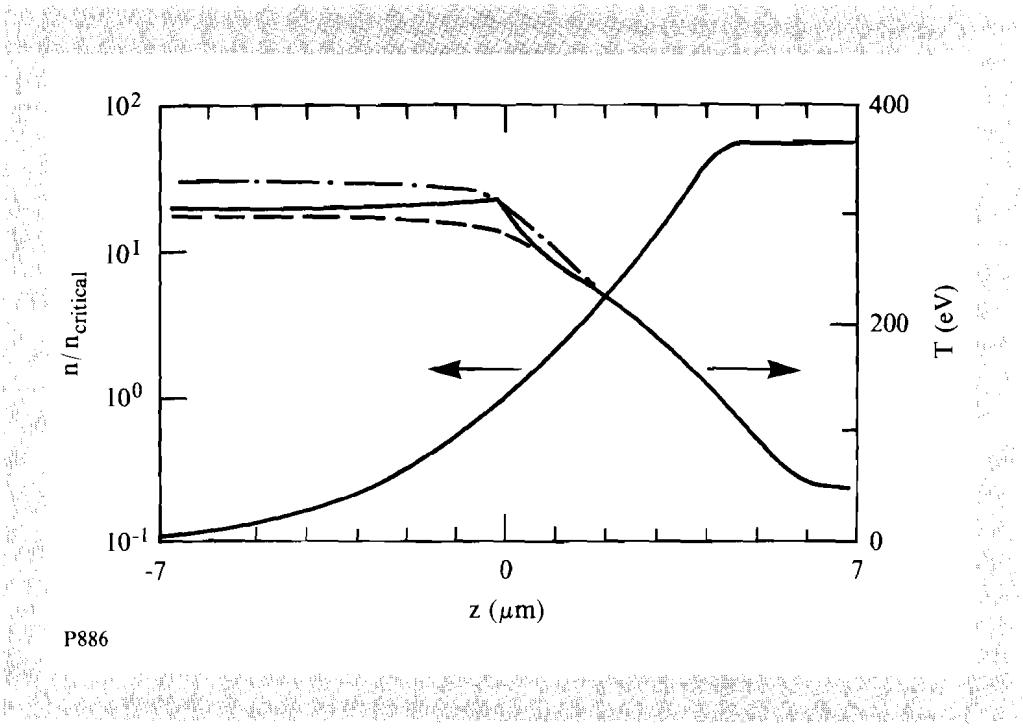

Fig. 42.4
Density n (normalized to the critical density value) and temperature T (in eV) profiles after a 100-ps laser pulse. Curves are identified as in Fig. 42.1.

300-μm-diameter, 10-μm-thick CH target irradiated by a 0.35-μm laser of peak intensity 5×10^{14} W/cm^2 and a Gaussian temporal pulse of 600-ps FWHM. The plot is taken at 600 ps before the peak, when the intensity is $\sim 3 \times 10^{13}$ W/cm^2. SPARK is initialized at this intensity (which is maintained constant in time) and at a temperature of 50 eV. After a few tens of picoseconds the coronal temperature reaches approximately 300 eV and the thermal front evolves in a quasi-steady fashion. Figure 42.4 shows the FP and fluid results at 100 ps. The very slight flux inhibition (not noticeable in the figure) is well modeled by using $f = 0.1$ (harmonic). We note that the coronal temperature increases with flux limitation (as less heat is allowed into the overdense plasma) so that we also obtain better agreement for the laser absorption fraction φ, i.e., $\varphi_{FP} = 0.74$, $\varphi_c = 0.78$ and $\varphi\,(f = 0.1) = 0.73$. Such a result is typical for simulations with short-wavelength lasers (<1 μm) at moderate intensities (<10^{15} W/cm^2).[4,15]

The above simulation has been repeated by applying a small modulation in the x direction to the incident laser intensity of the form $\sin(kx)$, where $\lambda_\perp = 2\pi/k = 10$ μm. Figure 42.5 shows the calculated root-mean-square (rms) temperature deviation at 100 ps defined by

$$\sigma = \left\{\left[\int dx (T - \langle T\rangle)^2\right] / \int dx\right\}^{1/2} \langle T\rangle^{-1},$$

where $\langle T \rangle$ is the average temperature. All plots have been normalized to the rms laser intensity. Axial and transverse heat flow, normalized to q_f, are shown in Figs. 42.6(a) and 42.6(b), respectively. Here, q_c is calculated using the FP temperature profiles.

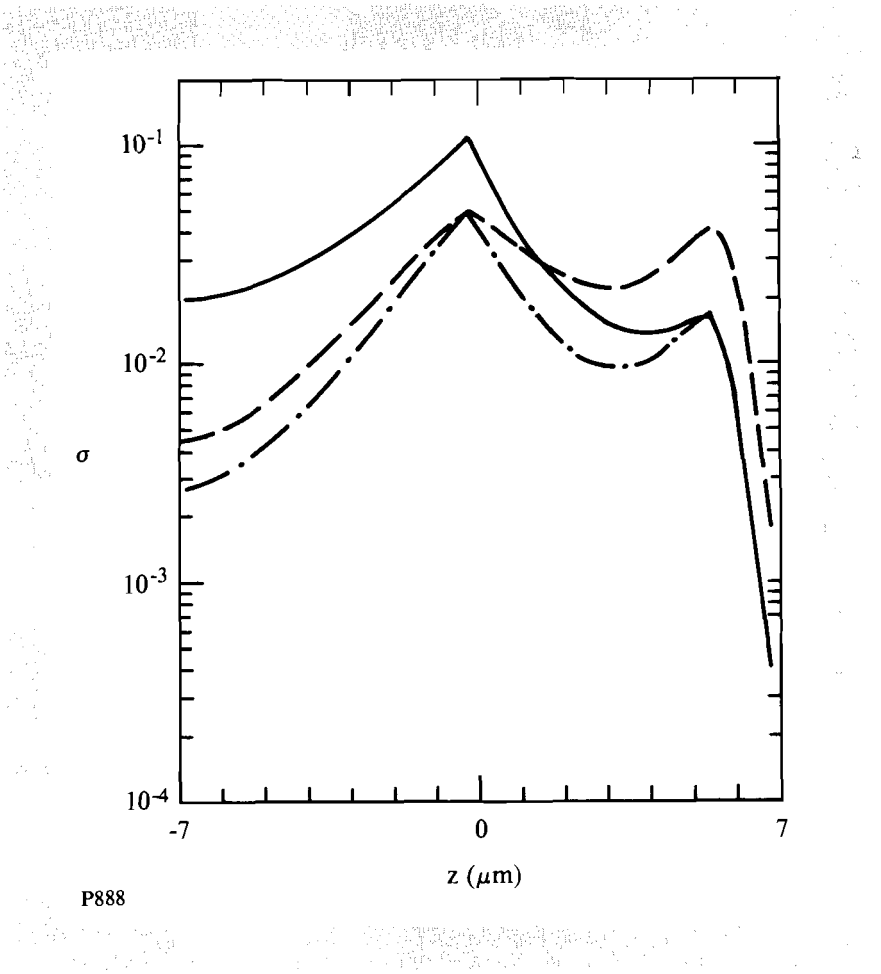

Fig. 42.5
Plot of the rms temperature deviation (normalized to the rms laser-intensity deviation) as a function of z. Curves are identified as in Fig. 42.1.

Despite the good agreement between fluid and kinetic results for the 1-D temperature profiles, the same is not true for the transverse spatial modulation. Nonlocal transport gives rise to less smoothing in the corona and an enhancement at higher densities. Both these regimes are now discussed in turn. To characterize the coronal smoothing, the ratio σ_{FP}/σ_c is calculated at the critical surface and the result is plotted in Fig. 42.7 as a function of $\lambda_\perp$. The increase of σ_{FP}/σ_c as $\lambda_\perp \to 0$ is a consequence of lateral heat-flux inhibition, of the type discussed in the previous section for the special case of a homogeneous plasma. For a more quantitative demonstration of this effect we first assume that $S \sim ik(q_{FP})_x \sim ik(q_c)_x$ in the corona, where S is the laser energy deposition rate. Using the definition $\kappa_{FP} = -(q_{FP})x/ik\delta T_{FP}$, we find that $\kappa_{FP}/\kappa_c \sim \delta T_c/\delta T_{FP} \sim (\sigma_{FP}/\sigma_c)^{-1}$, allowing us to plot κ_{FP}/κ_c as a function of $\lambda_\perp/(2\pi\lambda_d)$ in Fig. 42.2 (full circles), where $\lambda_d = 0.75\ \mu$m at the critical surface. This occurrence of reduced coronal thermal smoothing

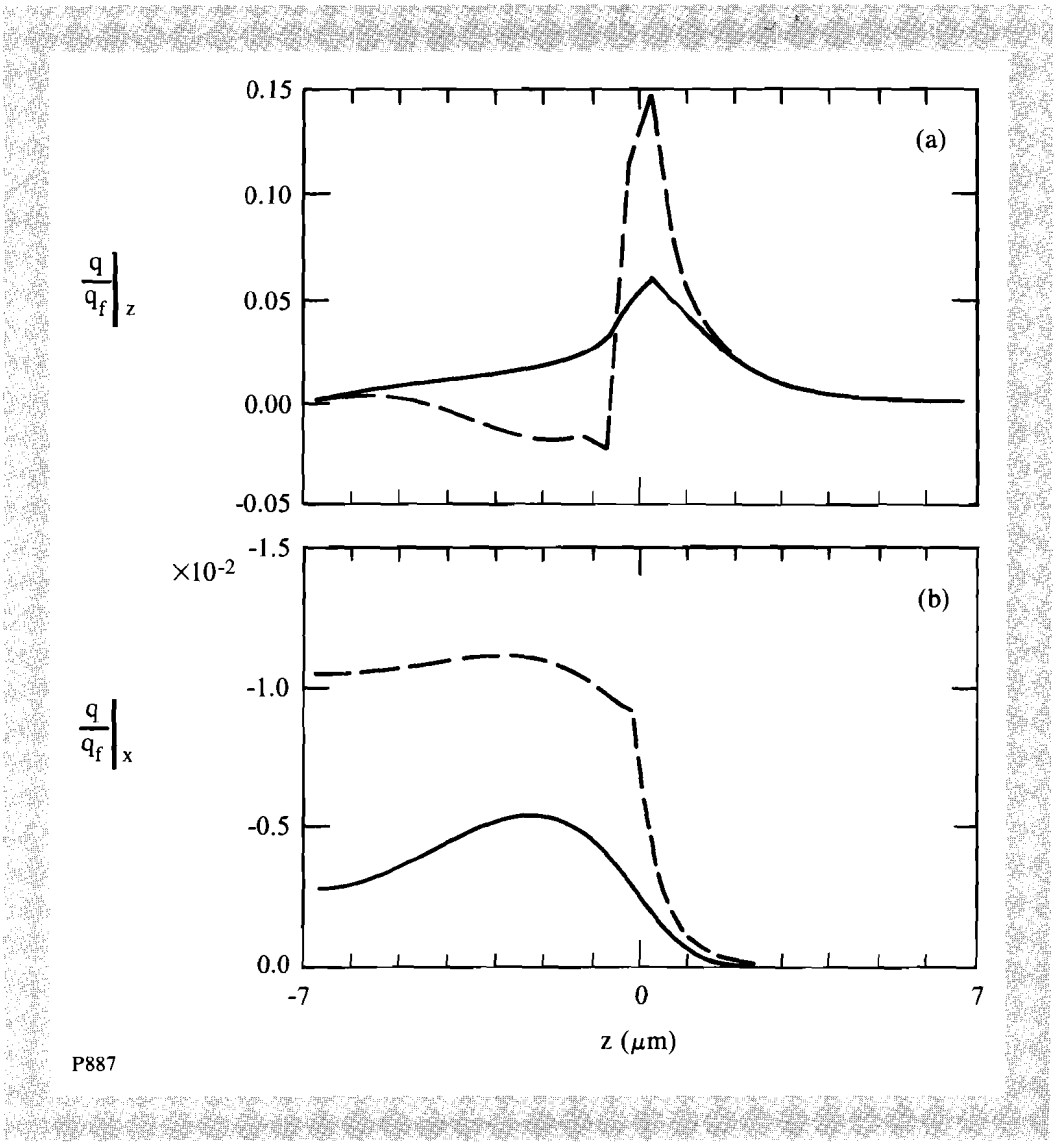

Fig. 42.6
Plot of heat flow (normalized to q_f) in the (a) z direction (axial) and in the (b) x direction (transverse) at $x = 0$, as functions of z. Here, solid curves refer to q_{FP}, whereas dashed curves refer to q_c using FP temperatures.

in longer-scale-length plasmas irradiated by higher intensities has been previously reported by Epperlein *et al.*[5]

The clue for the enhanced smoothing at high densities lies in the axial flux inhibition near critical [see Fig. 42.6(a)]. This acts to reduce the effective flow of thermal modulation away from the critical surface to the overdense plasma. By applying a flux limiter we can reproduce this effect to some extent as shown in Fig. 42.7. The enhancement of lateral thermal smoothing due to axial flux inhibition was first predicted by Skupsky,[19] using a crude steady-state fluid model. More recently Rickard *et al.*[20] used a FP code to predict a large increase in thermal smoothing in the long-wavelength ($\lambda_\perp$)

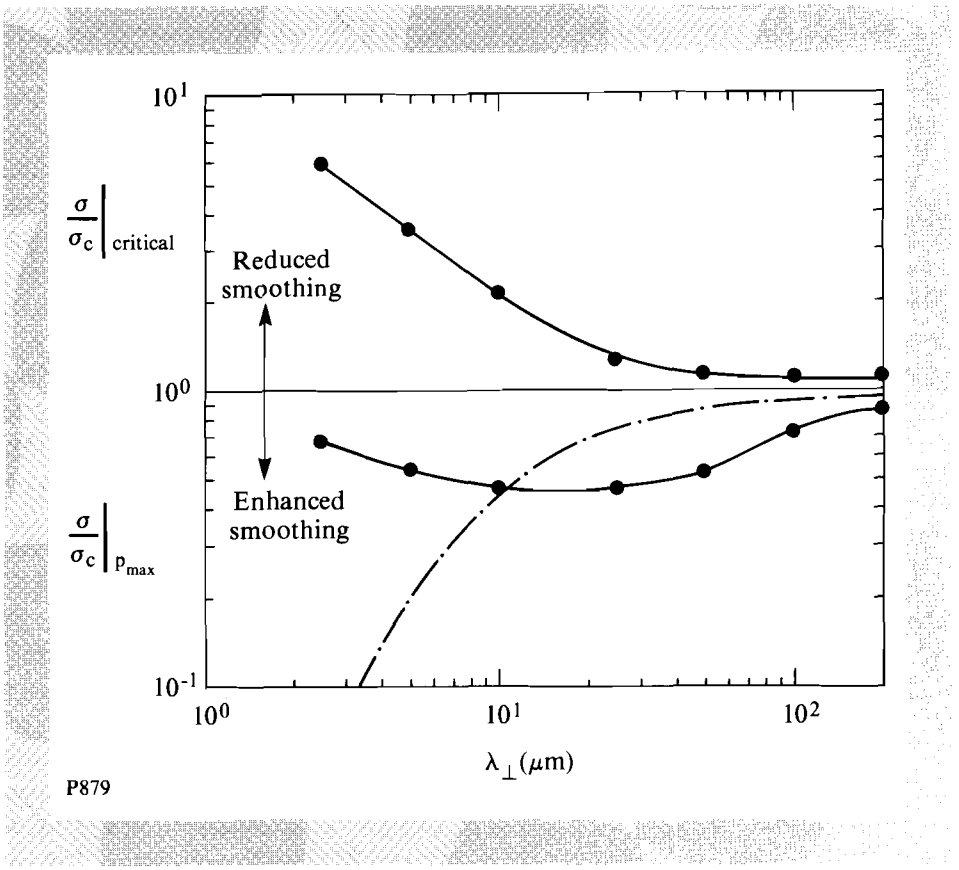

Fig. 42.7
Plot of σ_{FP}/σ_c (solid curves) and $\sigma^*(f=0.1)/\sigma_c$ (dash-dotted curve) as functions of $\lambda_\perp$ (μm), calculated at $n_{critical}$ and at maximum pressure.

limit. They used, however, a much higher laser intensity (10^{15} W/cm^2) that gave rise to a much stronger axial flux inhibition and hence reduced thermal modulation at high densities. Here we calculate σ_{FP}/σ_c where pressure is a maximum p_{max} (~4.4 μm away from the critical surface) and obtain only a modest enhancement in smoothing at large wavelengths, as seen in Fig. 42.5. We do, however, predict that for a wide range of $\lambda_\perp$ (6 μm – 40 μm), $\sigma_{FP}/\sigma_c \sim 0.5$, which represents a factor of ~2 improvement in pressure uniformity at p_{max}. At smaller wavelengths the reduced lateral smoothing at critical starts to dominate and the value of σ_{FP}/σ_c increases again. (In practice this is relatively unimportant since at p_{max}, we find that $\sigma < 10^{-2}$ for $\lambda_\perp < 6$ μm.) These effects are not accurately modeled with flux-limited classical transport as shown in Fig. 42.7 by plotting $\sigma(f=0.1)/\sigma_c$.

Conclusions

Care must be taken when interpreting transport data using flux-limited classical heat conduction. For short-wavelength lasers (<1 μm) at moderate intensities (<10^{15} W/cm^2) a fluid model provides an adequate description of the transport under uniform illumination conditions. A modest amount of flux limitation ($f \sim 0.1$) is then sufficient to fine tune the results. However,

one must be aware that classical transport (flux limited or otherwise) cannot model preheat because of the long-mean-free-path electrons. In the FP simulations presented here this issue was not addressed satisfactorily because of the relatively high initial plasma temperatures. Mima *et al.*[21] have recently shown, using a 1-D FP code coupled to a Lagrangian fluid solver, that preheat can significantly degrade the performance of thin low-Z shell targets irradiated by 0.53-μm laser light. The magnitude of this effect is expected to be less for shorter-wavelength lasers, by virtue of the higher collisionality of the plasma, though the exact extent remains to be investigated.

When simulating 2-D transport, which may arise as a result of nonuniform laser irradiation, nonlocal effects can drastically alter the results, even when the average 1-D transport appears well modeled by fluid theory. The main consequences of nonlocal transport are given as follows:

1. A severe reduction in the coronal thermal smoothing for spatial modulations less than about 200 $(Z + 1)^{1/2}\lambda_t$.

2. An enhancement in the smoothing at high densities, especially near the pressure maximum, for all spatial modulations.

The first consequence is well explained in terms of flux inhibition of short-scale modulations in a homogeneous plasma. Its main impact would be to reduce the threshold for thermal self-focusing instabilities[22] or any other instabilities that rely on coronal temperature modulations.

The second result arises from the axial flux inhibition from the critical density to higher densities, which acts to reduce the propagation of thermal modulations. The scaling of this phenomenon with plasma and laser conditions has not been fully investigated, nor has the issue of hydrodynamic feedback been addressed. However, the simulations presented here suggest the possibility of a two-fold increase in smoothing (when compared with classical heat-flow modeling) over a wide range of modulation wavelengths. Such an outcome is potentially very beneficial to ICF since, for a given nonuniformity in the incident laser, it predicts a smoother ablation pressure and less chance for seeding hydrodynamic instabilities.

ACKNOWLEDGMENT

This work was supported by the U.S. Department of Energy Division of Inertial Fusion under agreement No. DE-FC03-85DP40200 and by the Laser Fusion Feasibility Project at the Laboratory for Laser Energetics, which has the following sponsors: Empire State Electric Energy Research Corporation, New York State Energy Research and Development Authority, Ontario Hydro, and the University of Rochester.

REFERENCES

1. J. Nuckolls, L. Wood, A. Thiesen, and G. Zimmerman, *Nature* **239**, 139 (1972).
2. L. Spitzer, Jr. and R. Härm, *Phys. Rev.* **89**, 977 (1953).
3. D. R. Gray and J. D. Kilkenny, *Plasma Phys.* **22**, 81 (1980).

4. A. R. Bell, R. G. Evans, and D. J. Nicholas, *Phys. Rev. Lett.* **46**, 243 (1981); J. P. Matte and J. Virmont, *ibid.* **49**, 1936 (1982); J. R. Albritton, *ibid.* **50**, 2078 (1983); T. H. Kho, D. J. Bond, and M. G. Haines, *Phys. Rev. A* **28**, 3156 (1983); J. P. Matte, T. W. Johnston, J. Delettrez, and R. L. McCrory, *Phys. Rev. Lett.* **53**, 1461 (1984); J. F. Luciani, P. Mora, and R. Pellat, *Phys. Fluids* **28**, 835 (1984); A. R. Bell, *ibid.* **28**, 2007 (1985); and S. Jorna and L. Wood, *J. Plasma Phys.* **38**, 317 (1987).

5. E. M. Epperlein, G. J. Rickard, and A. R. Bell, *Phys. Rev. Lett.* **61**, 2453 (1988).

6. E. M. Epperlein, G. J. Rickard, and A. R. Bell, *Comput. Phys. Commun.* **52**, 7 (1988); G. J. Rickard, A. R. Bell, and E. M. Epperlein, *Phys. Rev. Lett.* **62**, 2687 (1989).

7. R. C. Malone, R. L. McCrory, and R. L. Morse, *Phys. Rev. Lett.* **34**, 721 (1975).

8. J. Delettrez, *Can. J. Phys.* **64**, 932 (1986).

9. W. L. Kruer, *The Physics of Laser Plasma Interactions* (Addison-Wesley, Redwood City, CA, 1988).

10. I. P. Shkarofsky, T. W. Johnston, and M. P. Bachysnky, *The Particle Kinetics of Plasmas* (Addison-Wesley, London, 1966).

11. E. M. Epperlein and M. G. Haines, *Phys. Fluids* **29**, 1029 (1986).

12. D. Shvarts, J. Delettrez, R. L. McCrory, and C. P. Verdon, *Phys. Rev. Lett.* **47**, 247 (1981).

13. E. M. Epperlein, *Plasma Phys. & Controlled Fusion* **27**, 1027 (1985).

14. A. B. Langdon, *Phys. Rev. Lett.* **44**, 575 (1980).

15. J. F. Luciani, P. Mora, and J. Virmont, *Phys. Rev. Lett.* **51**, 1664 (1983); J. R. Albritton, E. A. Williams, I. B. Bernstein, and K. P. Swartz, *ibid.* **57**, 1887 (1986); P. A. Holstein, J. Delettrez, S. Skupsky, and J. P. Matte, *J. Appl. Phys.* **60**, 2296 (1986).

16. A. R. Bell, *Phys. Fluids* **26**, 279 (1983).

17. M. K. Prasad and D. S. Kershaw, *Phys. Fluids B* **1**, 2430 (1989).

18. J. Delettrez (private communication).

19. S. Skupsky, LLE Report **131** (1982).

20. G. J. Rickard, I. R. G. Williams, and A. R. Bell, presented at the 19th Annual Anomalous Absorption Conference, Durango, CO, June 1989.

21. K. Mima *et al.*, *Laser and Part. Beams* **7**, 487 (1989).

22. E. M. Epperlein, presented at the 19th Annual Anomalous Absorption Conference, Durango, CO, June 1989.

1.B Fabrication of Plastic Shells

Low-atomic-number ablators are a requirement in future direct-drive high-gain capsule designs to reduce preheat; hence, they produce a more efficient compression of the fuel. In the short term, experiments are being planned on OMEGA to investigate the hydrodynamic behavior of capsules with plastic ablators. In this article we will describe the microencapsulation technique now being used to produce the required large numbers of high-quality uniform-thickness plastic shells. The preferred polymer material for production of low-atomic-number capsules is polystyrene due to its chemical and physical stability and its easy processability. Furthermore, it is easily soluble in many common organic solvents at room temperature.

Two methods—both utilizing a polystyrene solution—are commonly used to fabricate polymer shells. In the drop-tower technique,[1] a single-orifice droplet generator is mounted atop a polymer-shell-drying column that has several independently controlled temperature zones. Droplets of polystyrene solution from the generator fall through the column during which time solvent in the outer region of the droplets evaporates and solvent inside is driven off to inflate the shell. The drop-tower method has not yet, however, been able to fabricate polymer shells with wall-thickness uniformity comparable to that of glass shells.

Microencapsulation, the second method, was developed by U. Kubo[2] of Kinki University, Japan in 1981. A schematic of the process is illustrated in Fig. 42.8. Polystyrene solution and water are rapidly agitated in a small closed vial to produce an emulsion of water droplets suspended in the polystyrene solution. This emulsion is then poured into heated and agitated water containing a polyvinyl alcohol (PVA) surfactant into which the emulsion dispenses forming droplets of water surrounded by a thin spherical layer of polystyrene solution. The temperature is then raised to accelerate the evaporation of solvent from the polystyrene. This results in solid polystyrene shells that contain pure water. These shells are then rinsed in pure water to remove residual PVA surfactant and air dried to remove internal water.

Microencapsulation has been extensively refined at Osaka University's Institute of Laser Engineering (ILE) to the extent that they are currently capable of producing target-quality polymer shells.[3] ILE now fabricates not only polystyrene shells but also deuterated polystyrene and polytrimethyl silylstyrene shells.[3] Using ILE's procedure as a general guideline, LLE has developed a process that yields target-quality polystyrene and deuterated polystyrene shells in large quantity. While ILE's and LLE's methods of fabrication are essentially the same during initial stages of processing, they differ in the method of water removal from the shell interior. In the ILE process, shells are rinsed with pure water and air dried in a filter funnel until all interior water has permeated through the shell wall. While this process does produce uniform shells, many are cracked, perhaps due to water permeating through the shell wall too rapidly. The process results in the

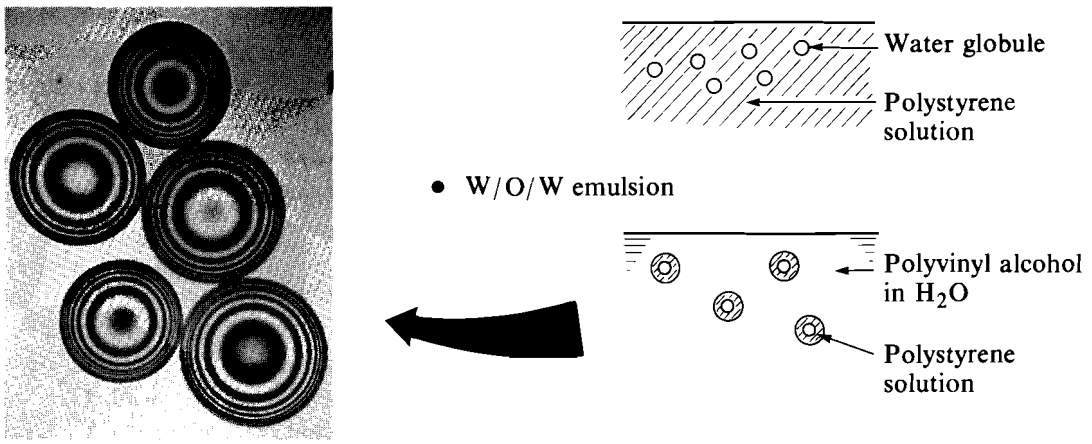

Fig. 42.8
Schematic of microencapsulation technique of forming plastic shells. W/O (water in oil) emulsion is first formed in which water globules are dispersed in polystyrene solution. This is followed by a W/O/W emulsion in which shells of polystyrene solution containing water are dispersed in polyvinyl alcohol solution in water.

time-consuming operation of optically inspecting each shell for cracking. In the LLE process, shells are rinsed in pure water to remove residual PVA and then placed in a dilute mixture of ethanol and water. This allows for accurate rate control of water removal from the interior of the shells via osmotic action. This can be accomplished because styrene is highly permeable to water, while being impermeable to ethanol. Although some shells still crack during water removal, they are automatically removed from the batch because they sink. Only shells that do not crack or have very minor cracks float to the surface where they are removed by pipette and placed in a grid to complete drying in a vacuum oven.

In practice, polystyrene solutions are made using polystyrene fractions having a narrow molecular-weight distribution, either alone or in combination with other molecular-weight fractions. These molecular-weight fractions are typically in the 100,000–600,000 range. Similarly, the solutions are made in a variety of weight percentages ranging from 3 to 7 wt.%. The PVA solution is made using 25,000-molecular-weight polymer at 5 wt.% concentration. A 50/50 volume ratio of benzene and ethylenedichloride is the solvent used for polystyrene. Both the polystyrene and PVA solutions are filtered to 0.2 μm to reduce contamination in the shell wall and on its surface. Approximately 8 cc of filtered polystyrene solution is prepared in

a 15-cc vial. This is capped and heated to ~50°C for a period of 2 h to allow the polymer to degas. After cooling to room temperature, 4 cc of filtered water is placed in the vial. The mixture is recapped and shaken vigorously by hand for 10 s. The resulting emulsion is poured rapidly into the heated PVA solution that is agitated by a downward pushing propeller-type stirrer rotating at ~400 rpm. After ~10 s, the propeller speed is reduced to 200 rpm. At this time the PVA bath temperature is raised from its initial temperature of 72°C to a final temperature of ~85°C. After ~3 h at the elevated temperature, all of the benzene and dichloroethane is removed and the shells are rinsed, sieved, and placed in the alcohol/water solution for interior-water removal.

Plastic shells are target quality if they meet the three following conditions: (1) the shells are spherical and the wall is of uniform thickness; (2) the rms surface roughness is less than 1 μm; and (3) the density of the shell wall is uniform, i.e., no vacuoles are present in the shell wall. Generally, a single batch contains up to several thousand shells and 10% to 50% of them are "target quality" shells. Figure 42.9 shows Mäch-Zehnder interferograms of polystyrene shells of different sizes (diameters of 216 μm, 265 μm, 373 μm, and 640 μm). These shells are from a single batch and in any given batch, the shell size ranges, in general, from 100 to 700 μm. The wall thickness

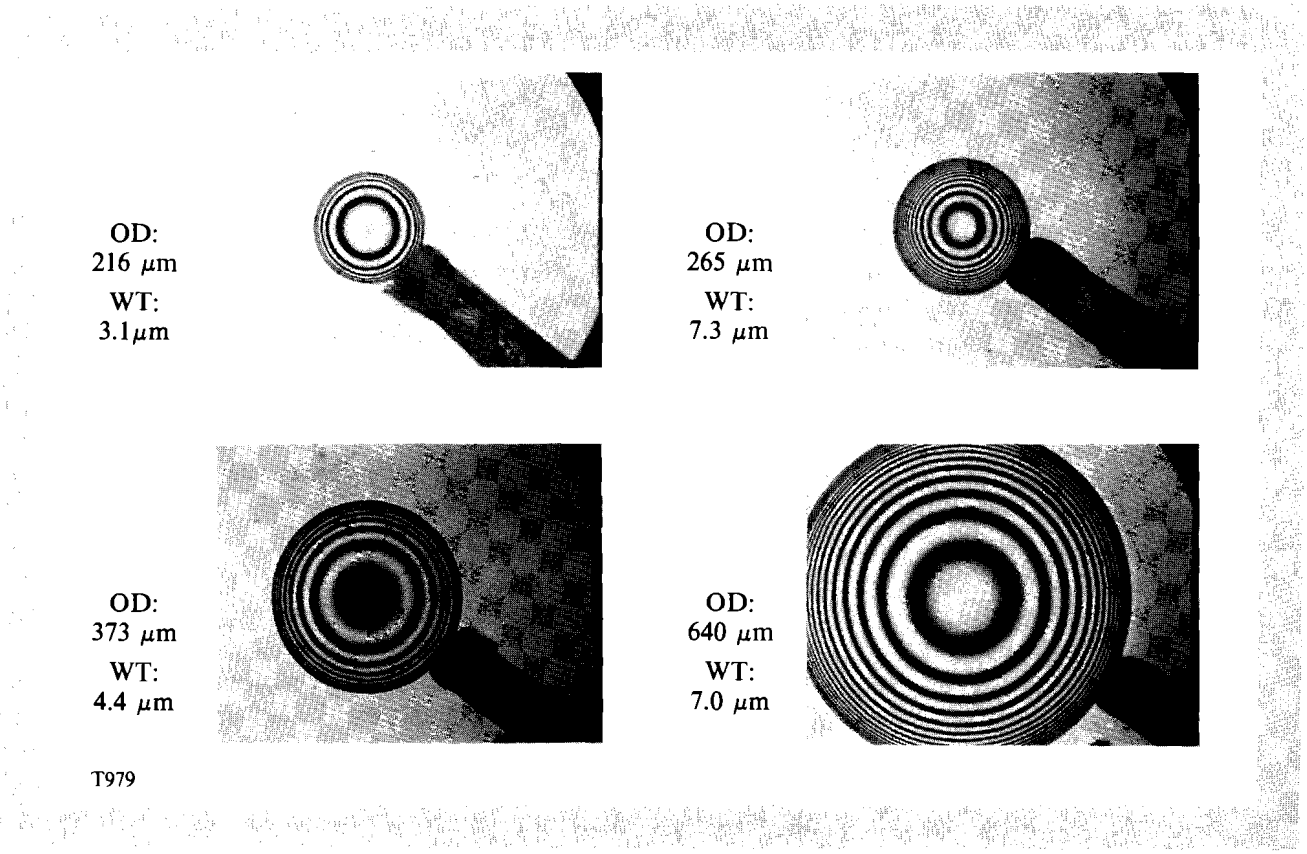

Fig. 42.9
A typical batch of polystyrene shells with a wide range of sizes and wall thicknesses.

ranges from 2 to 7 μm. Production of sizes and wall thicknesses of the shells outside the above-described ranges may require further study. Concentricity of the shells was analyzed by comparing the interferograms from two orthogonal views with templates generated by a ray-tracing computation. Figure 42.10 shows a Mäch-Zehnder interferogram, a template, and their superposition. From this comparison, this particular shell is shown to have a nonconcentricity of 2%, which is well within the acceptable range of 5%. Figure 42.11 is a scanning electron microscope (SEM) photo of a shell showing the surface finish. The object in the middle of the photo is believed to be a dust particle deposited on the surface. The surface is very smooth with an rms finish much smaller than 1 μm. Although not all shells have such a smooth surface finish, a sufficient number of shells of good surface quality can be selected from any given batch.

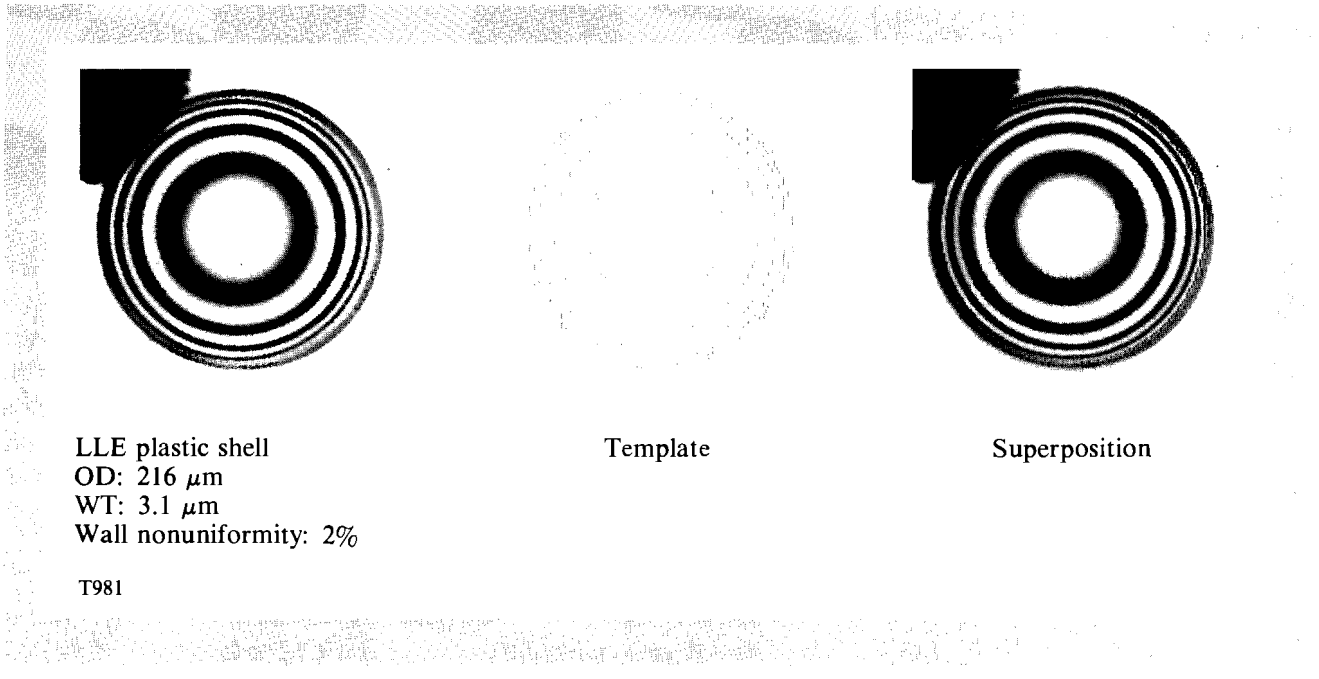

Fig. 42.10
Characterization of a polystyrene shell. Interferogram is superposed onto a template calculated from a ray-tracing program. From this comparison, the shell is shown to have a nonconcentricity of 2%.

Nonuniformity of plastic shell density is generally caused by the presence of vacuoles in the wall that can be incorporated during the fabrication process. In fact, problems with vacuoles caused the abandonment of some early attempts to develop the microencapsulation technique.[4] However, in our experiments, it was found that the number of vacuoles can be reduced or eliminated by simply degassing the polymer and reducing the size of the container holding the mixture of water and polymer solution. Optical microscopy is utilized to detect the vacuoles in the shell. When a shell is illuminated with plane-parallel wave fronts, the transmitted rays either converge or diverge depending upon whether the defect is surface debris or vacuoles embedded in the shell, respectively. Therefore, by focusing

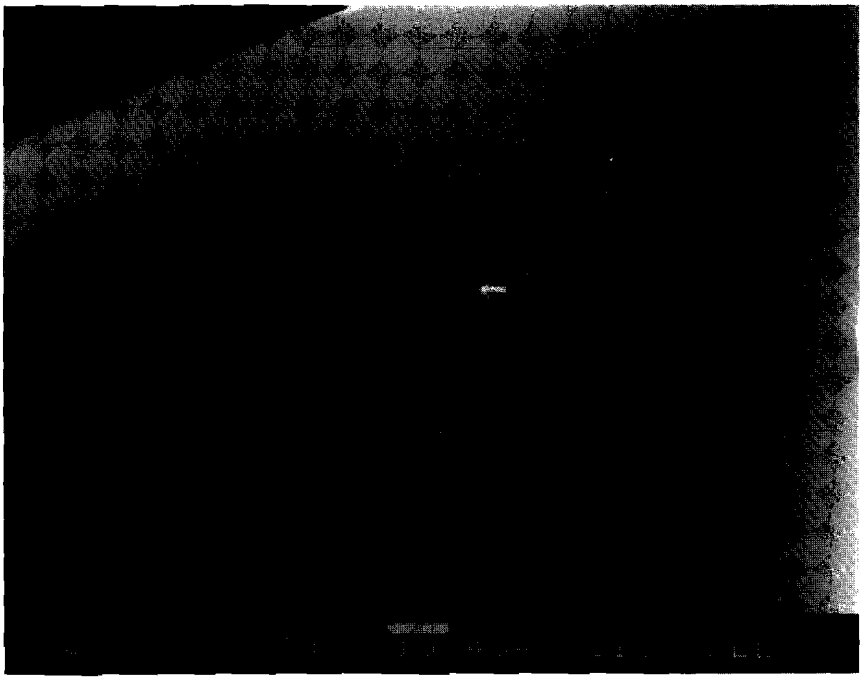

T980

Fig. 42.11
Surface finish of a polystyrene shell. The defects in the surface are artifacts.

through the object plane and noting whether the bright point of light appears above or below the plane in which the object is clearly in focus, one can easily differentiate between surface debris or vacuoles. However, because of the refractive effects of the shell wall itself, this technique is useful only for regions of the shell on which the light from the condenser is normally incident. The shell must therefore be rotated to examine it entirely. Typical polymer shells produced at LLE contain only a few vacuoles, if any, which are of the order of up to several microns in diameter.

In summary, using the microencapsulation technique, it is possible to fabricate a large number of polystyrene shells. The fabricated shells have very uniform wall thickness, smooth surface finish, and few vacuoles embedded in the wall. The size and wall thickness of the shells range from 100 to 700 μm and from 2 to 7 μm, respectively. We have also succeeded in fabricating deuterated polystyrene shells. Since deuterated and protonated polystyrenes are chemically identical, the same procedure also produced target-quality deuterated polystyrene shells. This present work will be expanded to fabricate the large-size shells needed for OMEGA Upgrade experiments and plastic shells containing Si, Cl, or other elements.

ACKNOWLEDGMENT

This work was supported by the U.S. Department of Energy Division of Inertial Fusion under agreement No. DE-FC03-85DP40200 and by the Laser Fusion Feasibility Project at the Laboratory for Laser Energetics, which has the following sponsors: Empire State Electric Energy Research Corporation, New York State Energy Research and Development Authority, Ontario Hydro, and the University of Rochester.

REFERENCES

1. A. K. Burnham, J. Z. Grens, and E. M. Lilley, *J. Vac. Sci. Technol. A* **5**, 3417 (1987).

2. U. Kubo, M. Nakatsuka, and M. Tsubakihara, Annual Progress Report, ILE, Osaka University, ILE-APR-79 (1979), p. 177.

3. S. Nakai *et al.*, "High Density Compression of Hollow-Shell Target of GEKKO XII and Laser Fusion Research at ILE, Osaka University," to be published in *Laser Interaction and Related Plasma Phenomena.*

4. KMS Fusion Annual Technical Report, KMSF-U-1728 (1985), p. 73.

Section 2
ADVANCED TECHNOLOGY DEVELOPMENTS

2.A Observation of Gain on XUV Transitions in Ne-like and Li-like Ions

Population inversion and amplified spontaneous emission (ASE) at soft x-ray wavelengths have been achieved using two methods of pumping: collisional and recombinational. In the collisionally excited x-ray laser, thermal electrons in the plasma excite ions to the upper laser state, which is a forbidden radiative transition to the ground state but is easily excited by collisions and dielectronic recombinations. Population therefore accumulates in the upper state while the lower laser level is depopulated by a rapid radiative transition rate. The first collisionally pumped laser was demonstrated by Lawrence Livermore National Laboratory (LLNL)[1] in Ne-like Se and has been extensively studied in various other elements and extended to several Ni-like species.[2] These experiments use thin exploding-foil targets to ensure that refraction effects are minimized. The pump laser burns through the target foil near the peak of the pulse, causing the foil to explode symmetrically. The resulting density profile is relatively flat in the central region and falls off in both directions along the incident laser axis. This allows x rays to propagate along the axis of the plasma and be significantly amplified before leaving the plasma.

Collisionally excited x-ray lasing can also be produced using slab targets.[3] In this case, the target thickness is such that the pump laser does not burn through the target during the pulse. This gives rise to a steep density gradient in the direction of the incident laser because the target mass is not depleted and a region of solid density persists for the duration of the laser

pulse. Since there is no axis of symmetry in the density profile, all rays suffer refraction away from the target. This behavior was originally thought to be a severe detriment to the attainment of gain. The results of Ref. 3 are thus unexpected and merit further study.

We have carried out experiments that utilize slab targets and produce lasing in Ne-like Ge, using lower laser energy than in previous experiments. The wavelengths of the five lasing lines range from 196 Å to 287 Å. We will show the scaling of the laser output with target length and present measurements of the divergence of this x-ray laser.

In a recombination-pumped laser the mean ionization of the plasma is higher than that of an equilibrium plasma at the same temperature. In this nonequilibrium condition, which occurs following a rapid cooling, three-body recombination and radiative cascading dominate over collisional ionization and excitation processes. This tends to populate the upper levels (e.g., $4f$ and $5f$ in Li-like ions) more than the lower excited states, thus creating an inversion. Furthermore, the lower level ($3d$) has a short lifetime because of a strong radiative transition to the ground state.[4]

This nonequilibrium situation is typically created by heating the plasma with a short laser pulse and then allowing it to cool in a time that is short compared to the recombination time for the ions involved. Since the recombination time for ions of interest (i.e., lasing at wavelengths <200 Å) is of the order of tens of picoseconds, these types of experiments usually require laser pulses shorter than 100 ps. Such experiments have produced various types of recombination lasing.[5] In long-pulse experiments, any lasing occurs while the pump laser is heating the plasma; therefore, it must occur far from the target surface where the plasma absorbs very little laser energy and is thus able to cool quickly. At this point, collisional excitation and ionization (dominant in the region heated by the laser) are insignificant compared to recombination.

Recent results by Hara *et al.*[6] have shown that the intensity of the $3d$–$4f$ and $3d$–$5f$ lines of Li-like Al increases exponentially with length in experiments using very-low-power, 5-ns laser pulses. We present results of experiments with Li-like Al performed at somewhat higher intensities than reported in Ref. 6 and show apparent ASE of the lines at 105 Å and 154 Å. We also present results that extend the Li-like scheme to shorter wavelengths, i.e., a Li-like Ti transition at 47 Å. The Ti experiments also showed a lasing line at 326.5 Å that has been tentatively identified as transition in Ne-like Ti.[7] Finally, we present angular-distribution measurements of the output of these x-ray lasers.

Experimental Configuration

At LLE experiments were performed using the glass development laser (GDL).[8] The targets were irradiated with 650-ps pulses of 1054-nm light at various intensities. The line focus was produced by the addition of a cylindrical corrector lens to the f/3 spherical focus lens normally used in

laser-plasma interaction experiments. To produce sufficient excitation of the $3p$ state in the Ne-like Ge ion (of excitation energy 1480 eV), a temperature in the range of 600 eV–1000 eV is required. Such temperatures are produced using on-target intensities of $\sim 2 \times 10^{13}$ W/cm^2 as evidenced by the observation of Ne-like lines in the x-ray and XUV spectra.

A grazing incidence grating spectrometer (GIGS) is used to view the plasma end-on to detect the output of the x-ray laser, as shown in Fig. 42.12. The spectrometer has an acceptance angle of ~20 mrad in the direction along the entrance slit and a focusing mirror provides a collection angle of ~1 mrad perpendicular to the slit. A crystal spectrometer and an x-ray pinhole camera are used to measure the x-ray spectrum and the intensity distribution of the optical laser at line focus, respectively. All diagnostics are time integrated and use film for recording. Kodak 2497 film is used in the pinhole and crystal spectrometer; Kodak 101 film is used in the GIGS. An advantage of using film in the GIGS rather than three narrow strips of microchannel plate as used in Refs. 1 and 2 is that a more complete record of the angular output intensity perpendicular to the dispersion direction is obtained on film.

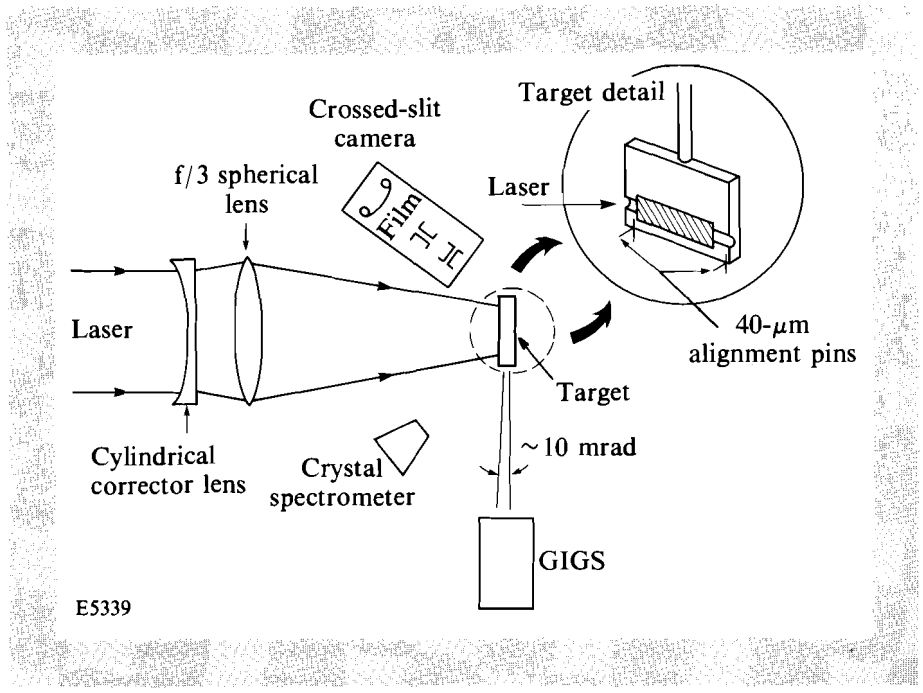

Fig. 42.12
The experimental configuration for x-ray laser experiments on GDL. The insert depicts an x-ray laser target with glass-fiber alignment pins.

Gain measurements are performed by comparing the output intensity from targets of different length. The target length is varied by using different target slab lengths while maintaining the laser line-focus length. This ensures that variations caused by laser irradiance differences are kept to a minimum since the targets sample only the central region of the beam. For example, the longest targets (22 mm) are overfilled by the line focus

by ~2 mm. The x-ray and XUV film densities are converted to intensity using x-ray calibration data.[9] The reflectivity of the grating and collection mirror has not been absolutely calibrated; all intensities are therefore in relative units.

Results

1. Ne-like germanium

The Ge targets consist of 125-μm Mylar foil coated with ≥1-μm GE thickness, which is much larger than the heat-front penetration depth. The Mylar backing serves to provide a resilient support ensuring the flatness of the Ge surface. Segments of 40-μm glass fibers are used as alignment reference pins to be imaged in the target alignment microscope as shown in the inset of Fig. 42.12. Using these pins and the edge of the target enables us to align the target, spectrometer, and line-focus axes to better than 5-mrad accuracy.

The presence of gain and the effect of laser length on x-ray laser output are demonstrated in Figs. 42.13 and 42.14. Figure 42.13 shows similar regions of the XUV spectra (from GIGS) from two different target lengths. Both spectra are shown after conversion to relative intensity. Note that for the 10-mm-long targets the lasing lines are barely discernible (J = 2→1

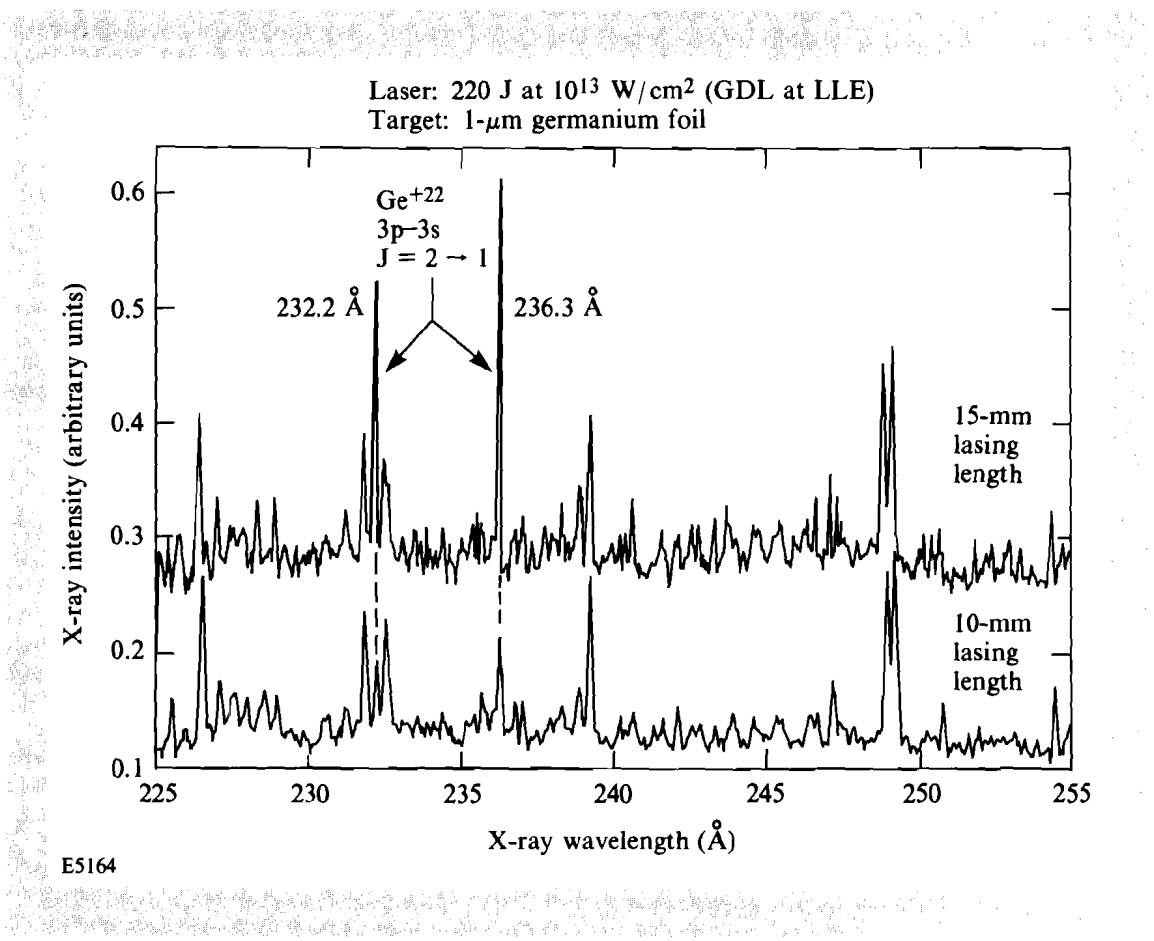

Fig. 42.13
A comparison of the output intensity of the J = 2–1 Ge^{+22} lines (232 Å and 236 Å) for two x-ray laser lengths. The lower spectrum is for a 10-mm plasma length and the upper spectrum is for a 15-mm length.

at 232 Å and 236 Å), whereas for the 15-mm length the lines begin to be the dominant features in the spectrum. For line foci shorter than 10 mm, the lasing lines could hardly be seen.

If the line focus is extended to 22 mm, the lasing lines become the brightest lines in the spectrum. Figure 42.14 shows the Ge spectrum (from GIGS) in the range of ~20 Å–380 Å from a 22-mm-long target irradiated at an intensity of 1.5×10^{13} W/cm^2. The lasing lines of Ne-like Ge are labeled (a) to (e) and correspond to the designation in Table 42.I. The nonlasing lines have approximately the same intensity as those in the shots of Fig. 42.13. The carbon K absorption edge can be seen at 43.6 Å and results from the carbon in the film emulsion and impurity coatings on the GIGS optics.

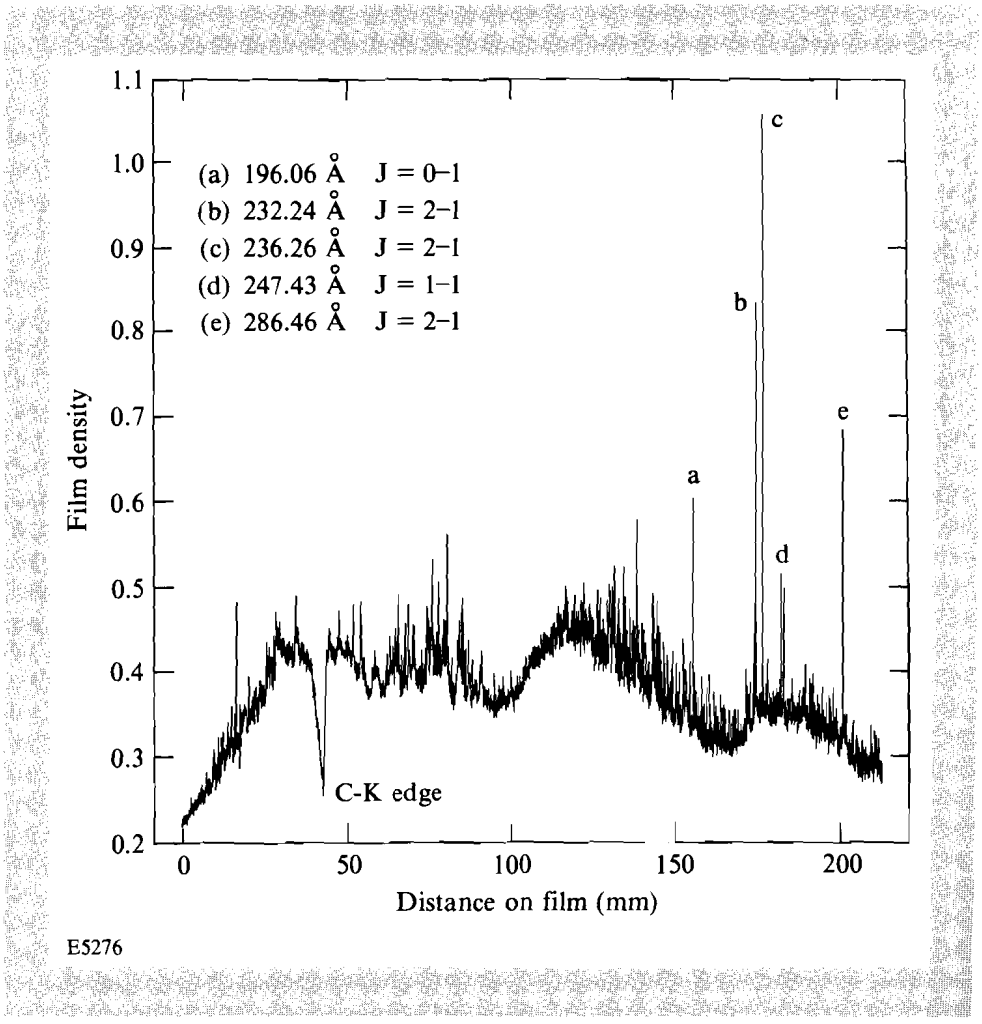

Fig. 42.14
A wide range of the spectrum from a 22-mm-long Ge x-ray laser target. The lines designated (a) – (e) are the various $3p$–$3s$ lasing lines observed in Ne-like Ge.

Figure 42.15 is a plot of the relative intensity I of the J = 2–1 lasing line at 236 Å as a function of the Ge target length ℓ. The data points are obtained from different shots that had nominally the same optical laser conditions (±10%). The solid curve is a best fit of the analytic expression

$$I \propto \left[\exp(g\ell) - 1\right]^{3/2} / \left[(g\ell)\exp(g\ell)\right]^{1/2} \quad (1)$$

to the data. From this we derive the gain coefficient g. This method was likewise applied to the other lasing lines. The resulting gains are shown in Table 42.I.

Table 42.I: Lasing lines and their designations.

Designation	Transition	Wavelength (Å)	Gain (cm^{-1})
(a)	$(2p^5{}_{1/2}3p_{1/2})_0 - (2p^5{}_{1/2}3s_{1/2})_1$	196.06	1.5
(b)	$(2p^5{}_{3/2}3p_{3/2})_2 - (2p^5{}_{3/2}3s_{1/2})_1$	232.24	2.5
(c)	$(2p^5{}_{1/2}3p_{3/2})_2 - (2p^5{}_{1/2}3s_{1/2})_1$	236.26	2.5
(d)	$(2p^5{}_{3/2}3p_{3/2})_1 - (2p^5{}_{3/2}3s_{1/2})_1$	247.32	1.0
(e)	$(2p^5{}_{3/2}3p_{1/2})_2 - (2p^5{}_{3/2}3s_{1/2})_1$	286.46	1.8

E5593

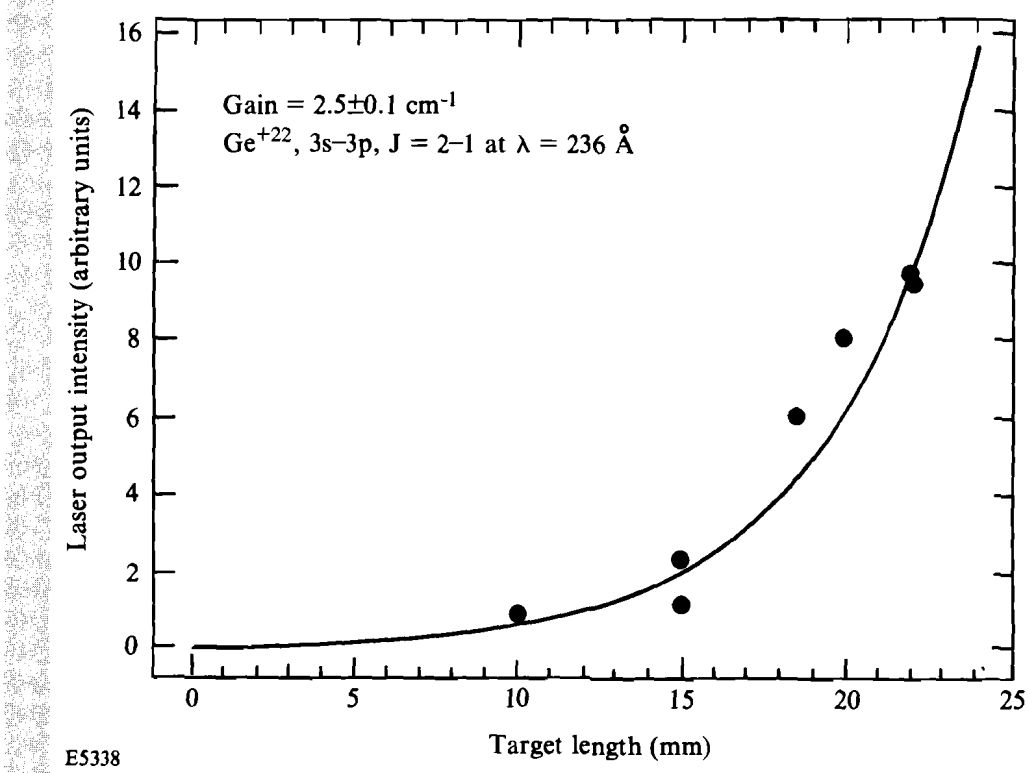

Fig. 42.15
Intensity of the 236-Å line of Ge^{+22} versus target length. The gain is obtained from the solid curve, which is a fit of Eq. (1) to the experimental points.

The angular width of the x-ray laser output can be measured using GIGS. Since the output beam of the x-ray laser is of limited extent (~200 μm) and narrow (~10 mrad), the rays fill only a portion of the entrance slit of the spectrometer and are relayed to the film plane as a narrow beam. Providing the acceptance angle of the spectrometer is greater than the x-ray laser divergence, only a limited length of the film is exposed by the lasing line. In contrast, spontaneously emitted x rays are isotropic, fill the slit, and form a spectral line extending across the entire width of the film.

Figure 42.16 is a print of the spectrometer film in the range ~180 Å–300 Å. The limited angular extent of the four lasing transitions can be seen in comparison to the nonlasing transitions that fill the spectrometer slit and show no dependence on angle. A measure of the x-ray laser beam divergence can be obtained by plotting the intensity along the spectral line.

The angular peak of the narrow x-ray laser beam is very near the top edge of the spectrometer film. This offset position is a result of the x-ray laser beam refraction by the plasma density profile. This deflection angle is ~10–15 mrad away from the target surface.

The low divergence of the x-ray laser beam makes the measurement of its total intensity difficult. This is a result of the uncertainty as to what portion of the x-ray beam the spectrometer is detecting in the direction perpendicular to the slit. Significant (20%–30%) variation in output intensity for shots of the same length were noted. We believe this is caused by variations in GIGS alignment and shot-to-shot differences in the GDL laser conditions.

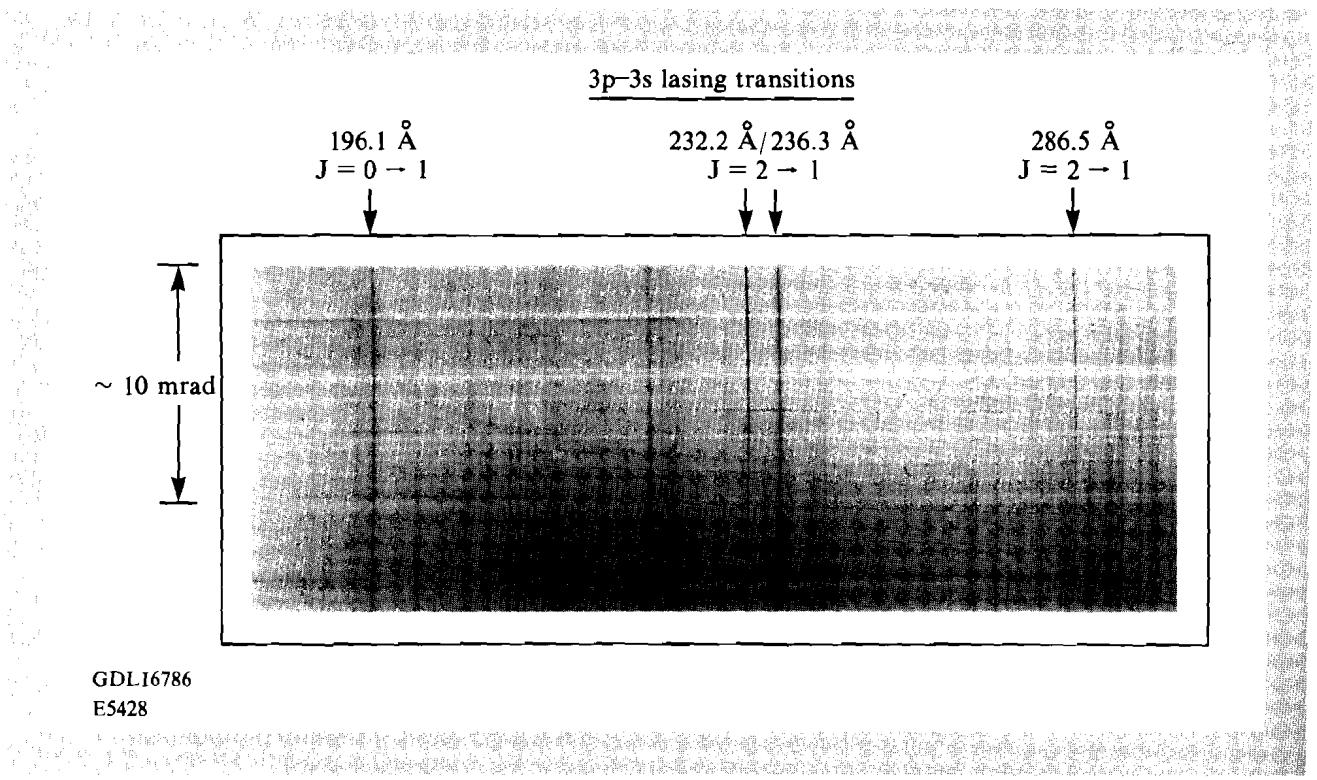

Fig. 42.16
A print of the spectrometer film in the region 180 Å–300 Å. The variation of intensity along the lasing lines (vertical in photo) represents the angular distribution of the x-ray laser output. Note that the nonlasing lines uniformly fill the width of the spectrometer film.

2. Li-like lasing in aluminum and titanium

For the Li-like Al experiments we used the same 650-ps pulse and line focus as described earlier, but reduced the laser energy to about 25 J to give an intensity of 1.9×10^{12} W/cm^2. The Al targets were constructed out of 125-μm-thick slabs of aluminum and were mounted as shown in the Fig. 42.12 inset.

Figure 42.17 shows the XUV spectrum from a 14-mm-long Al target. Note that the 3*d*–5*f* and 3*d*–4*f* lines of Li-like Al at 105 Å and 154 Å dominate the spectrum, suggesting that these lines have experienced gain. Figure 42.18 shows the intensity (as recorded by GIGS) of the 3*d*–5*f* line of Li-like Al versus the target length. It also shows that, up to ~14 mm, the line intensity increases exponentially with target length, exhibiting a gain of 2.2 cm^{-1}. For targets longer than 14 mm, the output intensity remains approximately constant, up to 22 mm. The 3*d*–4*f* line at 154 Å exhibited a similar rollover in the intensity-versus-length curve above 15 mm and exhibited a gain of 2.0 for lengths less than 14 mm. This is possibly the result of refraction that limits the useful length of the plasma. In such a case, the curvature of rays caused by refraction will allow only a 14-mm length of the plasma to contribute to the gain. For lengths greater than 14 mm, the x rays are refracted out of the plasma column before they can sample additional plasma.

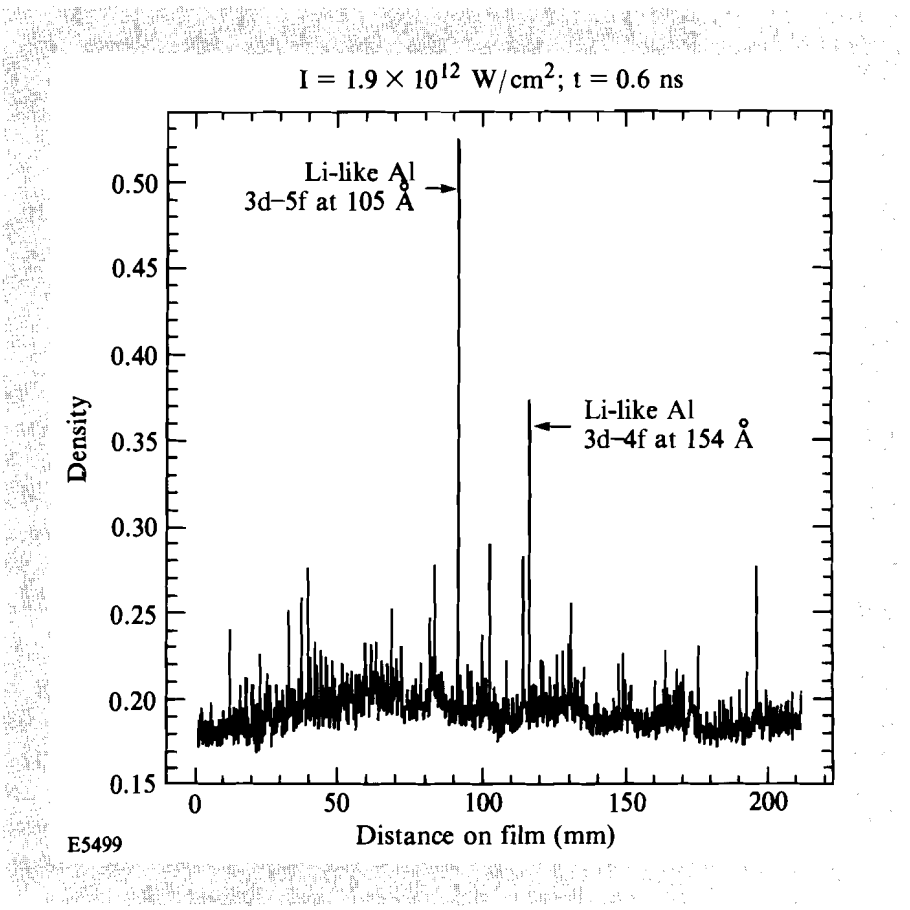

Fig. 42.17
The spectrum from a 14-mm-long Al target at an irradiance of 1.9×10^{12} W/cm^2. Note that the Li-like Al lines at 105 Å and 154 Å dominate the output spectrum for this target.

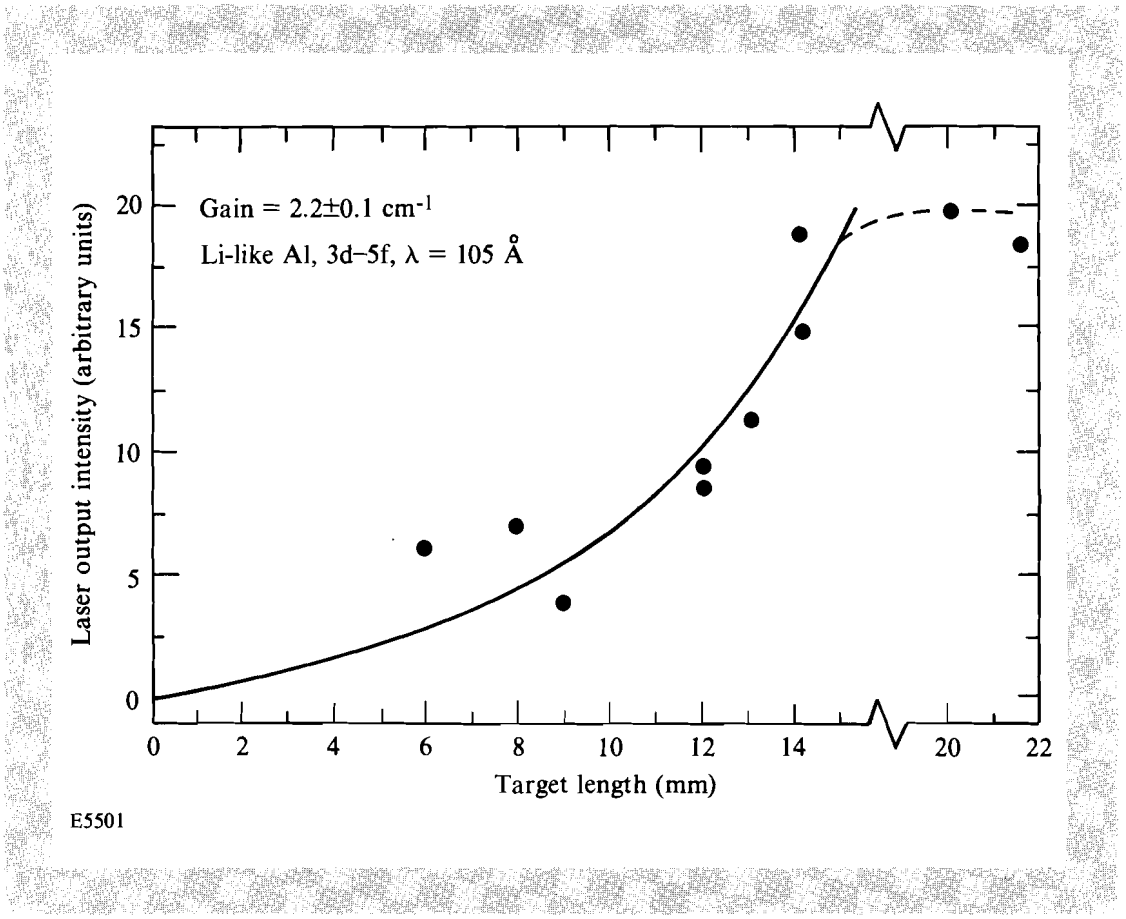

Fig. 42.18
The output intensity of the $3d$–$5f$ Li-like Al line at 105 Å for various target lengths. The points are the experimental data and the solid line is a fit of Eq. (1). Note that the line shows exponential growth for lengths less than 14 mm but is nearly constant for longer lengths (dashed curve).

Similar experiments were performed using Ti targets instead of Al. Again, these targets were fabricated out of 125-μm-thick slabs of Ti supported on the standard mount. To obtain the proper ionization (He-like Ti), the laser energy was increased to 200 J, corresponding to an intensity of 1.25×10^{13} W/cm^2. We observed an exponential growth of the $3d$–$4f$ line of Li-like Ti at 47 Å for increasing length with a gain coefficient of 2.7 cm^{-1}, as shown in Fig. 42.19.

It should be noted that neither the Li-like Al nor the Li-like Ti lasing transitions exhibited the narrow cone of emission observed for the Ne-like Ge lasers (Fig. 42.16). This may result from lasing occuring at a relatively low density where the gradient is also low (as discussed earlier). A broader region of gain will yield a beam that is broader in angle; therefore, the resulting output of the Li-like x-ray lasers may be broad enough to uniformly fill the spectrometer slit.

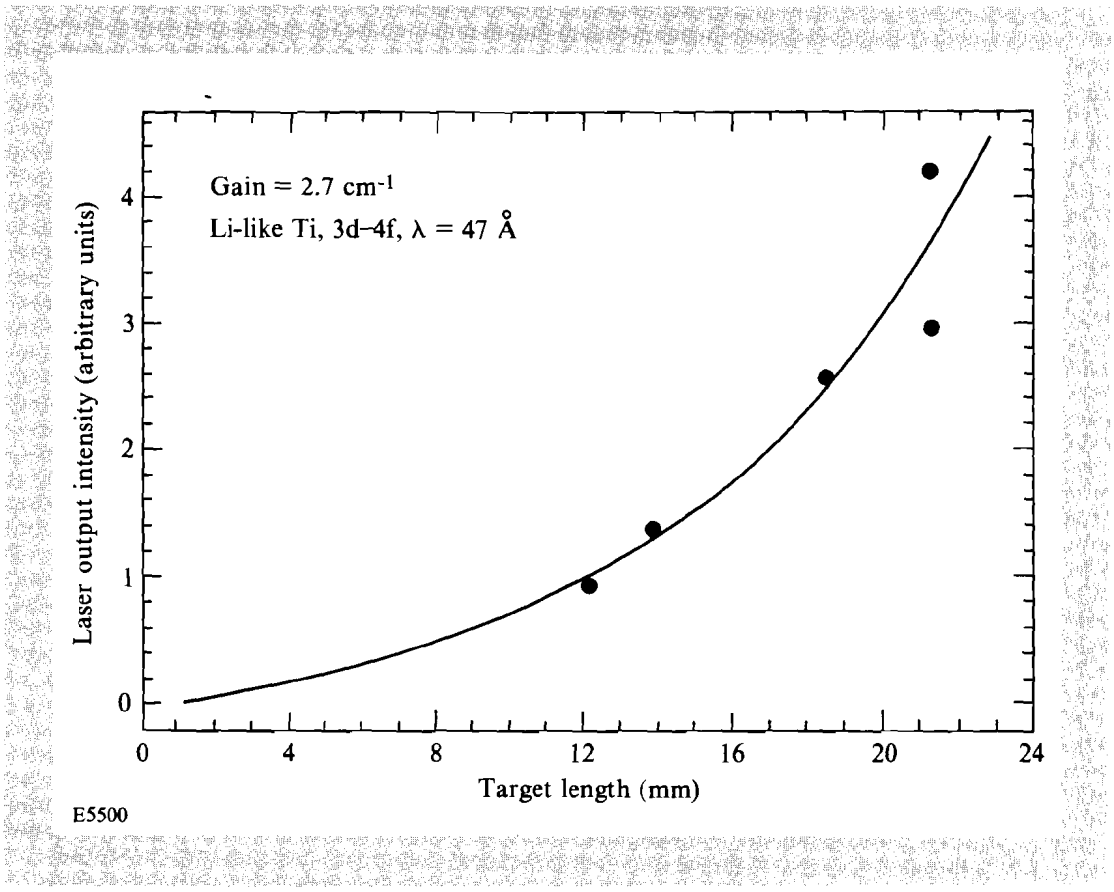

Fig. 42.19
The output intensity of the $3d$–$4f$ Li-like Ti line at 47 Å for various target lengths. The points are the experimental data and the solid line is the fit to Eq. (1).

3. Lasing in Ti at 326.5 Å

At the same irradiation conditions as in the above Ti experiment, an additional line was observed to lase in Ti at 326.5 Å. This transition is shown in Fig. 42.20, which depicts the GIGS spectrum from a 22-mm-long Ti target. The line at 326.5 Å is the most intense line in the Ti spectrum, far brighter than the line at 47 Å in Li-like Ti, which exhibited gain on the same shots. This line has tentatively been identified as a $2p_{1/2}^5 3p_{1/2}(J=0)$ to $2p_{1/2}^5 3s_{1/2}(J=1)$ transition in Ne-like Ti by extrapolating the wavelength values of this transition in various elements.[7] The other Ne-like lines, which have been observed to lase in other elements (J = 2–1, J = 0–1, etc.), lie beyond the current wavelength range of our spectrometer. Figure 42.21 shows the spectrum of a similar shot in the region 10 Å–40 Å in which the $n = 3$ to 2 lines of Ne-like and F-like Ti are labeled. A group of lines from higher ionization states is also indicated. The presence of both Ne-like and F-like Ti suggests that, at peak intensity, we have ionized the Ti past the Ne-like state and that any lasing in the Ne-like state must occur later as the plasma recombines back into Ne-like. It is still unclear what the pumping mechanism is for the inversion. Besides collisional excitation, it has been suggested that Ne-like lasers can be also pumped by recombination from the F-like ions.[2] There have also been line coincidences identified by Nilsen[10] that could contribute to the inversion by photo pumping.

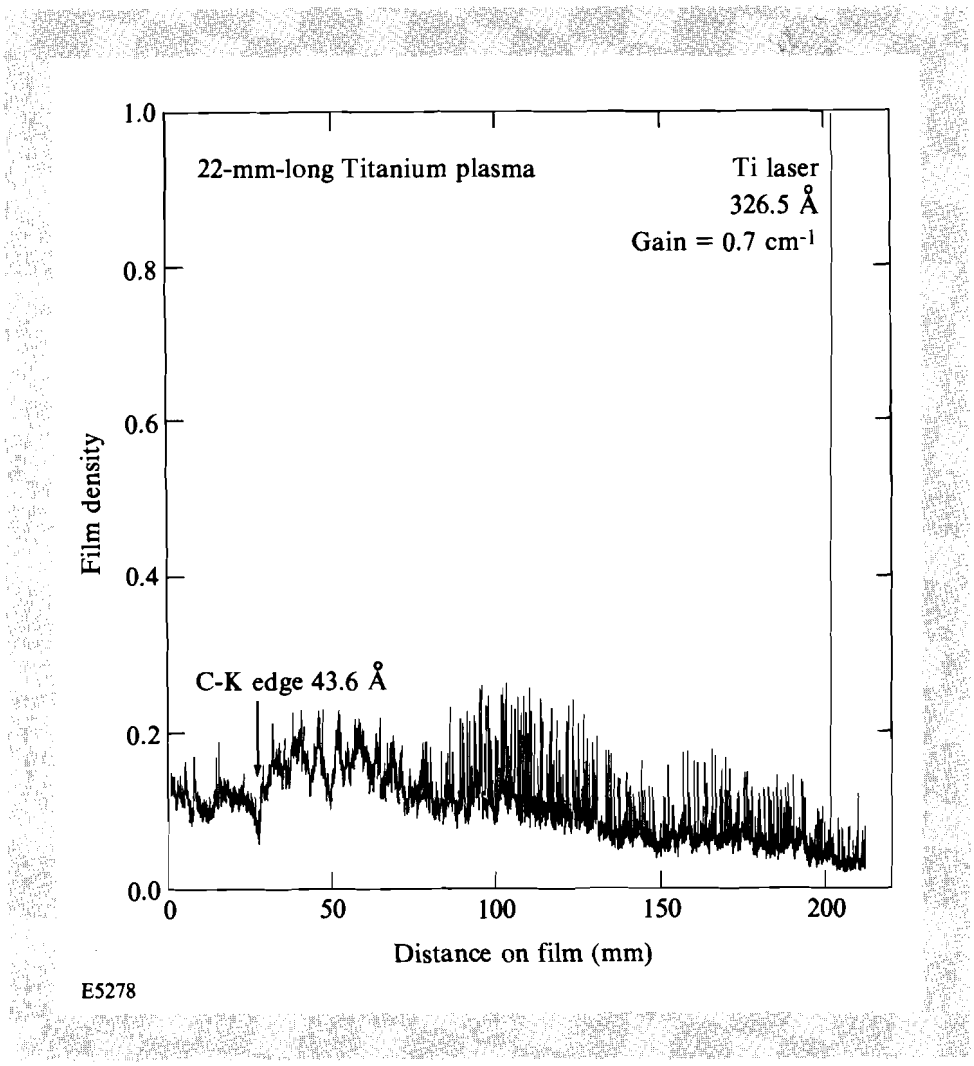

Fig. 42.20
The spectrum from a 22-mm-long Ti target showing the lasing line at 326.5 Å. This line has been tentatively identified as a J = 0–1, $3p$–$3s$ transition in Ne-like Ti. The J = 2–1 lines that lase in Ne-like ions are beyond the range of this spectrometer.

Figure 42.22, a print of the spectrometer film in the range 300 Å–340 Å, shows the limited transverse extent of the lasing line at 326.5 Å. A comparison of the angular intensity distribution of one of the Ne-like Ge lasing transitions (236 Å) and the Ti transition (326 Å) is shown in Fig. 42.22(a). The Ti laser is about half as divergent as the Ge laser. This difference in divergence may be related to the region where the conditions for lasing are optimal in each case. The Ti laser, having a lower atomic number, will have an optimal density for lasing lower than that of Ge. Moreover, if the Ti laser is driven by other excitation mechanisms, the time at which the two x-ray lasers peak will also be different. Further analysis of the output characteristics of these lasers should reveal the basic manner in which they operate.

The low divergence of the Ti laser allows us to determine the gain in the plasma by comparing the radiation intensity along the axis of the x-ray laser to the emission slightly off axis. The ratio of the intensity I of the ASE (on axis) to the intensity I_0 of the spontaneous emission (off axis) as a function of the gain length $(g\ell)$of the laser is given by

$$I / I_o = [\exp(g\ell) - 1] / (g\ell). \quad (2)$$

From this relation we determine the gain coefficient of the 326.5-Å Ti laser to be 2.7 cm^{-1} for a length of 22 mm.

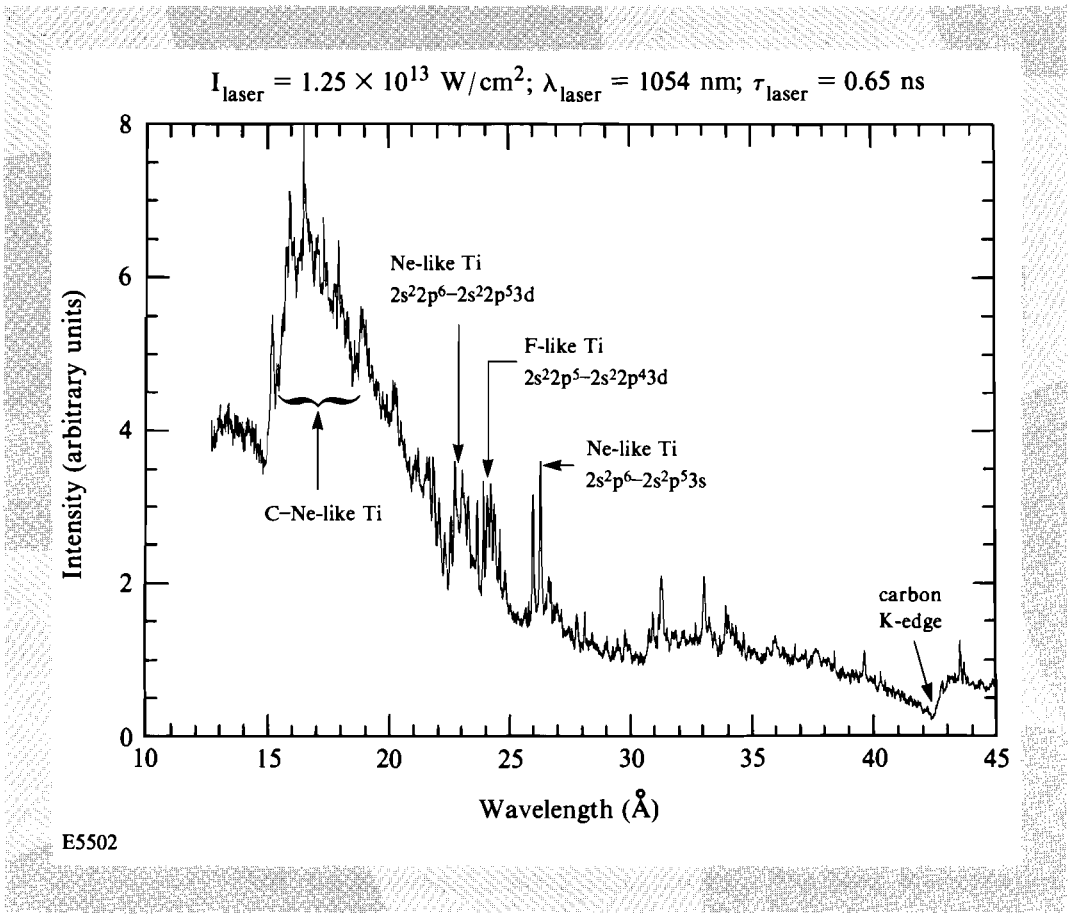

Fig. 42.21
The spectrum from a 22-mm-long Ti target. This spectral region (10 Å–40 Å) contains the $n = 3$ to $n = 2$ lines of Ne-like and F-like Ti. The presence of Ne-like emission supports the claim that the lasing line at 326.5 Å is from Ne-like Ti.

Summary

We have demonstrated several types of lasing using slab targets. We observed gains in the range of 1.0 to 2.5 cm^{-1} in the various $3s$–$3p$ Ne-like Ge transitions previously observed in both exploding-foil targets and slab target geometries. These results were obtained using the lowest optical laser energies reported to date. Our results include a measurement of the angular divergence of the x-ray laser beam in one dimension.

We have also observed gain on the $3d$–$5f$ and $3d$–$4f$ transitions in Li-like Al at 105 Å ($g = 2.2$ cm^{-1}) and at 154 Å ($g = 2.0$), respectively. These transitions have previously been observed at lower irradiances with longer

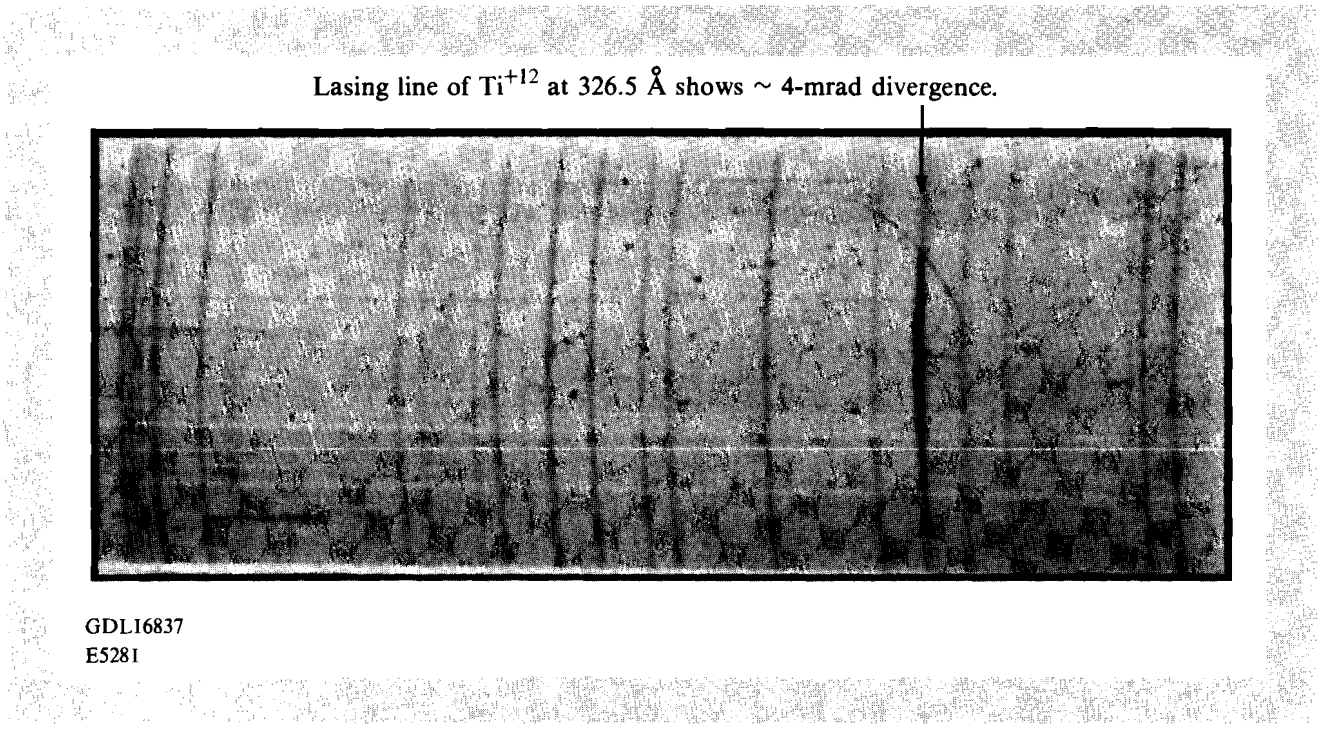

Fig. 42.22
A print of the spectrometer film in the region of the Ti lasing transition at 326.5 Å. The narrow angular extent of the x-ray laser output can be readily seen (see also Fig. 42.16). Both the ASE (on axis) and the unamplified spontaneous emission can be measured from this spectrum.

pulse widths. Our results extend the range of laser conditions for which these transitions have been observed to lase. We also extended this scheme to a relatively short wavelength, 47 Å, by demonstrating a gain of 2.7 cm^{-1} on the $3d$–$4f$ Li-like transition in Ti.

The Li-like lasing transitions (in Al and Ti) appear to behave differently than Ne-like lasers in that no angular distribution peak could be discerned in the output intensity. As the gain medium in an x-ray laser increases, the output beam is dominated by the few rays that experience the most gain. Typically these rays are limited in direction and cause the output beam to get narrower as the medium gets longer. The lack of measured directionality may result from the recombinationally pumped lasers experiencing gain in an extended region of the plasma where more than one path exists through which rays can experience gain. If these multiple paths contain equivalent gain, a wider output beam would be produced. The fact that the output of the Li-like Al emission does not continue to grow exponentially with lengths greater than ~14 mm also suggests that no localized collection of rays has begun to dominate the output.

Originally it was thought that a slab target could not produce gain because steep density gradients would refract the x rays out of the plasma before significant path length is achieved. Therefore, it is important to understand

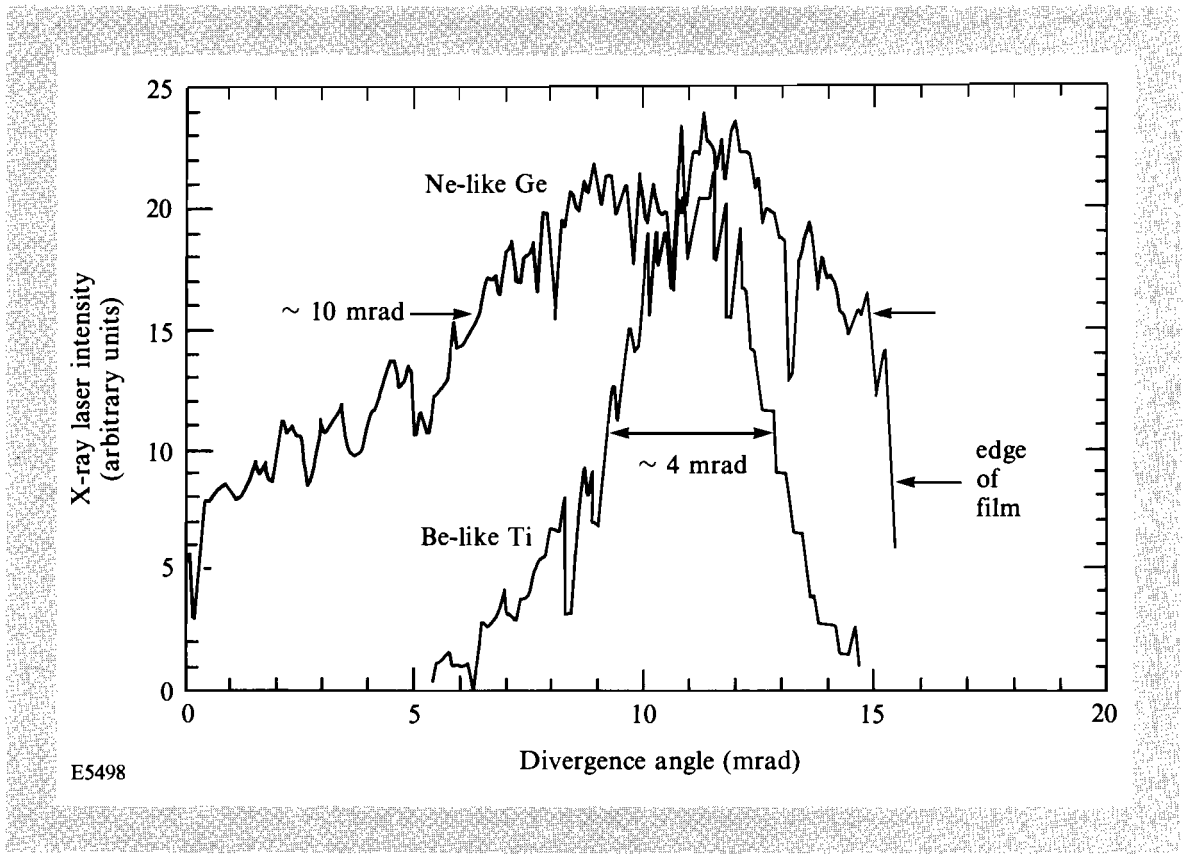

Fig. 42.22(a)
A comparison of the angular intensity distributions of the Ne-like Ge laser (236 Å) and the Ti laser (326 Å).

how these slab-target x-ray lasers behave. We have developed both analytical[11] and numerical[12] models that treat the refraction of x-ray laser beams in various types of targets. These models should help us explain where the x rays experience most gain and how they propagate through the target. The numerical code solves the three-dimensional ray-trajectory equation through the two-dimensional density profiles generated by a separate hydrocode. The local gain (as a function of temperature and density) has been calculated using a detailed atomic physics code.[13] By following various rays through the plasma, applying the calculated gain, and summing their contributions we will be able to compare the predictions to the experiments and comment on the relative importance of refraction in various target types.

Finally, we have observed a gain of 2.7 cm^{-1} on a transition at 326.5 Å in Ti. We will attempt to identify this transition by extending the range of the GIGS to include the other predicted Ne-like lasing transitions. If this transition is indeed Ne-like, then there are a number of additional questions to be resolved. For example, the gain is higher than predicted by the scaling of gain in Ne-like ions with atomic number as demonstrated by Lee

et al.,[3] from which an extrapolation to Ti results in a gain of nearly zero. This suggests that there may be pumping mechanisms other than collisions that contribute to gain in the Ti x-ray laser.

ACKNOWLEDGMENT

This work was supported by the Naval Research Laboratory under contract N00014-86-C-2281 and by the Laser Fusion Feasibility Project at the Laboratory for Laser Energetics, which has the following sponsors: Empire State Electric Energy Research Corporation, New York State Energy Research and Development Authority, Ontario Hydro, and the University of Rochester.

REFERENCES

1. D. L. Matthews *et al.*, *Phys. Rev. Lett.* **54**, 110 (1985).
2. C. J. Keane *et al.*, *J. Phys. B.* **22**, 3343 (1989); R. A. London *et al.*, *ibid.* **22**, 3363 (1989).
3. T. N. Lee, E. A. Mclean, and R. C. Elton, *Phys. Rev. Lett.* **59**, 1185 (1987).
4. D. Kim *et al.*, *J. Opt. Soc. Am. B* **6**, 115 (1989).
5. P. Jaegle *et al.*, *J. Opt. Soc. Am. B* **4**, 563 (1987); G. J. Pert, *Plasma Phys. & Controlled Fusion* **27**, 1427 (1985); S. Suckewer *et al.*, *Phys. Rev. Lett.* **55**, 1753 (1985); J. F. Seely, C. M. Brown, U. Feldman, M. Richardson, B. Yaakobi, and W. E. Behring, *Opt. Commun.* **54**, 289 (1985); P. R. Herman *et al.*, *IEEE Trans. Plasma Sci.* **16**, 520 (1988).
6. T. Hara *et al.*, *Proc. Japan. Acad.* **65**, 60 (1989).
7. J. H. Scofield (private communication).
8. W. Seka, J. M. Soures, S. D. Jacobs, L. D. Lund, and R. S. Craxton, *IEEE J. Quantum Electron.* **QE–17**, 1689 (1981).
9. B. L. Henke *et al.*, *J. Opt. Soc. Am. B* **1**, 818 (1984); B. L. Henke *et al.*, *ibid.* **1**, 828 (1984).
10. J. Nilsen (private communication).
11. B. Boswell, D. Shvarts, T. Boehly, and B. Yaakobi, to be published in *Phys. Fluids B*.
12. R. S. Craxton, 10th Annual Anomalous Absorption Conference, Durango, CO, 19–23 June 1989; also R. S. Craxton, LLE Review **38**, 88 (1989).
13. M. Klapisch, *Comput. Phys. Commun.* **2**, 239 (1971).

2.B Electro-Optic Imaging of Surface Electric Fields in High-Power Photoconductive Switches

Semiconductor photoconductive switches have become increasingly useful for pulsed-power applications where high voltages must be switched on a short time scale. They are used in a variety of devices, including microwave generation, Pockel's cell drivers, and an innovative accelerator design.[1,2] There has been considerable interest in the design and operation of photoconductive switches, and various semiconductors have been investigated for use as switches, the most popular materials being silicon and GaAs. GaAs is particularly suited for high-voltage switches as its high resistivity ($\rho > 10^7$ cm) makes it less susceptible to thermal runaway than other, less-resistive materials. This is very important, as the electric field between electrodes on a semiconductor photoconductive switch can be significant, with typical field strengths between 1 and 50 kV/cm. At these field strengths, switches will preferentially break down along the surface between electrodes. Surface breakdown is the primary failure mode for photoconductive switches and places a limit on their operation. The problem is compounded by the need to shorten the electrode gap to increase switching speed, thus increasing the electric field across the switch for a given bias voltage. Engineering considerations, such as the need to improve switch reliability, and the desire to explain certain physical phenomena associated with high-voltage switching have motivated the investigation of the dynamics of photoconductivity. Despite their relevance to switch engineering, the mechanisms of surface breakdown and photoconductivity are not well understood.

To better understand the physics of photoconductivity it is necessary to monitor a photoconductive switch during the switching process. Conventional analog or sampling oscilloscopes do not have the bandwidth to temporally resolve switch rise times of the order of a picosecond. However, greatly improved temporal resolution can be provided by sampling the switched output electro-optically. In this technique the birefringence of an electro-optic crystal, placed in the vicinity of an electronic circuit, is modified by stray electric fields surrounding the circuit. This electric field can then be measured by probing the electro-optic crystal with a fast, polarized optical pulse and monitoring the change in polarization. The duration of the optical pulse determines the bandwidth of the system, with an effective limit of about 1 THz due to crystal absorption. This technique has been used to measure the picosecond and subpicosecond output of electronic devices.[3,4]

Conventional electro-optic sampling techniques involve coupling the switched voltage output of a photoconductive switch to a strip line and measuring the voltage on the strip line electro-optically, remote from the switch. Such a measurement of the output waveform yields information

about the temporal evolution of the voltage at the output electrode of the switch but no information about the evolution of the electric field within the electrode gap itself. The electric field in the contact gap must be changing rapidly in both time and space as the gap is driven conductively by the optical-excitation pulse. By combining electro-optic sampling, short-pulse lasers, and imaging technology, an ultrafast, two-dimensional electro-optic imaging system has been developed that can monitor rapid variations of the electric field over an extended region in detail. This system can produce maps of the surface electric field between contacts on photoconductive switches that can be used to determine the electric-field configuration for different contact shapes, separation, and preparation.

This article details the development of the electro-optic imaging system and its application to the study of photoconductive switching, particularly in GaAs. The surface field between the electrodes on a GaAs photoconductive switch was monitored during switch operation; the collapse of the electric field was observed for various bias voltages and excitation conditions.

System

The electro-optic imaging system represents the latest development in a series of optical probes utilizing the electro-optic effect to characterize surface electric fields between electrodes on semiconductor devices.[5] Earlier work involved the use of single-point or one-dimensional, time-averaged, electro-optic sampling. Extension of this work has produced the current two-dimensional, time-resolved, electro-optic imaging system, which can obtain full surface field maps in real time with picosecond temporal resolution.[6,7] This electro-optic probe is particularly suited for the study of high-field devices because the optical probe does not require any electrical connection to the device under test. Optical detection of the electric field is carried out using the electro-optic, or Pockel's, effect in which the birefringence of certain crystals can be altered by an electric field applied across the crystal. If a beam of polarized light traverses the crystal, the electrically induced birefringence will rotate the probe beam's polarization. This rotation can be detected and used to measure the electric field present in the crystal. The electric field in the crystal is not, necessarily, spatially uniform. If the probe beam only illuminates a small portion of the crystal, the electric field in that region only will be measured. A full measurement of the electric field would then require translation of the sampling point across the crystal. However, if the entire crystal is illuminated by the probe beam, the electric field at every point in the crystal will be interrogated. The probe beam will then be imprinted with an optical analog of the spatial electric-field distribution in the crystal. This is the essential operating principle of the two-dimensional electro-optic probe. Temporal resolution is obtained by using a pulsed laser as the probe beam. In effect, a snapshot of the instantaneous electric field is taken. To produce the desired effect, the crystal axis, optical polarization, and electric field must all be properly aligned.

Details of the probe beam, electrodes, and crystal geometry for the surface-field probe are shown in Figs. 42.23 and 42.24 for two different types

of photoconductive switches. Figure 42.23 shows the surface-field probe set up to measure the field of a photoconductive switch of a surface device type, i.e., the metallic contacts are in the same plane on the surface of a semiconductor substrate. Figure 42.24 shows the probe set up to measure the field of a bulk photoconductive switch, which has contacts on opposite faces of a rectangular slab of semiconductor. For either type of switch, the probe operation is the same; only the IR pump geometry is different. When a bias voltage is applied to the metallic contacts, an electric field is established between them with a fringing field extending above the surface of the semiconductor. The electro-optic crystal is placed directly on top of the switch, covering the contact gap completely. A dielectric mirror is bonded to the underside of the crystal. This reflection-coated side is in contact with

Fig. 42.23
Detail of electro-optic probe set up to measure electric field above photoconductive switch of surface device type.

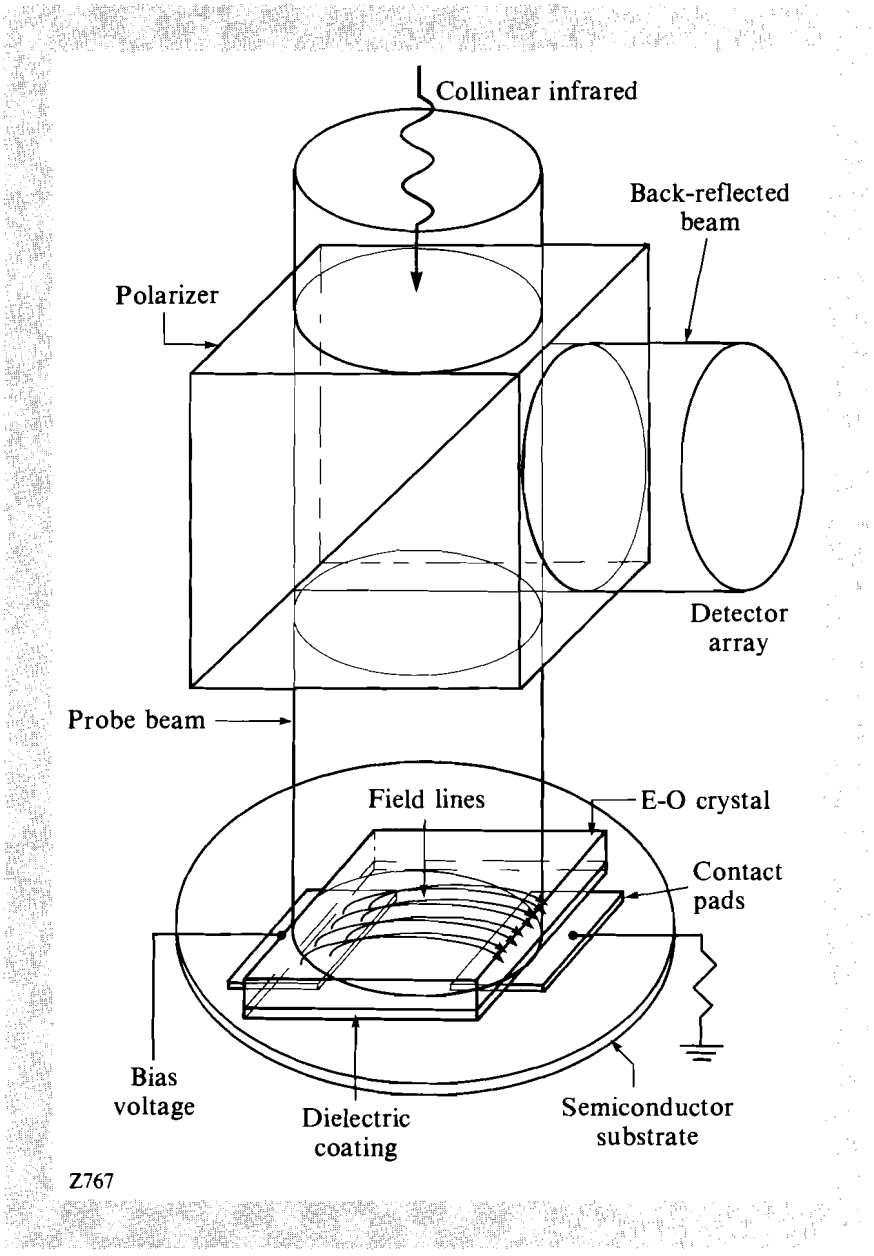

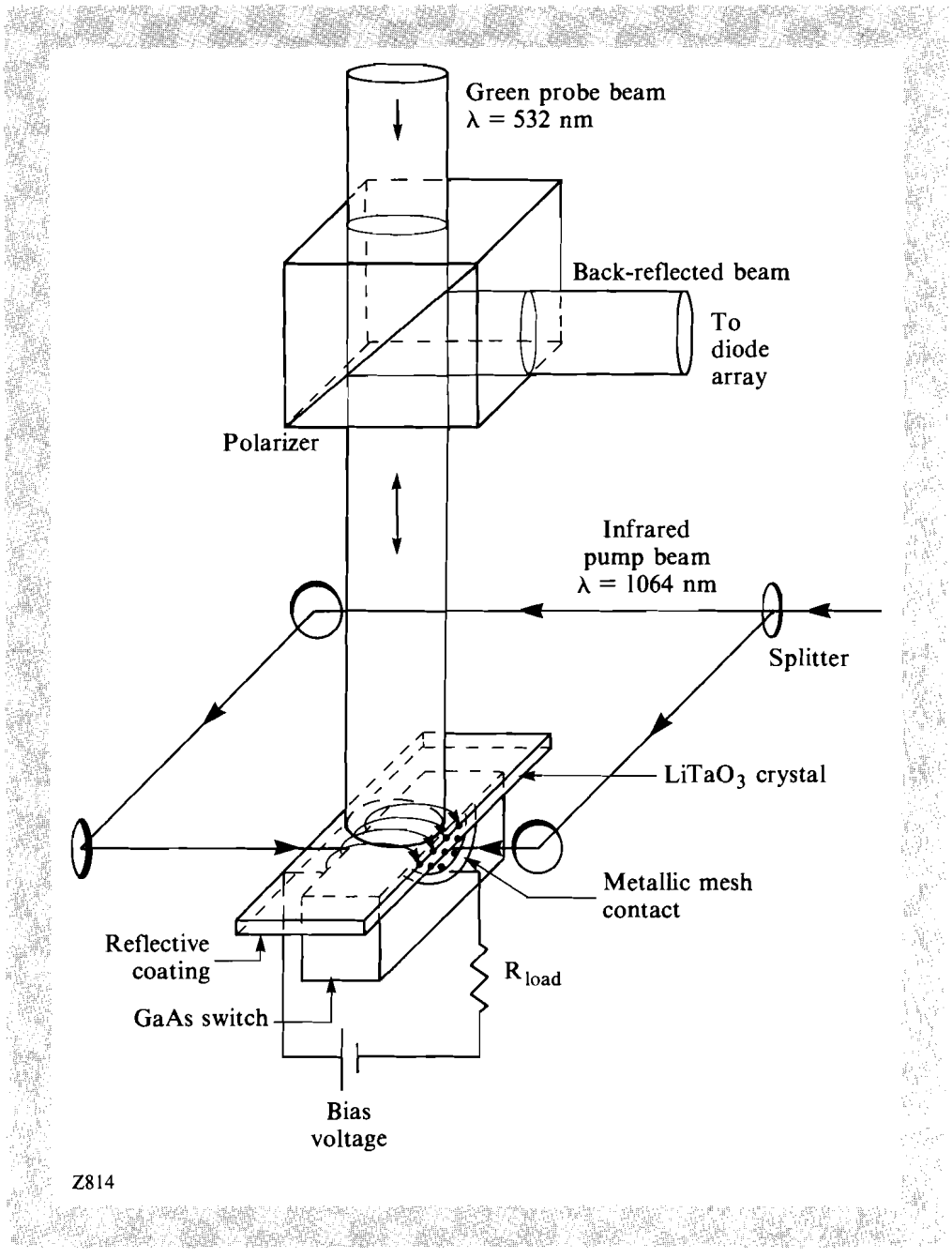

Fig. 42.24
Detail of electro-optic probe set up to measure electric field of GaAs bulk photoconductive switch.

the semiconductor. Therefore, the crystal is immersed in the fringing electric field of the contacts and its birefringence is altered by this surface field. The optical probe, visible green light with $\lambda = 532$ nm, is polarized and directed onto the crystal and test switch. The probe-beam diameter is greater than the contact gap so that the entire contact gap is illuminated. The beam traverses

the crystal and is reflected back onto itself by the dielectric mirror on the semiconductor side of the crystal. The back-reflected beam, whose intensity is an optical analog of the electrically induced birefringence in the crystal, is imaged onto a two-dimensional diode array that records the intensity profile of the beam.

Each pixel in the array image has a corresponding point in the crystal. As the optical probe makes a double pass through the polarizer, the crystal can be considered to be between two crossed polarizers. The intensity at any given point in the cross section of the back-reflected beam will depend on the sine squared of the polarization rotation experienced by that particular beam element as it traversed the crystal. The transmission to a detector element (i, j) can be written as

$$T_{i,j}(V) = I_{i,j}(V) / I'_{i,j} = \sin^2\left[(\alpha_{i,j}E_{i,j} + \beta_{i,j})\right], \tag{1}$$

where $I_{i,j}(V)$ is the light intensity measured at camera pixel (i,j) when a voltage V is applied to the electrodes; $I'_{i,j}$ is the intensity that appears at the camera if 100% of the light is imaged onto the camera without bias voltage applied; $E_{i,j}$ is the magnitude of the local electric field; $\alpha_{i,j}$ is a constant for a given point (i, j) that relates the electro-optic coefficient[8] to the local electric field and whose value depends on material parameters, optical path length in the crystal, electrode geometry, and frequency of applied optical field; and $\beta_{i,j}$ is a constant optical rotation due to static birefringence in the crystal and quarter-wave plate. To obtain the best response to the applied electric field, a quarter-wave plate is placed between the polarizer and crystal to optically bias the probe beam on the sine-squared transmission curve given by Eq. (1). By comparing the intensity at the camera with and without voltage applied, the rotation caused by the electric field can be determined.

The electro-optic crystal used was 0.5-mm-thick y-cut $LiTaO_3$, cut to completely cover the contact gap of the switch being studied. The top surface of the $LiTaO_3$ was antireflection coated to prevent internal reflection and improve transmission through the crystal. The bottom surface was coated with the aforementioned dielectric mirror to have a reflectivity of 99.3% at 532 nm. The $LiTaO_3$ optic axis (z axis) was perpendicular to the contact edges and generally parallel to the applied electric field. In this geometry, the crystal is sensitive primarily to the electric-field component parallel to the $LiTaO_3$ optic axis. The voltage pulse switched by the green probe light was measured using an oscilloscope attached to the load side of the switch and was found to be negligible (10^{-6} times the applied bias voltage).

The complete probe system is shown in Fig. 42.25. The entire computer-controlled system consists of the test switch and crystal shown in detail in Figs. 42.23 and 42.24, the detector array, a high-voltage pulser, and an optical delay translation stage. The laser source is a Nd:YAG regenerative amplifier seeded by a Nd:YAG mode-locked oscillator. The wavelength is 1064 nm and the pulse width is about 100 ps to 200 ps. The mode-locked

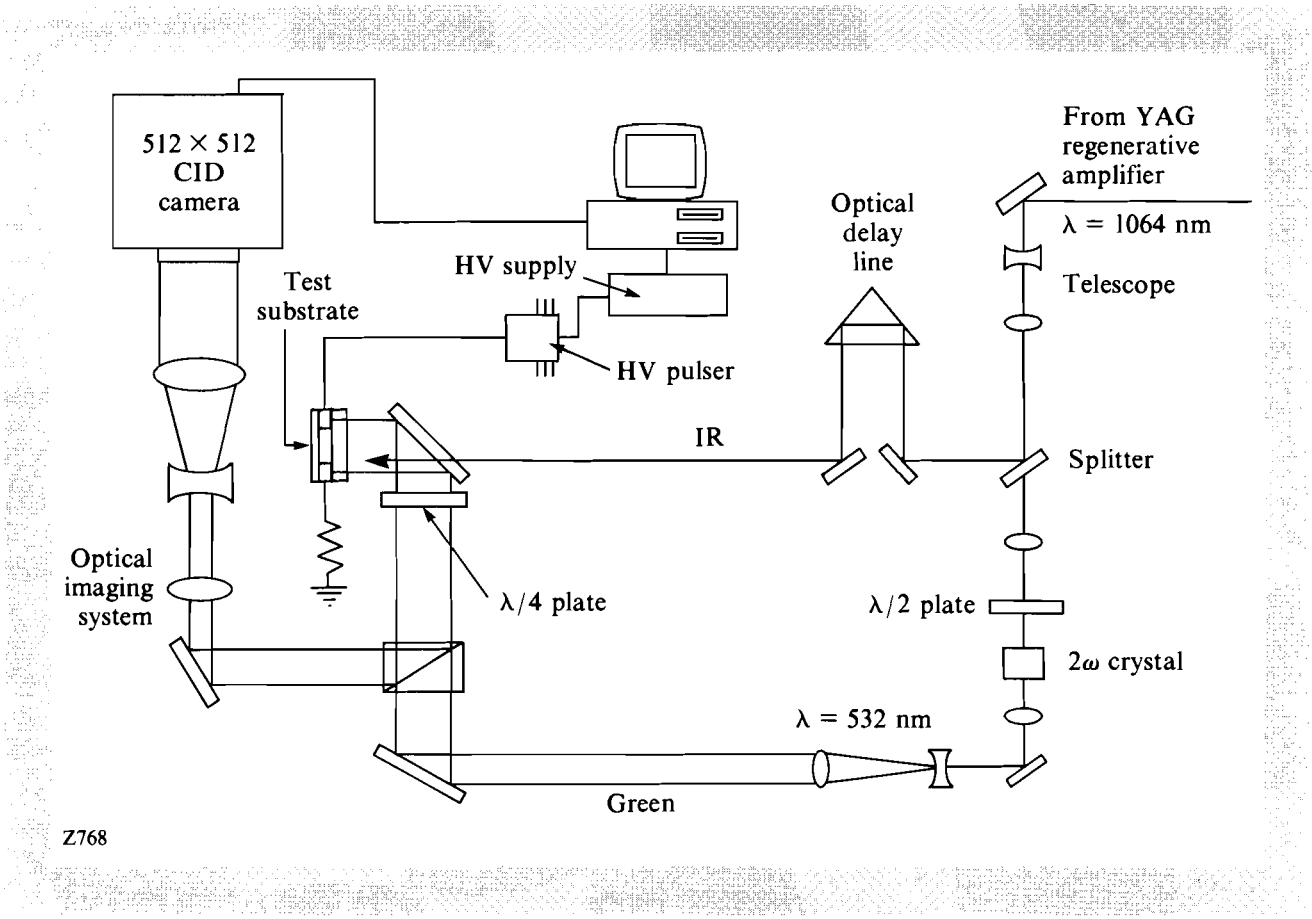

Fig. 42.25
The complete electro-optic imaging system.

pulses are amplified to approximately 300 μJ and switched out of the laser with a double Pockel's cell arrangement to yield pulses that have a prepulse to main pulse contrast ratio of 4000:1.[9] There are always small prepulses present in the amplifier output at the oscillator repetition rate of 100 MHz. The amplifier pulse repetition rate is variable up to 1 kHz. The infrared beam from the amplifier is first upcollimated and then split, 90% for switching use and 10% for second-harmonic generation. Green ($\lambda = 532$ nm) laser pulses are generated in a KTP crystal. This green beam is upcollimated and serves as the probe beam. The 1.25-cm, green-beam diameter is sufficient to completely illuminate all the electrode gaps that were studied. The back-reflected probe-beam pulses are imaged onto a 512 × 512-element GE CID camera, which is interfaced to a personal computer through a PCVISIONplus video frame grabber supplying an 8-bit digital image of the modulated probe beam. The camera response was measured to be linear with applied light intensity over the range used in this experiment. As the green probe consists of ~140-ps pulses, the switch surface field is sampled only during a short window in time. If the infrared excitation pulse illuminates the switch during this window, the switch field will be sampled during the photoconductive collapse. For surface switches, as in Fig. 42.24, this is

accomplished by directing an infrared pulse onto the switch gap collinear with the green probe pulse. For the bulk switches, the infrared illuminates the switch directly through the metallic mesh contacts. By sweeping the 140-ps sampling window in time, the switch surface field can be monitored as the switch photoconductivity evolves in time. The system's operation can be viewed as 512×512 separate, parallel, pump-probe experiments, each probing a different spatial region in the electrode gap. The sampling window is moved in time by changing the length of an optical delay line in the infrared beamline. This delay line consists of a retro-reflector on an Aerotech computer-controlled translation stage. As the pump and probe are derived from the same laser pulse and timed optically, there is no jitter.

For the probe to operate in real time, i.e, without averaging, data must be collected with a single laser pulse. As the system operates in the high-field regime, the electric field applied to the electro-optic crystal causes the optical polarization vector of the probe pulse to change by a significant fraction of $\pi/2(>2\%)$. At these fields, the change in transmission to the camera is large with respect to the shot-to-shot noise in the laser pulse. Thus, the electro-optic images can be acquired without averaging. This is essential to image random events such as surface breakdown. To ensure that the camera sees only one laser pulse, the camera and laser are synchronized to the same electronic oscillator, with a pulse from the camera triggering the firing of the laser. Data is taken at a 30-Hz repetition rate, limited by the camera. The intensity of every laser pulse is measured with a fast diode. Any pulse not within 10% of a reference value is rejected and the measurement is repeated.

The field data must be extracted from the raw camera image. The values of $\alpha_{i,j}$ and $\beta_{i,j}$ for each point (i,j) must be determined so that given the transmission $T_{i,j}$, the field $E_{i,j}$ can be determined. The crystal is not illuminated uniformly, as the probe beam has a Gaussian spatial profile. Therefore, the raw image must be normalized with respect to the beam profile, so that the transmissivity and not the transmitted intensity is used.

Each image acquired by the camera is normalized to a stored reference image. This reference image is the average of four frames taken with the quarter-wave plate set for maximum transmission and with a dielectric mirror in place of the $LiTaO_3$ crystal. The light intensity is adjusted so that the most intense pixel is just within the 8-bit camera resolution; i.e., no points in the detector field are saturated. This reference image then contains $I'_{i,j}$ for each point (i, j), as in Eq. (1). Images normalized with respect to this reference are scaled to the maximum signal and represent $I_{i,j}(V)/I'_{i,j}$.

The values of $\alpha_{i,j}$ and $\beta_{i,j}$ are obtained by calibrating the response of the probe to an applied electric field. A quasi-dc, i.e, long compared to the light pulse, bias voltage is applied to the contacts by a computer-controlled high-voltage pulser. The bias voltage is varied from 0 kV–9.5 kV in 500-V increments. An image is taken at each voltage and reduced

to a 32×32 array by averaging over pixels. This array size reduction is done so that image acquisition, processing, and display can be done with a PC rather than a workstation and in real time, i.e., without any post-processing. This allows for rapid scanning of camera images. The transmission curve [Eq. (1)] for each of the 1024 elements of the reduced image is determined experimentally by this procedure. $\alpha_{i,j}$ and $\beta_{i,j}$ are then obtained by performing a least-squares fit of the experimental transmission curve to Eq. (1) for each element in the reduced image. Figure 42.26 shows this dc calibration for one element of the reduced image. The biasing is chosen such that all points lie within one-half cycle of the transmission curve. Due to the sinusoidal nature of Eq. (1), it is sometimes necessary to reduce sensitivity to see large effects.

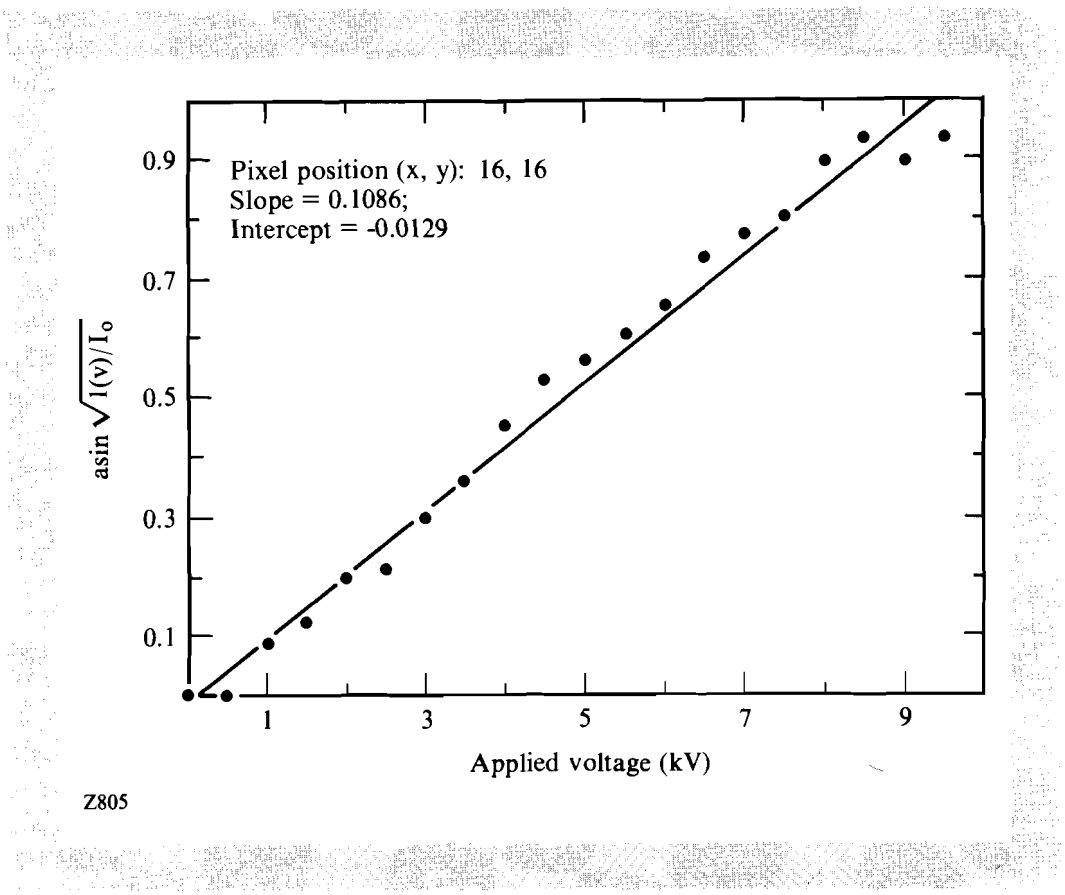

Fig. 42.26
Results of dc calibration of electro-optic imaging system showing least-squares fit of the experimental transmission curve to Eq. (1) for one image pixel.

After correcting for the probe-beam spatial profile and calibrating the crystal response, the surface electric field information can be decoded from the raw images. To measure the field, a frame is first acquired with high-voltage bias on and then with the bias off. Each frame is digitized with 8-bit resolution, normalized to the probe-beam profile and scaled, and then reduced to a 32×32 array. The images are scaled by dividing the raw image by the reference image, pixel by pixel. The division is performed using a look-up table for speed of execution and scale control. These two reduced

arrays, i.e., each element within each array, represent two different points, $T_{i,j}$, on the transmission curve [Eq. (1)]. The zero-bias image is used to remove the contribution of the static birefringence. The arrays are used as inputs to a function that, using the dc calibration described earlier, transforms the transmission $T_{i,j}$ to field $E_{i,j}$ by inverting Eq. (1). The field $E_{i,j}$ is given in units of "equivalent electrode voltage" (EEV), which means that the point (i,j) is responding to the applied electric field as if a voltage $E_{i,j}$ were applied to the electrodes. The resulting field map of the electric field has an 8-bit range and can be displayed as a false-color image on a monitor or the digital image can be manipulated to produce field contour plots, axonometric plots, or field cross sections of a particular line across the switch. The optical system is capable of producing images with a spatial resolution of 3 μm per pixel. The electric field can be measured with this type of spatial resolution, but this would require that the above calibration procedure be applied to the entire 512×512 array. This has been done in selected cases but, in general, 32×32 images have been used. The minimum electric-field sensitivity is approximately 200 V/cm and can be adjusted by rotating the quarter-wave plate.

Experiments

Silicon and GaAs photoconductive switches have been studied, the majority of the work involving GaAs. The Si switches are surface devices (see Fig. 42.23), whereas the GaAs switches are bulk devices (see Fig. 42.24). Figures 42.27 and 42.28 show typical raw, unnormalized data obtained with the electro-optic imaging system. Figure 42.27 shows successive lineouts of the surface field over a 3-mm-gap Si switch taken through the center of the switch parallel to the contact edge. The switch gap has been illuminated by the IR pump pulse. Time is relative to the position of the IR optical delay line, where 0 ps indicates the arrival of the pump pulse. The surface electric field begins collapsing at the onset of photoconductive switching and has collapsed completely within 300 ps, consistent with the ~200-ps pulse width of the laser. Figure 42.27 illustrates the ability of the system to monitor the surface field in the switch gap during switch operation and the ability to measure switching parameters like switch rise time directly using the field across the electrode gap and not by measuring the switched output. In this case, the field collapse is spatially uniform, as the gap was driven conductive by uniform IR illumination. Figure 42.28 illustrates the ability of the system to map nonuniform fields above a 3-mm-gap Si switch and to observe carrier migration within the switch gap. The nonuniform fields are the result of nonuniform IR illumination. The center of the switch gap was illuminated with a pinpoint (~40-μm) spot of infrared laser energy. This local illumination photogenerates carriers only in a small region at the gap center. These carriers migrate outward, collapsing the surface field as they drift. One interesting feature of the field on the coplanar silicon switch is that we have not detected the significant field enhancements at the contact edge we would have suspected from the geometry. We believe that this may be because of the conductivity of the silicon substrate.

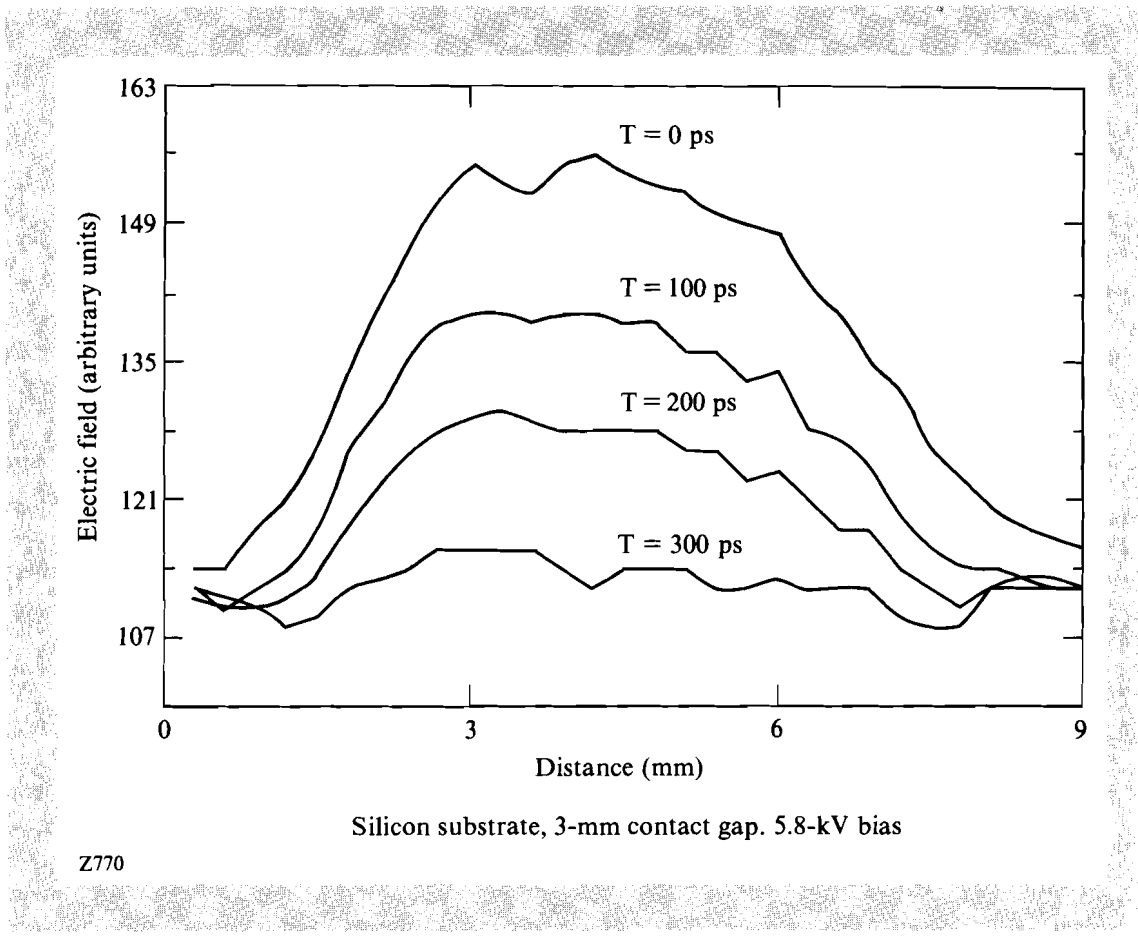

Fig. 42.27
Collapse of electric field above IR-illuminated surface-type Si switch. Lineouts from raw electro-optic images taken through center of switch perpendicular to contact edge for various times. The switch was biased at 5.8 kV across a 3-mm contact gap. Note the spatially uniform collapse of the field.

The primary physical system investigated was the collapse of the electric field in a GaAs bulk photoconductive switch. These switches were fabricated by depositing circular contacts of NiAu:Ge on opposite faces of a 0.6- to 1-cm-thick block of intrinsic GaAs. The GaAs was high-resistivity material ($\rho \sim 10^7$ cm) supplied by MA-COM. The contacts consisted of a solid annulus surrounding a center region that was perforated to allow light to pass through into the bulk of the GaAs. The contact preparation was also varied with the 6-mm-thick switches having an ion implantation under the metallization to make ohmic contacts, the other samples having contacts deposited on bare GaAs. This switch design is of particular interest both for its applicability to coaxial geometry[10] and for its relative immunity to surface breakdown, as a surface arc must travel out to the edge, down the side, and back into the center—a very long physical path. The design is also useful in that this contact geometry allows for uniform fields that facilitate extraction of absolute field values, as opposed to the coplanar geometry that

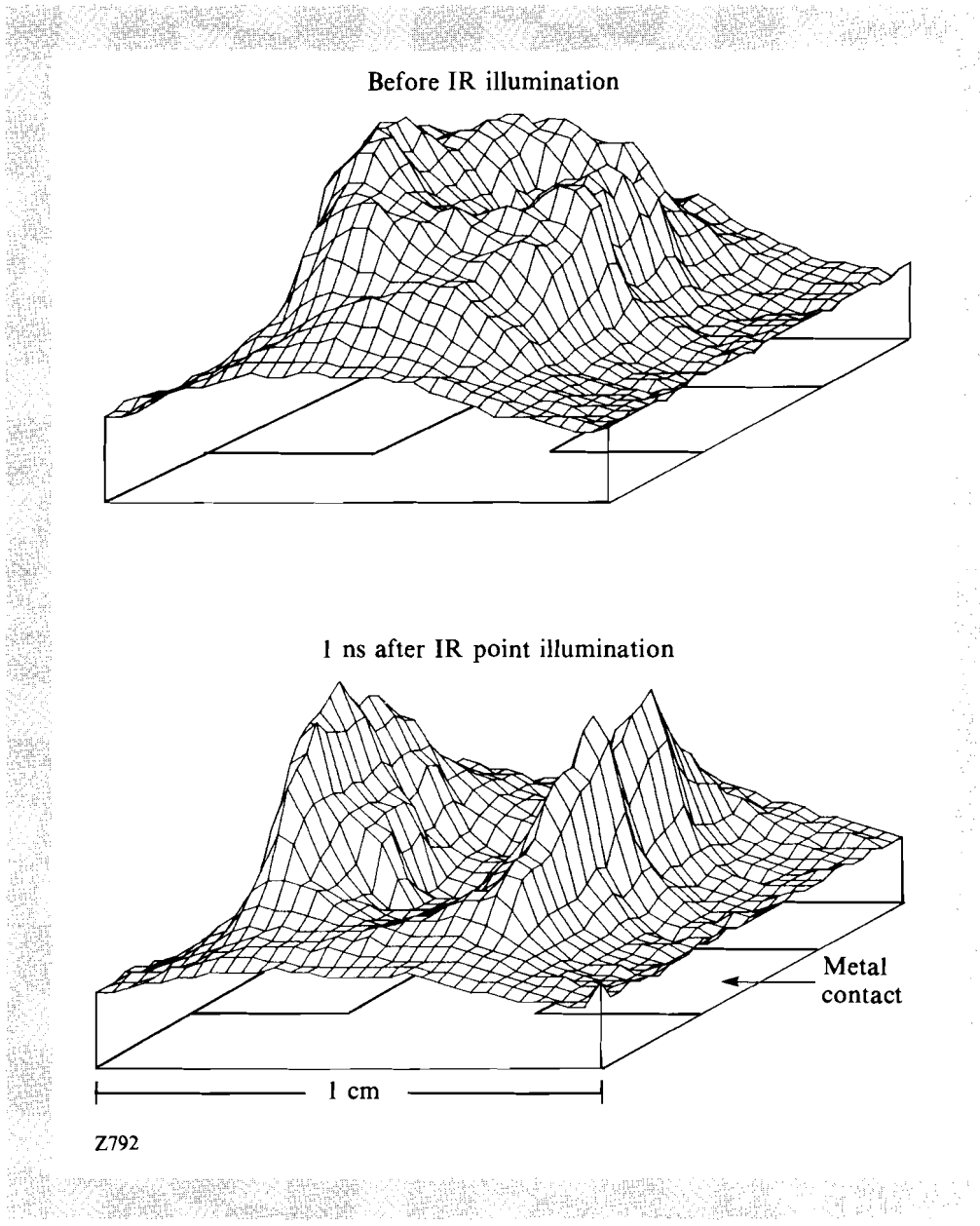

Fig. 42.28
Effect of nonuniform illumination on the electric field above Si surface-type switch. Raw electro-optic images shown before and 1 ns after illumination by 40-mm spot of IR energy at switch center. Switch was biased at 3 kV across 3-mm contact gap. Note local collapse of electric field near switch center.

has a much more complicated field pattern. To access the fields between the contacts, this design has been modified by cutting the GaAs in a plane passing through the center of the contacts. Connection to the external circuit was made by pressure-contacting copper electrodes coated with indium along the outside circumference of the NiAu:Ge electrodes. The Cu electrodes were bored out so that IR light could reach the switch contacts. By

placing a dielectric beam splitter in the IR pump beam, approximately 50% of the IR light could be directed onto each electrode. Either of these beams could be blocked to investigate asymmetries in the response of the photoconductor. The arrival time of the two beams at the switch was adjusted to within 300 ps by monitoring the arrival of the switch pulse at the load with a 1-GHz analog oscilloscope. The dielectric beam splitter was mounted on a kinematic mount so that it could be removed and the full IR laser energy could be applied to one side of the switch. Thus, five illumination schemes were employed, considering that full energy could be applied to either the ground or high-voltage contact.

Figures 42.29–42.32 show data taken for a 6-mm-thick ion-implanted GaAs bulk switch. The images taken were normalized and scaled to EEV. Figure 42.29 shows an axonometric plot of the surface field on a 6-mm GaAs switch illuminated through both contacts 800 ps after initial illumination by a 2-mm-wide pump beam. Outside the region between the contacts, the field falls abruptly to zero because there is no tangential component of the electric field at the surface of a conductor. Noise spikes in that region of the image have been artificially suppressed. The left edge of the image corresponds to the negative high-voltage contact, and the right side to the ground contact.

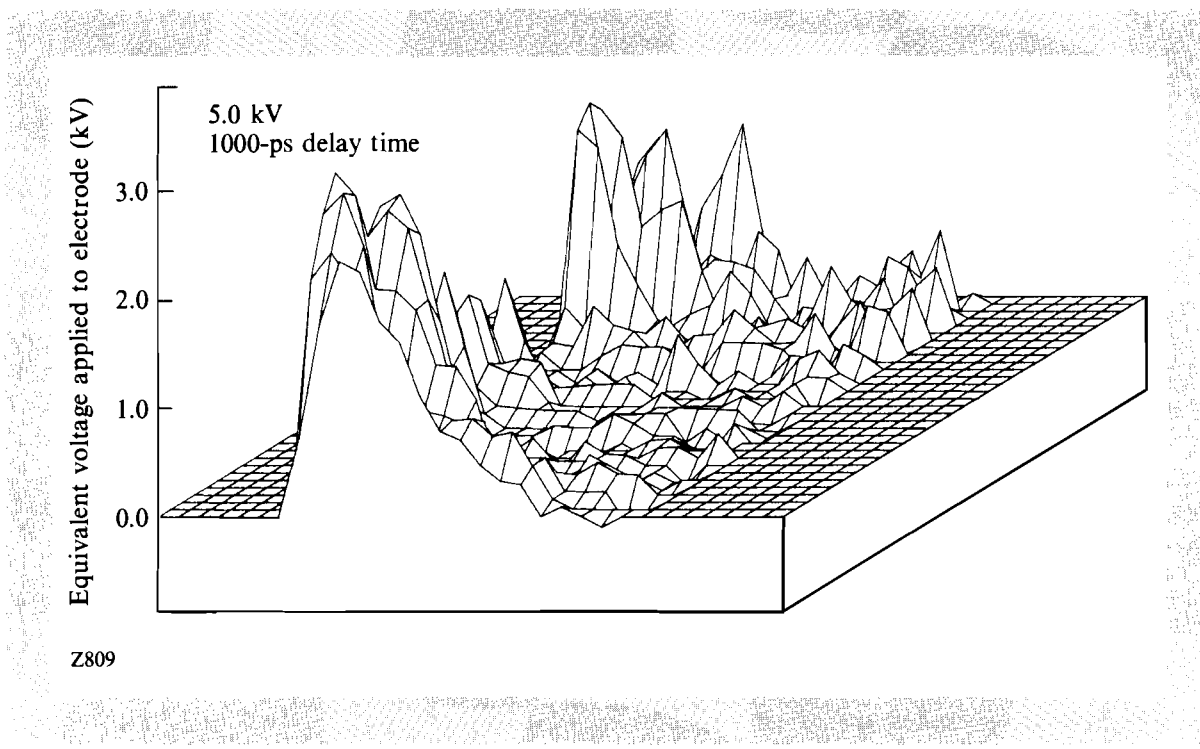

Fig. 42.29
The electro-optic image of the surface electric field on a GaAs switch 800 ps after illumination by a 200-ps IR pulse through both of its electrodes. The left side of the image corresponds to negative high-voltage electrode. The active area is 6 mm by 10 mm and the field enhancements are located behind the solid portion of the high-voltage contact.

The active area in the center is 6 mm wide, and the front and back edges of the image are 10 mm apart and correspond to the edges of the deposited electrodes. Initially, the image was uniform between the contacts. The infrared light has caused the field to collapse. The center section of the image is where the 2-mm-wide pump beam illuminated the GaAs. Note that the field has collapsed over most of the active region to a value of ~0.3-kV EEV although the bias voltage is 5 kV. The field collapses uniformly on the ground side of the image but it has areas of significant enhancement on the high-voltage side. There are two significant high-voltage spikes of ~3-kV EEV even though most of the switch field has collapsed. These spikes are located at the very edges of the high-voltage contact (review Fig. 42.24 for contact geometry). A survey of all the acquired images reveals that this is a general feature independent of the type of contact. There is always an enhancement at the high-voltage contact. The enhancement can be alleviated at the perforated region of the contact by illuminating with more IR light but the collapse is never as complete as on the ground side.

Figures 42.30 and 42.31 show a series of axonometric plots of the field above a 6-mm GaAs switch. These illustrate the progressive collapse of the

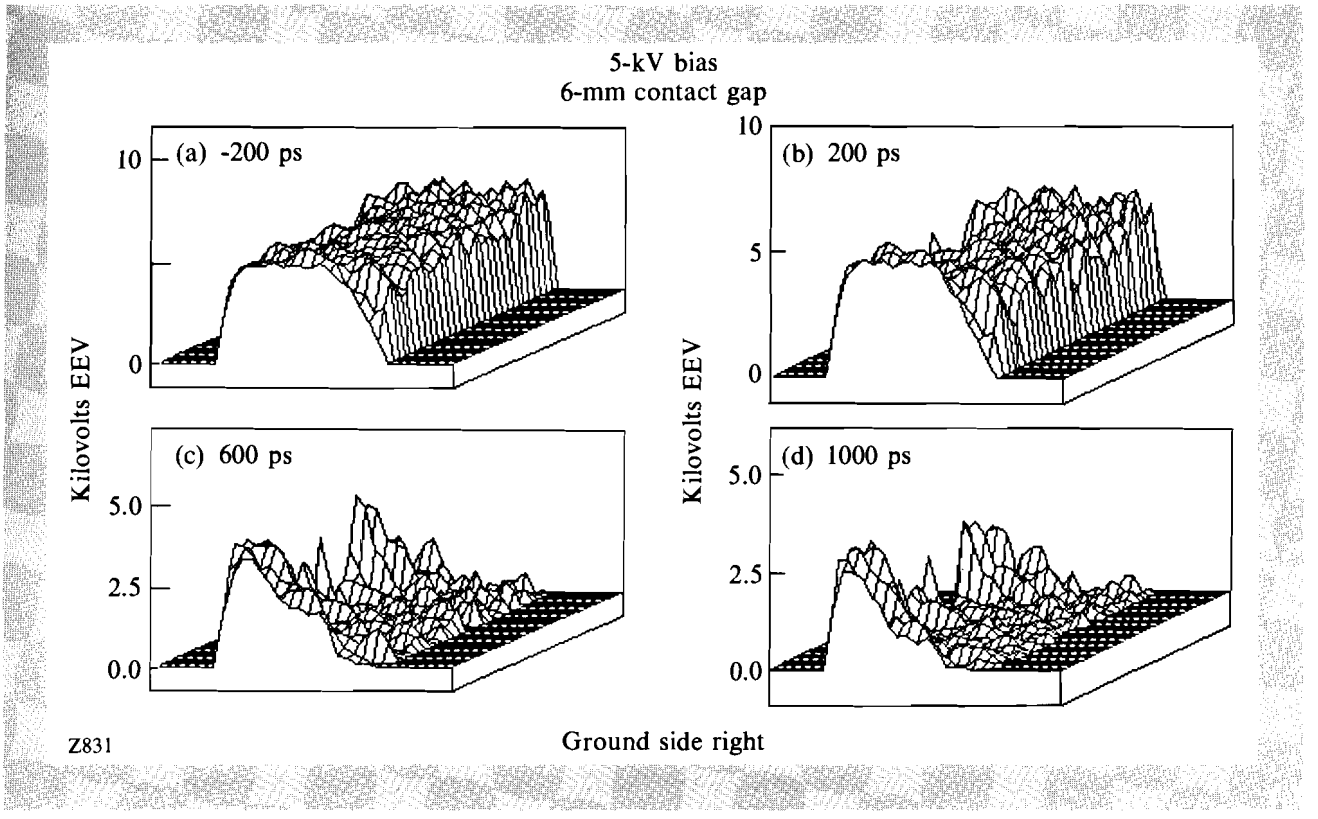

Fig. 42.30
Temporal evolution of electric field above 6-mm-thick bulk GaAs switch illuminated by 200-ps IR pulse through both contacts. Switch biased at 5 kV. Images processed and scaled to equivalent electrode voltage (EEV). The active area of the image is 6 mm by 1 cm. The collapse of electro-optic field proceeds from the essentially uniform profile shown in (a).

surface field in time for two different bias voltages. Both contacts were illuminated with IR light. In Fig. 42.30, the switch bias was 5 kV; in Fig. 42.31, 9 kV. The field is given in EEV, the true field is EEV divided by the gap distance—in this case, 6 mm. The time is relative to the IR translation-stage position; 0 ps is the arrival of the IR pulse and the stage can scan out to 1 ns after IR illumination begins. At −200 ps, the field across the switch is essentially uniform, as expected; as time progresses, the field collapses. For 5-kV bias, the collapse is almost complete, except for the enhancement

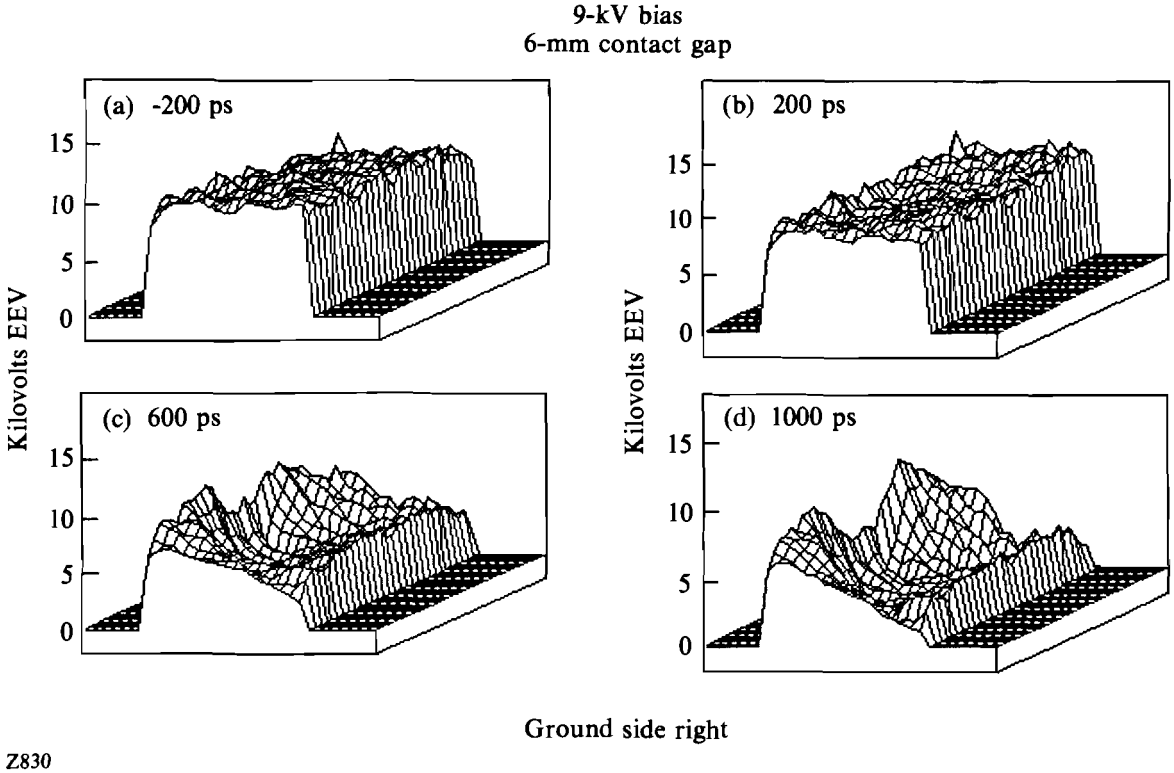

Fig. 42.31
Same conditions as in Fig. 42.30 except switch biased at 9 kV. The incomplete collapse of field is evidenced by ~3 kV/cm field remaining across switch after 1200 ps.

near the contacts. At 9 kV, the situation is much different: the field collapses only to 3-kV EEV. There is still a field of ~3 kV/cm across the switch, 1 ns after illumination.

Figure 42.32 shows a series of lineouts from surface-field images of the 6-mm GaAs switch, taken through the center of the image, perpendicular to the contact faces. These illustrate the progressive collapse of the surface field in time for various illumination schemes. Switch bias was 8 kV.

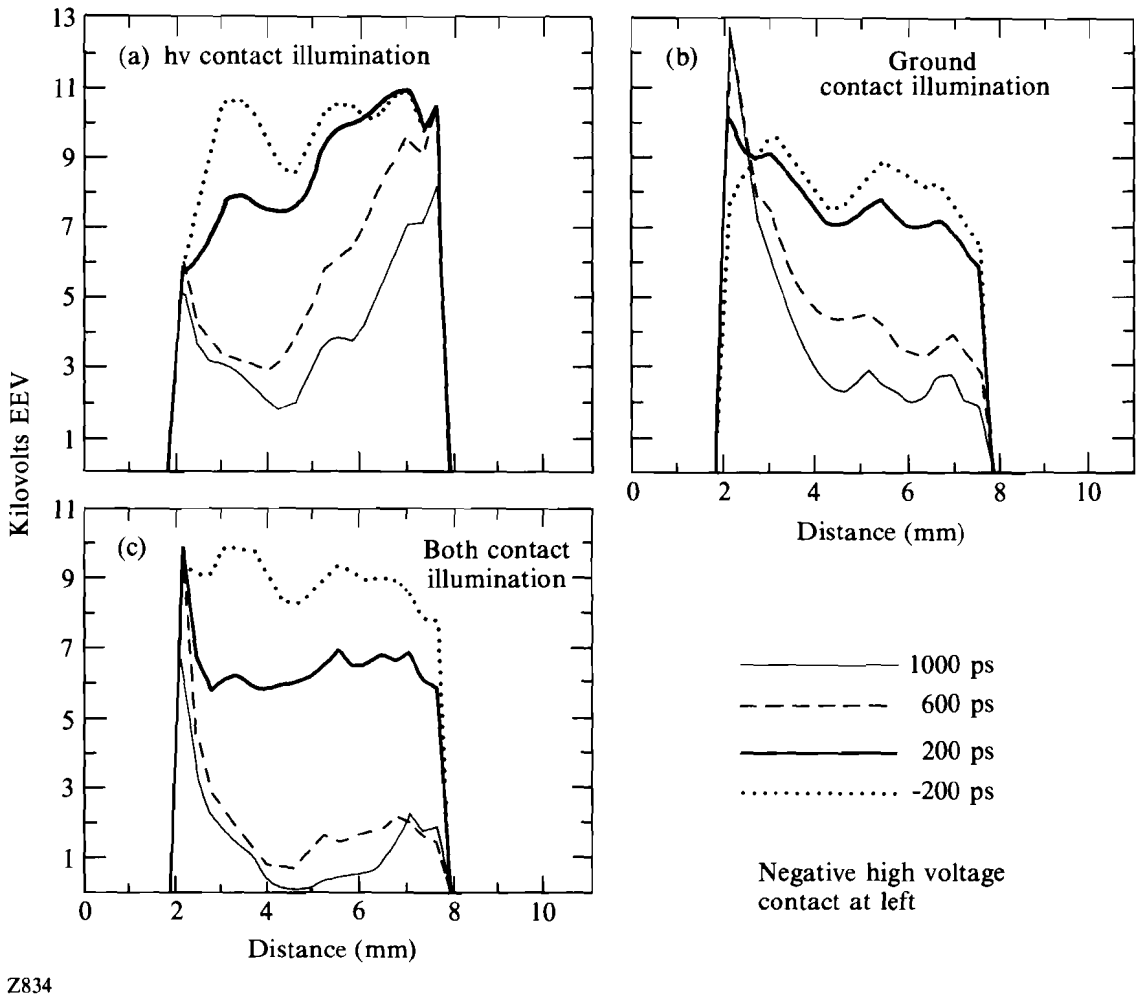

Fig. 42.32
Temporal evolution of electric field above 6-mm-thick bulk GaAs switch for different illumination conditions. Switch biased at 8 kV. Lineouts taken through center of processed electro-optic image at different times after illumination with 200-ps IR pulse. Greater efficiency and speed are obtained for illumination through both contacts.

Single-sided illumination is characterized by a wave front that propagates across the switch. In Figs. 42.32(a) and 42.32(b), the field collapses from the illuminated contact to the nonilluminated contact in time as the region of conduction propagates from the region of photogeneration. When both sides are illuminated [Fig. 42.32(c)], the field collapses more quickly and to a lower final value than for single-sided illumination, as in Figs. 42.32(a) and 42.32(b). Switch rise time is faster and the efficiency is higher for illumination through both contacts—an important engineering consideration. The field enhancement exhibited in Figs. 42.29–42.31 can also be observed in these lineouts. Small differences in the –200-ps lineouts may be caused

by the small prepulses that excite the switch before the main IR pulse arrives, as well as the laser-intensity fluctuation (~10%).

Some of these observations can be made more quantitative by defining an electro-optic switching efficiency. A standard measure of switching efficiency would be the fraction of the dc bias that is switched to the load. A perfectly efficient switch would be driven completely conductive and the bias voltage would appear across the load. No electric field would remain across the switch electrodes. If the electric field across the switch is imaged electro-optically, an electro-optic switching efficiency η can be defined:

$$\eta = \sum_{N} \eta_{i,j} = (1/N) \sum_{N} \left[E'_{i,j} - E_{i,j}(t) / E'_{i,j} \right], \tag{2}$$

where the summation is over the total number of active pixels (pixels outside the electrode gap have been ignored), $E'_{i,j}$ is the electro-optic image element with no IR light present, and $E_{i,j}(t)$ is the electro-optic image element at a time delay t as determined by Eq. (1). The restrictions on the summation are that if

$$E'_{i,j} - E_{i,j}(t) < 0, \tag{3}$$

corresponding to a field enhancement η, was set equal to zero (i.e., it was considered to be an element that had not undergone switching) and if

$$E'_{i,j} - E_{i,j}(t) > E'_{i,j}, \tag{4}$$

implying a negative oscillation in the surface electric field, the efficiency at that point η was set equal to 1. The parameter η is a measure of how much of the dc surface field has been switched, and would measure the total field switched if it were possible to integrate through the entire switch volume. Although this is impossible for these experiments, η still gives a good indication of switch efficiency. Figure 42.33 shows the electro-optic efficiency as a function of the optical delay-line setting for several applied fields in the case of two-sided illumination. The most striking feature of this graph is that the switching efficiency drops as the field increases. Figure 42.34 shows that this trend continues with single-sided illumination at two different intensities. For example, at an illumination intensity of 2.1 mJ/cm^2, there is sufficient light to switch a field of 6.6 kV/cm with 90% efficiency. At the same intensity, a field of 15 kV/cm is switched with only 40% efficiency. Figure 42.34(a) shows that increasing the intensity to 3.8 mJ/cm^2 increases the efficiency to only 50% at 15 kV/cm. The rise time of the switch also decreases as the light intensity is increased.

Discussion

A number of important features regarding the operation of GaAs photoconductive switches can be discerned from this work. First, the electric

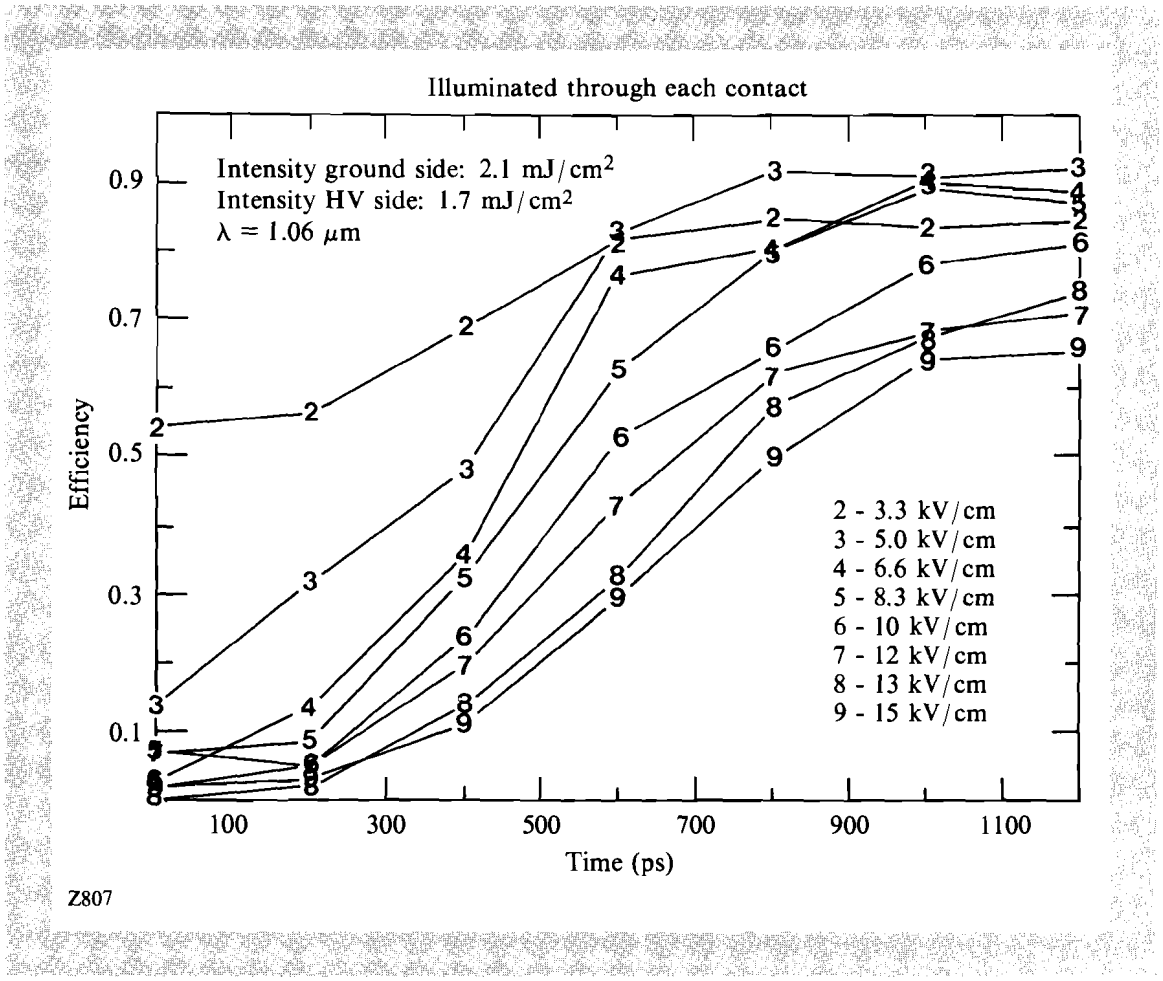

Fig. 42.33
The electro-optic efficiency for a 6-mm bulk GaAs photoconductive switch illuminated through both contacts as a function of time. The efficiency decreases with increasing field.

field is enhanced at the negative high-voltage electrode and collapses most slowly there. This type of behavior was seen in both types of contacts tested. Similar behavior has been predicted to occur at both contacts for uniformly illuminated silicon switches with ohmic contacts.[11] The field enhancement, in that case, was shown to be caused by rapid carrier sweep-out at the ohmic contacts. It is possible that ohmic contacts at the negative electrode are responsible for the field enhancement observed in the data. In particular, the enhancement was strongest under the solid portion of the high-voltage contact. A corresponding enhancement was not observed on the ground-side electrode (positive with respect to the high-voltage pulse). This enhancement was reduced in the perforated region by increasing the light incident on the high-voltage contact. This enhancement was seen in all samples and showed some increase with the number of shots applied to the sample. Thus, some of the nonuniform enhancement may have been associated with the long-term degradation of the contact ($>2 \times 10^4$ shots) due to arcing from the perforated region to the solid region of the NiAu:Ge contact. This arcing only occurred if the GaAs was switched.

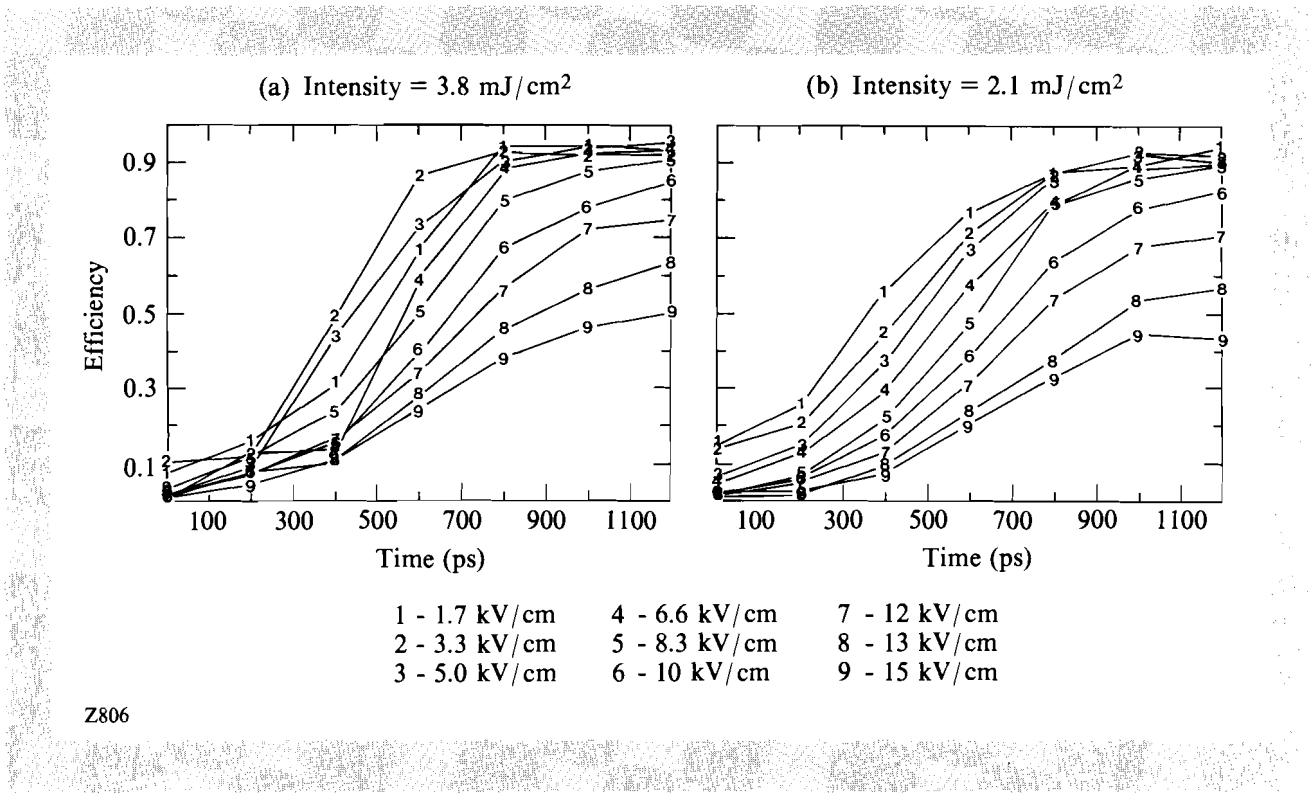

Fig. 42.34
The electro-optic efficiency of a GaAs photoconductive switch illuminated through only the high-voltage contact; (a) 3.8 mJ/cm^2, (b) 2.1 mJ/cm^2.

The switching efficiency of GaAs decreased with increasing voltage. Increasing the number of carriers by increasing the IR illumination energy by a factor of ~2 does not significantly improve switching efficiency, suggesting that switching efficiency is predominantly a field effect. This is confirmed by the observation that, for constant bias voltage, the switching efficiency increases with increasing electrode spacing, although this data is not presented here. The measured decrease in switching efficiency with increasing voltage may well be caused by the negative differential resistance in GaAs.[12] Above 3 kV/cm, the electron drift velocity in GaAs decreases as the electric field increases. Since the current is proportional to the drift velocity, this represents an effective increase in switch resistance as the field increases above 3 kV/cm. This observation has important implications for the use of photoconductive switches in pulsed-power applications. In many cases, the trend has been to push the breakdown limit in these devices to achieve the highest switch electrical energy for the minimum optical energy. These results indicate that switches with larger gaps and lower bias fields are much more efficient in terms of switched voltage for a given pump energy.

The electrode geometry of the Si surface switches results in a very nonuniform field between the contacts, making calibration and extraction of

absolute field values difficult. Also, Si switch surface fields were greatly affected by the aforementioned laser prepulses, again making field measurements difficult. However, the lack of significant peaking at the contacts and the different modes of collapse with different illuminator regimes show some of the underlying carrier dynamics.

The two-dimensional electro-optic imaging system can time resolve the full spatial and temporal variations of the electric field on semiconductor surfaces. The images have provided significant insight into the mechanism of photoconductive switching in GaAs. The primary strength of this diagnostic is its ability to monitor events inside the electrode gap itself, which is a distinct advantage over monitoring only the semiconductor device output waveform. Switching parameters can be measured with no electrical connection to the high-voltage circuit. Extension of this work to integrated circuits could allow the characterization of devices without introducing connector or strip-line effects. Future work will center around using the electro-optic imaging system to investigate the phenomena of surface breakdown and further the study of semiconductor photoconductivity. Images obtained with the system should provide an appropriate experimental basis for a complete model of the photoconductive process.

ACKNOWLEDGMENT

This work was supported by the Laser Fusion Feasibility Project at the Laboratory for Laser Energetics, which has the following sponsors: Empire State Electric Energy Research Corporation, New York State Energy Research and Development Authority, Ontario Hydro, and the University of Rochester, and also by the SDIO/IST and managed by the Office of Naval Research under contract N00014-86-K-0583. Such support does not imply endorsement of the content by any of the above parties.

The GaAs was supplied by M. Weiner, A. Kim, and R. Zeto at the U.S. Army Electronics Technology and Device Laboratory.

REFERENCES

1. G. Mourou, W. H. Knox, and S. Williamson, *Picosecond Optoelectronic Devices*, Chap. 7 (Academic Press, New York, NY, 1984), p. 219.
2. C. Bamber, W. Donaldson, T. Juhasz, L. Kingsley, and A. C. Melissinos, *Part. Accel.* **23**, 255 (1988).
3. J. A. Valdmanis, G. Mourou, and C. W. Gabel, *Appl. Phys. Lett.* **41**, 211 (1982).
4. K. Meyer, M. Pessot, G. Mourou, R. Grondin, and S. Chamoun, *Appl. Phys. Lett.* **53**, 2254 (1988).
5. LLE Review **34**, 74 (1988).
6. Z. H. Zhu, J.-P. Weber, S. Y. Wang, and S. Wang, *Appl. Phys. Lett.* **49**, 432 (1986).
7. Y. H. Lo *et al.*, *Appl. Phys. Lett.* **50**, 1125 (1987).
8. A. Yariv, *Quantum Electronics*, 2nd ed., Chap. 14 (John Wiley & Sons, New York, NY, 1975), p. 327.
9. I. N. Duling III, T. Norris, T. Sizer II, P. Bado, and G. A. Mourou, *J. Opt. Soc. Am. B* **2**, 616 (1985).

10. L. Bovino *et al.*, *Digest of Technical Papers*, 5th IEEE Pulse Power Conference, edited by P. Turchi and M. F. Rose (IEEE, New York, NY, 1985), p. 242.

11. A. E. Iverson, *Trans. Soc. Comput. Simulation* **5**, 175 (1988).

12. S. M. Sze, *Physics of Semiconductor Devices* (John Wiley & Sons, New York, NY, 1981), p. 44.

Section 3
NATIONAL LASER USERS FACILITY NEWS

The three major activities during the second quarter of FY90 were as follows: (1) support for **A. Honig** of Syracuse University; (2) target fabrication for **C. Hooper** of the University of Florida; and (3) the preparation for review of proposals for FY91.

A. Honig is building a cold-insertion target handler for the OMEGA cryogenic target positioner. This device will allow the insertion of targets prepared outside the OMEGA target chamber at liquid-helium temperatures. Cryogenic targets can thus be prepared and characterized and then inserted for laser shots, in a process similar to the handling of gas targets. This positioner is critical to the spin-polarized target experiments of the Syracuse research group and will find application in a wide variety of ICF target experiments. The cold-insertion handler is expected to be fitted to the OMEGA target chamber during the third quarter of FY90.

Plastic argon-filled microballoons are being constructed for C. Hooper, using the microencapsulation technique. The shell diameters will be about 250 μm and thus better suited to uniform illumination than the 400-μm-diam targets used in December 1987. Argon fill pressures will vary between 1 and 10 atm so that a range of convergence ratios can be studied. These experiments are being modeled with the *LILAC* hydrodynamics code at LLE and will be used to study high-density laser-driven implosions.

The DOE deadline for FY91 proposals was 1 March 1990. This was changed from last year so that principal investigators could be notified in May of the results of the steering committee review. Table 42.II lists the 11 proposals received for FY91. Ten of these request DOE funding and one requests GDL laser time. The steering committee met at the end of April to review the scientific merit of the proposals. The results of the technical review were sent to DOE to select proposals for funding and for notification of all principal investigators. Members of the committee are listed in Table 42.III. The new members for this year are **P. Goldstone** (LANL) and **R. Turner** (LLNL).

Table 42.II: Proposals for FY91 NLUF experiments.

Number	Organization	Title	P.I. Name
162	University of Florida	Time-Resolved Emission and Absorption Spectroscopy of High-Density Plasmas in Spherical and Planar Geometry	C. F. Hooper
163	Lockheed MSC	Time-Dependent Study of the Ionization Dynamics in a Laser-Produced Plasma from a Supersonic Gas Jet	P. Filbert
164	Lockheed MSC	Study of the Sodium-Neon Photopumped X-Ray Laser Using High-Power Laser Irradiation of High-Density Planar Gas Jet to Create the Neon Lasant	P. Filbert
165	University of Wisconsin-Madison	Experimental Determination of Non-LTE Radiative Transfer Effects in High-Temperature, Moderate-Density Plasmas	J. MacFarlane
166	Syracuse University	Fusion with Highly Spin Polarized HD and D_2	A. Honig
167	University of Maryland	Experimental Studies of Radiative Properties of High Energy Density Matter	H. Griem
168	US DOC, National Institute Standards and Technology	Atomic Structure of Ni-Like, Soft X-Ray Lasing Ions	J. Reader
169	University of California/ Davis	Development of a New Plasma Diagnostic of the Critical Surface and Studies of the Ion Acoustic Decay Instability Using Collective Thomson Scattering	J. S. DeGroot
170	Naval Research Laboratory	X-Ray Line Coincidence Diagnosis of Core-Shell Mixing in ICF Target Implosions	J. Apruzese
171	Naval Research Laboratory	XUV Spectroscopy Studies at the OMEGA Laser	J. Seely
172	Rensselaer	Futuristic Propulsion System	L. Myrabo

U153

Table 42.III: Voting members of the NLUF Steering Committee.

Dr. K. Matzen	Sandia National Laboratory
Dr. E. Spiller	IBM Watson Research Center
Dr. K. Hill	Princeton Plasma Research
Dr. J. Perez	Auburn University
Dr. P. Goldstone	Los Alamos National Laboratory
Dr. R. Turner	Lawrence Livermore National Laboratory

U154

ACKNOWLEDGMENT

This work was supported by the U.S. Department of Energy Division of Inertial Fusion under agreement No. DE-FC03-85DP40200.

Section 4
LASER SYSTEM REPORT

4.A GDL Facility Report

During the first half of the second quarter of FY90, GDL operations concentrated on three main programs: shine-through, x-ray laser, and Bessel-beam propagation. There were also many shots devoted to identification and suppression of a prepulse. The second half of the quarter was devoted to an oscillator reconstruction in which the GDL oscillator was totally rebuilt, with attention given to vibrational and electrical isolation for the purpose of ensuring proper phase stabilization. This work also included changing the frequency of the rf-driven mode-locker and Q-switch from 66 MHz to 50 MHz. Ultimately these upgrades plus the installation of a regenerative amplifier seeded by a cw laser will provide pairs of accurately timed pulses enabling us to perform pulse-shaping experiments.

A summary of the quarter's GDL operation follows:

Beamline Test, Calibration, Tuning and Laser Alignment Shots	407
Target Shots	
Shine-through	56
X-Ray Laser	41
Bessel Beam	46
TOTAL	550

ACKNOWLEDGMENT

This work was supported by the U.S. Department of Energy Division of Inertial Fusion under agreement No. DE-FC03-85DP40200 and by the Laser Fusion Feasibility Project at the Laboratory for Laser Energetics, which has the following sponsors: Empire State Electric Energy Research Corporation, New York State Energy Research and Development Authority, Ontario Hydro, and the University of Rochester.

4.B OMEGA Facility Report

During the second quarter of FY90, the OMEGA laser facility resources were allocated to three main programs. First, beam-uniformity improvements for target irradiation went through system integration and testing cycles, followed by target-interaction studies. Then, two other campaigns were supported, each utilizing single OMEGA beamlines. Large-signal-gain measurements were made on a multisegmented amplifier (MSA), and stimulated rotational Raman scattering (SRRS) threshold measurements in the ultraviolet (351 nm) were also acquired.

As reported last quarter, the SSD uniformity-enhancement system was upgraded from 3-GHz to 8-GHz modulation frequency. A new style of microwave resonant cavity was completed and installed in the OMEGA driver line. Streak-camera measurements of amplitude modulation in the laser were well correlated with the theoretical modeling, and target shots were taken to quantify the effects of the faster smoothing times. A more detailed description of the SSD improvements will appear in a future LLE Review article.

An MSA prototype amplifier was assembled in a class-100 cleanroom within the OMEGA laser bay. The goal of this campaign was to characterize the amplifier performance, specifically the large-signal gain. OMEGA infrared output pulses at the 120- to 130-J level, 800 ps, were used as input for one of the four MSA beam paths. The MSA was synchronized to OMEGA, with the output of beam 6-4 double-passing the amplifier. OMEGA calorimetry, interferometry, and other diagnostics were deployed to characterize the MSA performance over the full range of operational parameters. During these tests a laboratory single-beam energy record of 949 J was set. Further details will be published in a future LLE Review article.

After the MSA tests were completed, beam 6-2 was converted to UV for SRRS experiments. As SRRS is a function of the product of intensity and interaction length, a long-path high-intensity beam setup was constructed to ensure conditions for threshold would be easily achieved. In fact, many shots were taken both above and below threshold for accurate characterization.

OMEGA was used for these measurements because it is the only facility that has SSD beam smoothing, and SRRS dependence on bandwidth and dispersion was a parameter space that to date has never been explored empirically. Data collection on this experiment will be completed early next quarter.

A shot summary for the quarter follows:

Driver Line		59
Software Test		50
Laser		94
Target		63
MSA		82
SRRS		25
	TOTAL	373

ACKNOWLEDGMENT

This work was supported by the U.S. Department of Energy Division of Inertial Fusion under agreement No. DE-FC03-85DP40200 and by the Laser Fusion Feasibility Project at the Laboratory for Laser Energetics, which has the following sponsors: Empire State Electric Energy Research Corporation, New York State Energy Research and Development Authority, Ontario Hydro, and the University of Rochester.

PUBLICATIONS AND CONFERENCE PRESENTATIONS

Publications

G. Banas, H. E. Elsayed-Ali, F. V. Lawrence, Jr., and J. M. Rigsbee, "Laser Shock-Induced Mechanical and Microstructural Modification of Welded Maraging Steel," *J. Appl. Phys.* **67**, 2380–2384 (1990).

T. Boehly, B. Yaakobi, D. Shvarts, D. Meyerhofer, P. Audebert, J. Wang, M. Russotto, B. Boswell, R. Epstein, R. S. Craxton, and J. M. Soures, "X-Ray Laser Experiments Using Double Foil Nickel Targets," *Appl. Phys. B* **50**, 165–172 (1990).

B. Boswell, D. Shvarts, T. Boehly, and B. Yaakobi, "X-Ray Laser Beam Propagation in Double-Foil Targets," *Phys. Fluids B* **2**, 436–444 (1990).

W. R. Donaldson, A. M. Kadin, P. H. Ballentine, and M. Shoup, "Optically Activated High Temperature Superconductor Opening Switches," in *Digest of Technical Papers,* Seventh IEEE Pulsed Power Conference, edited by R. White and B. H. Bernstein (IEEE, New York, 1989), pp. 897–901.

H. E. Elsayed-Ali, "Hot Electron Relaxation in Metals," in *1989 Technical Digest Series, Volume 17, High Energy Density Physics with Subpicosecond Laser Pulses* (Optical Society of America, Washington, DC, 1989), pp. 58–65.

C. Immesoete, L. Forsley, and H. Kim, "Computer-Assisted Microballoon Selection for Laser Fusion Targets," in *Proceedings of the Forth Conference,* Rochester, NY, 19–23 June 1989, pp. 80–83.

P. A. Jaanimagi, R. Saunders, C. Hestdalen, W. VanRemmen, and M. Russotto, "Pulse-Shape Measurements on OMEGA," *Ultrahigh Speed and High Speed Photography, Photonics, and Videography* (SPIE, Bellingham, WA, 1989), Vol. 1155, pp. 556–562.

H. Kim, P.-C. Cheng, M. D. Wittman, and H.-J. Kong, "X-Ray Microscopy of Living Biological Specimens Using a Laser-Plasma as an X-Ray Source," *X-Ray Instrumentation in Medicine and Biology, Plasma Physics, Astrophysics, and Synchrotron Radiation* (SPIE, Bellingham, WA, 1989), Vol. 1140, pp. 256–261.

H. G. Kim, P. C. Cheng, M. D. Wittman, and H. J. Kong, "Pulsed X-Ray Contact Microradiography and Its Applications to Structural and Developmental Botany," in *X-Ray Microscopy in Biology and Medicine,* edited by K. Shinohara *et al.* (Japan Sci. Soc. Press, Tokyo/Springer-Verlag, Berlin, 1990), pp. 233–242.

L. E. Kingsley and W. R. Donaldson, "Electro-Optic Surface Field Imaging System," in *Digest of Technical Papers,* Seventh IEEE Pulsed Power Conference, edited by R. White and B. H. Bernstein (IEEE, New York, 1989), pp. 376–379.

J. C. Lambropoulos, "Analysis of Thermal Stress, Fracture Strength and the Effect of Ion Exchange on High Average Power Phosphate Glass Slab Lasers," *J. Appl. Phys.* **67**, 1784–1792 (1990).

R. L. McCrory, J. M. Soures, C. P. Verdon, F. J. Marshall, S. A. Letzring, T. J. Kessler, J. P. Knauer, H. Kim, R. L. Kremens, S. Skupsky, R. L. Keck, D. K. Bradley, W. D. Seka, P. A. Jaanimagi, J. A. Delettrez, and P. W. McKenty, "High Density Direct Drive Cryogenic Implosion Experiments," in *Plasma Physics and Controlled Nuclear Fusion Research-1988* (International Atomic Energy Agency, Vienna, 1989), Vol. 3, pp. 17–27.

C. J. McKinstrie, G. G. Luther, and S. H. Batha, "Signal Enhancement in Collinear Four-Wave Mixing," *J. Opt. Soc. Am. B* **7,** 340–344 (1990).

R. W. Short and S. Skupsky, "Frequency Conversion of Broad-Bandwidth Laser Light," *IEEE J. Quantum Electron.* **26,** 580–588 (1990).

A. Simon and R. W. Short, "Reply to the Comments of Drake," *Phys. Fluids B* **2,** 227–228 (1990).

M. L. Tsai and S. H. Chen, "Helical Sense in Thermotropic Liquid Crystal Copolymers in Relation to the Structure of Pendant Chiral Moiety," *Macromolecules* **23,** 1908–1911 (1990).

M. L. Tsai, S. H. Chen, K. L. Marshall, and S. D. Jacobs, "Thermotropic and Optical Properties of Chiral Nematic Polymers," *Int. J. Thermophys.* **11,** 213–223 (1990).

Forthcoming Publications

G. Banas, F. V. Lawrence Jr., J. M. Rigsbee, and H. E. Elsayed-Ali, "Laser Shock Hardening of Welded Maraging Steel," to be published in *Surface Engineering: Current Trends and Future Prospects*, edited by S. A. Meguid (Elsevier Applied Science, Toronto, Canada, 1990).

S. H. Batha, D. D. Meyerhofer, A. Simon, and R. P. Drake, "Enhanced Scattering from Laser-Plasma Interactions," to be published in *Physical Review*.

H. C. Chen, G. Mourou, and R. Knox, "Time-Resolved Electron Diffraction from Pulse-Excited Crystalline Gold Films," to be published in the *Proceedings of 1989 Materials Research Society Fall Meeting: Beam-Solid Interactions*, Boston, MA, 27 November–2 December 1989; and in *Physical Review Letters*.

P. C. Cheng, V. H-K. Chen, H. G. Kim, and R. E. Pearson, "A Real-Time EPI-Fluorescent Confocal Microscope," to be published in *Journal of Microscopy*.

P. C. Cheng, V. H-K. Chen, H. G. Kim, and R. E. Pearson, "An EPI-Fluorescent Spinning-Disk Confocal Microscope," to be published in the *Proceedings of the 47th Annual Meeting of Electron Microscopy Society of America* (EMSA), Austin, TX, 14–18 August 1989.

J. Delettrez, D. K. Bradley, P. A. Jaanimagi, and C. P. Verdon, "Effect of Barrier Layers in Burnthrough Experiments with 351-nm Laser Illumination," to be published in *Physical Review A*.

H. E. Elsayed-Ali, "Comments on 'Thermal Response of Metals to Ultrashort-Pulse Laser Excitation'," to be published in *Physical Review Letters*.

H. E. Elsayed-Ali and J. W. Herman, "Transient Surface Debye-Waller Effect," (invited paper) to be published in SPIE's *Proceedings of Picosecond and Femtosecond Spectroscopy from Laboratory to Real World*.

H. E. Elsayed-Ali and J. W. Herman, "An Ultrahigh Vacuum Picosecond Laser-Driven Electron Diffraction System," to be published in *Review of Scientific Instruments*.

H. E. Elsayed-Ali, T. Juhasz, G. O. Smith, and W. E. Bron, "Femtosecond Thermoreflectivity and Thermotransmissivity of Polycrystalline and Single-Crystalline Gold Films," to be published in *Physical Review Letters*.

E. M. Epperlein, "Electron Kinetics in Laser-Driven Inertial Confinement Fusion," to be published in the *Proceedings of the Topical Conference on Research Trends in Nonlinear and Relativistic Effects in Plasmas*, San Diego, CA, 5–8 February 1990.

R. Epstein and S. Skupsky, "Anticipated Improvement in Laser Beam Uniformity Using Distributed Phase Plates with Quasi-Random Patterns," to be published in *Journal of Applied Physics*.

M. Y. Frankel and T. Y. Hsiang, "Picosecond Transient Behavior of Pseudomorphic High Electron Mobility Transistor—Simulations," to be published in *IEEE Transactions on Electron Devices.*

M. Y. Frankel, D. R. Dykaar, T. Y. Hsiang, K. H. Duh, and P. C. Chao, "Non-Invasive, Picosecond Transient Characterization of Pseudomorphic High Electron Mobility Transistor (HEMT)," to be published in *IEEE Transactions on Electron Devices.*

R. Q. Gram, M. D. Wittman, C. Immesoete, H. Kim, R. S. Craxton, N. Sampat, S. Swales, G. Pien, J. M. Soures, and H. Kong, "Uniform Liquid-Fuel Layer Produced in a Cryogenic Inertial Fusion Target by a Time-Dependent Thermal Gradient," to be published in *Journal of Vacuum Science and Technology A.*

C. Immesoete, S. Scarantino, H. Kim, and L. Forsley, "Computer-Assisted Microballoon Selection for Inertial Confinement Fusion Targets," to be published in *Journal of Vacuum Science and Technology A.*

H. G. Kim, C. K. Immesoete, and S. Scarantino, "Computer-Assisted Microballoon Selection for Inertial Fusion Targets," to be published in the *Proceedings of the Seventh Target Fabrication Specialists Meeting,* Livermore, CA, 25–29 September 1989.

H. G. Kim, R. Q. Gram, M. D. Wittman, C. Immesoete, R. S. Craxton, N. Sampat, S. Swales, G. Pien, and J. M. Soures, "Uniform Liquid Fuel Layer Produced in a Cryogenic Target by a Time-Dependent Thermal Gradient," to be published in the *Proceedings of the Seventh Target Fabrication Specialists Meeting,* Livermore, CA, 25–29 September 1989.

L. E. Kingsley and W. R. Donaldson, "Electro-Optic Imaging of Surface Electric Fields in High-Power Photoconductive Switches," to be published in *IEEE Transactions on Electron Devices.*

J. C. Lambropoulos and S.-S. Hwang, "Film Thermal Conductivity and Laser Damage Resistance of Optical Thin Films," to be published in *Proceedings of a Symposium on Electro-Optics and Non-Linear Optics,* 1st International Congress on Ceramic Science and Technology, Anaheim, CA, 1–3 November 1989.

J. C. Lee and S. D. Jacobs, "Design and Construction of 1064 nm Liquid Crystal Laser Cavity End Mirrors," to be published in *Applied Physics Letters.*

J. C. Lee, S. D. Jacobs, and K. J. Skerrett, "Laser Beam Apodizer Utilizing Gradient-Index Optical Effects in Liquid Crystals," to be published in *Optical Engineering.*

J. C. Lee, S. D. Jacobs, T. Gunderman, A. Schmid, T. J. Kessler, and M. D. Skeldon, "TEM_{OO} Mode and Mono-Mode Laser Operation with a Cholesteric Liquid Crystal Laser End Mirror," to be published in *Optics Letters.*

G. G. Luther and C. J. McKinstrie, "The Transverse Modulational Instability of Colinear Waves," to be published in *Journal of the Optical Society of America B.*

R. L. McCrory, "New Research Trends in Inertial Confinement Fusion," to be published in the *Proceedings of the Topical Conference on Research Trends in Nonlinear and Relativistic Effects in Plasmas*, La Jolla, CA, 5–8 February 1990.

R. L. McCrory and C. P. Verdon, "Computer Modeling and Simulation in Inertial Confinement Fusion," to be published in *Il Nuovo Cimento.*

P. W. McKenty, C. P. Verdon, S. Skupsky, R. L. McCrory, D. K. Bradley, W. Seka, and P. A. Jaanimagi, "Numerical Modeling of Effects of Power Imbalance on Irradiation Nonuniformities," to be published in the *Journal of Applied Physics.*

C. J. McKinstrie and G. G. Luther, "The Modulational Instability of Colinear Waves," to be published in *Physica Scripta, Special Issue on Large-Amplitude Waves in Plasmas.*

D. D. Meyerhofer, S. Augst, Y. H. Chuang, J. Delettrez, and M. C. Richardson, "Comparison of Multiphoton and Collisional Ionization in High Intensity Laser-Plasma Interactions," to be published in the *Proceedings of the Topical Meeting on High Energy Density Physics with Subpicosecond Lasers,* Snowbird, UT, 11–13 September 1989.

T. B. Norris, X. J. Song, G. Wicks, W. J. Schaff, L. F. Eastman, and G. A. Mourou, "Electric Field Dependence of the Tunneling Escape Time of Electrons from a Quantum Well," to be published in the *Proceedings of Picosecond Electronics and Optoelectronics Conference,* Salt Lake City, UT, 8–10 March 1989.

T. B. Norris, N. Vodjdani, B. Vinter, C. Weisbuch, and G. A. Mourou, "Time-Resolved Observation of Luminescence from a Charge-Transfer State in Double Quantum Wells," to be published in the *Proceedings of the Optical Society of America, Quantum Wells for Optics and Optoelectronics,* Salt Lake City, UT, 6–8 March 1989.

D. Y. Park, W. Seka, Y. Lin, and D. L. Brown, "Operational Characteristics of an Imaging, Unstable Ring Resonator Using Nd:YLF as Active Medium," to be published in *Proceedings of the Ninth Workshop on Laser Interaction and Related Plasma Phenomena,* Monterey, CA, 6–10 November 1989.

Conference Presentations

The following presentations were made at the SPIE's OE/LASE Conference '90, Los Angeles, CA, 14–19 January 1990:

S. Augst, D. D. Meyerhofer, C. I. Moore, and J. Peatross, "Tunneling Ionization and Harmonic Generation in Krypton Gas Using a High-Intensity, 1 μm, 1 ps, Laser."

H. Chen, Y. H. Chuang, R. Epstein, D. D. Meyerhofer, S. Uchida, and B. Yaakobi, "Spectroscopic Investigation of Plasma Produced with High-Intensity, 1 μm, 1 ps, Laser Pulses."

H. E. Elsayed-Ali and J. W. Herman, "Transient Surface Debye-Waller Effect."

D. D. Meyerhofer, H. Chen, Y. -H. Chuang, J. Delettrez, R. Epstein, S. Uchida, and B. Yaakobi, "High Intensity, Short-Pulse (1 ps), Laser-Plasma Interaction at 1 μm."

The following presentations were made at the 20th European Conference on Laser Interaction with Matter (ECLIM), Schliersee, Federal Republic of Germany, 22–26 January 1990:

R. L. McCrory, J. M. Soures, C. P. Verdon, F. J. Marshall, S. A. Letzring, S. Skupsky, R. L. Kremens, J. P. Knauer, H. Kim, R. Short, T. Kessler, R. S. Craxton, J. Delettrez, R. L. Keck, and D. K. Bradley, "Cryogenic SSD Direct-Drive Implosions on OMEGA."

W. Seka, J. M. Soures, and J. Kelly, "Energy Balance, Power Balance, and Intensity Balance for Direct-Drive Laser Fusion Experiments."

The following presentations were made at the Topical Conference on Research Trends in Nonlinear and Relativistic Effects in Plasmas, La Jolla, CA, 5–8 February 1990:

E. M. Epperlein, "Electron Kinetics in Laser-Driven Inertial Confinement Fusion."

R. L. McCrory, "New Research Trends in Inertial Confinement Fusion."

P. H. Ballentine, A. M. Kadin, W. R. Donaldson, J. H. Scofield, and L. J. Bajuk, "Optically Triggered Switching of Superconducting $YBa_2Cu_3O_7$ Thin Films," presented at the SPIE Conference on High Tc Superconductivity: Thin Films and Applications, San Diego, CA, 17–21 March 1990.

A. Simon, "Nonlinear Aspects of Raman Scattering in Plasma," presented at the NAS and ASUSSR Workshop on Optical and Plasma Physics, Irvine, CA, 26–30 March 1990.

T. Juhasz, G. O. Smith, W. E. Bron, and H. E. Elsayed-Ali, "Hot Electron Relaxation in Gold Films with Different Structures," presented at the APS Meeting, Anaheim, CA, 12–16 March 1990.

ACKNOWLEDGMENT

The work described in this volume includes current research at the Laboratory for Laser Energetics, which is supported by Empire State Electric Energy Research Corporation, New York State Energy Research and Development Authority, Ontario Hydro, the University of Rochester, and the U.S. Department of Energy Division of Inertial Fusion under agreement No. DE-FC03-85DP40200.